Retrofit design of a line-start permanent-magnet synchronous machine

KS Garner

23148543

Dissertation submitted in fulfilment of the requirements for the degree *Magister* in Electrical and Electronic Engineering at the Potchefstroom Campus of the North-West University

Supervisor: Dr AJ Grobler

May 2015

Summary

Energy resources are under tremendous pressure with society's ever increasing need for electricity. However, resources are becoming scarce and the effect of our power generation on the environment is cause for concern. The cost of electricity is also increasing and thus the need to reduce energy consumption is apparent. Most electrical energy generated is consumed by electric motors. Most of these motors are induction motors because they are reliable, efficient and durable. Though these motors are highly efficient, there is still room for improvement when the strain on electrical energy is taken into account. Constructing motors with better efficiency can result in a reduction in energy consumption and cost savings to the consumer.

One method of increasing a motor's efficiency is to use permanent magnets in the construction of the motor's core. Permanent magnets eliminate the excitation losses experienced by induction machines, thereby increasing the motor's efficiency. A retrofit design is considered because of the ease of manufacturing for motor suppliers and the ability to apply the solution to existing operating induction machines. The prototype will lay the foundation for future optimisation strategies. The optimised design should provide improved efficiency with a minimum effect on the motors already operating in industry.

The design process followed uses the design principles for inductions machines and for sizing permanent magnets. The design is then verified through the use of finite element method software packages, FEMM and ANSYS Maxwell®, and validated by performance testing. A comparison is drawn between the calculated results and the results determined from the performance analysis. The retrofit design performed as expected during the testing with some discrepancies in final values attributed to the manufacturing process. However, the efficiency is lower than designed and requires the implementation of machine optimisation strategies.

Keywords: Induction machine, Retrofit design, LSPMSM, PMSM, Permanent magnet

Acknowledgments

I would like to use this opportunity to acknowledge and thank the following for their assistance and support:

- Dr Andre Grobler who provided me guidance and insight over the years.
- Albert Sorgdrager for always being willing to assist.
- Zest WEG Group for assisting in terms of machine hardware and technical information.
- Sasol Technology Limited for funding the research.
- Marthinusen & Coutts and Elvis Lekhoaba for aiding in the wiring, assembling and final tests on the prototype machine.
- My family and friends who provided understanding and encouragement.

Declaration

I, *Karen Sharon Garner*, declare that the dissertation is a presentation of my own original work, conducted under the supervision of Dr A.J. Grobler.

Whenever contributions of others are involved, every effort is made to indicate this clearly, with due reference to the literature.

No part of this work has been submitted in the past, or is being submitted, for a degree or examination at any other university or course.

Signed on this ____ day of _____ 2015, in Potchefstroom.

_____

Initials and Surname

TABLE OF CONTENTS

LIST OF PUBLICATIONS ..... **I**

LIST OF SYMBOLS ..... **II**

LIST OF ABBREVIATIONS ..... **VIII**

LIST OF FIGURES ..... **IX**

LIST OF TABLES ..... **XII**

CHAPTER 1 - INTRODUCTION **1**

1.1 BACKGROUND 1

1.2 PROJECT MOTIVATION 1

1.3 PROBLEM STATEMENT 1

1.4 TECHNICAL SPECIFICATIONS 2

1.5 DESIGN METHODOLOGY 2

1.5.1 Permanent magnet machine theory *2*

1.5.2 Analytical sizing equations *2*

1.5.3 System verification and validation *3*

1.6 DESIGN REQUIREMENTS 3

1.7 DISSERTATION OVERVIEW 3

CHAPTER 2 - LITERATURE STUDY **5**

2.1 HISTORY OF THE INDUCTION MACHINE AND PERMANENT MAGNETS 5

2.2 PERMANENT MAGNET MOTORS 6

2.2.1 Permanent magnets *6*

2.2.2 Permanent magnet materials *8*

2.2.3 Principle of operation *9*

2.2.4 Permanent magnet factors for a rotor *9*

2.2.5 Permanent magnet factors for a stator *13*

2.3 PERMANENT MAGNET MOTOR VERSUS INDUCTION MOTOR 15

2.3.1 Start-up behaviour *16*

2.3.2 Steady state operation *16*

2.4 CONCLUSION 16

CHAPTER 3 - CONCEPTUAL DESIGN **18**

3.1 STATOR STRUCTURE 18

3.2 ROTOR STRUCTURE 20

3.3 SIZING APPROACH 21

3.3.1 Rotor slot dimensions 22
3.3.2 Cogging torque reduction principles 26
3.3.3 Magnet dimensions 28
3.3.4 End ring dimensions 34
3.4 LSPMSM STRUCTURE 36
3.5 CONCLUSION 36

CHAPTER 4 - MODELLING 38

4.1 FLUX DENSITY PLOT 38
4.2 PRELIMINARY TORQUE CAPABILITY 39
4.2.1 Air gap leakage inductance 39
4.2.2 Slot leakage inductance 40
4.2.3 Tooth tip leakage inductance 41
4.2.4 End winding leakage inductance 41
4.2.5 Skew leakage inductance 42
4.2.6 Total leakage inductance 43
4.2.7 Electromechanical torque curve 43
4.3 CALCULATED EFFICIENCY 45
4.3.1 Resistive losses 45
4.3.2 Iron losses 46
4.3.3 Stray losses 48
4.3.4 Mechanical losses 48
4.3.5 Total losses and efficiency 49
4.4 EQUIVALENT ELECTRICAL CIRCUIT 49
4.5 CONCLUSION 52

CHAPTER 5 - DETAIL DESIGN 53

5.1 LEAKAGE FLUX REDUCTION 53
5.1.1 Movement of magnets 53
5.1.2 Improvement of flux barriers 54
5.1.3 Leakage flux reduction final design 56
5.2 PERMANENT MAGNET BRAKING TORQUE ANALYSIS 56
5.3 TOTAL TORQUE CAPABILITY 60
5.4 MANUFACTURING AND ASSEMBLY 61
5.4.1 Rotor laminations 61
5.4.2 Rotor bars 62
5.4.3 Final assembly 62

5.5 CONCLUSION 63

CHAPTER 6 - TESTING AND VALIDATION 64

6.1 TESTING METHODOLOGY 64
6.2 DC RESISTANCE TEST 65
6.3 BLOCKED ROTOR TEST 66
6.4 NO LOAD TEST 69
6.5 BACK-EMF TEST 71
6.6 COGGING TORQUE TEST 73
6.7 EFFICIENCY ANALYSIS 75
6.8 TORQUE ANALYSIS 75
6.9 CONCLUSION 77

CHAPTER 7 - CONCLUSION AND RECOMMENDATIONS 78

7.1 CONCLUSIONS 78
7.1.1 Design process 78
7.1.2 Fabrication process 79
7.1.3 Operation 79
7.2 RECOMMENDATIONS 79
7.2.1 Design 80
7.2.2 Fabrication 80
7.2.3 Further development 80

REFERENCES 82

APPENDIX A: FLOW DIAGRAMS 84

APPENDIX B: MECHANICAL LOSSES 87

APPENDIX D: PRESENTED ARTICLE 88

APPENDIX E: DESIGN TECHNICAL DRAWINGS 97

List of Publications

K. S. Garner and A. J. Grobler, "Rotor design of a retrofit line-start permanent magnet synchronous machine," *in Proceedings of the 23rd Southern African Universities Power Engineering Conference,(SAUPEC),* Johannesburg, January 2015.

List of Symbols

a	Number of parallel paths per winding without a commutator	
A	Area	m^2
A_{cr}	Area of rotor conductive material	m^2
A_{ur}	Area of rotor slots	m^2
b_1	Slot width	m
b_4	Slot opening width	m
B	Magnetic flux density	T
B_r	Remanence flux density	T
BH_{max}	Maximum energy product	TA/m
C_M	Torque coefficient	
$cos\varphi$	Power factor	
D	Diameter	m
E	Electric field strength	V/m
E_m	Electromotive force/ Back-emf	V
f	Frequency	Hz
h_1	Slot opening depth	m
h_4	Slot height	m
H	Magnetic field strength or magnetising force	A/m
H_c	Coercivity related to flux density	A/m
h_{mag}	Thickness of the permanent magnet	m

I	Current	A
J	Current density	A/m^2
k	Connecting factor	
k_C	Carter factor	
$k_{cu,r}$	Fill factor for copper	
k_{dv}	Distribution factor at harmonic number v	
k_{pv}	Pitch factor at harmonic number v	
k_R	Correction coefficient for slot resistance	
k_{sqv}	Skewing factor at harmonic number v	
k_X	Correction coefficient for slot inductance	
$k_w/k_{wsv}/k_{wrv}$	Winding factor for stator or rotor at harmonic number v	
K_{rs}	Referral factor for rotor parameters to stator reference frame	
l	Length	m
l'	Equivalent length	m
m	Number of phases	
M	Mass	kg
N	Number of turns of winding	
p	Number of pole pairs	
P	Power	W
q	Number of slots per pole per phase	
Q	Number of slots	
r	Radius of circle	m

R	Resistance	Ω
$R_{e\delta}$	Couette Reynolds number	
R_{fe}	Core resistance	Ω
R_m	Magnetic reluctance	A/Wb
R_r/R_2	Rotor resistance	Ω
R_s/R_1	Stator resistance	Ω
s	Slip	
$skew$	Skewing measured as the length of an arc	
T_b	Braking torque	Nm
T_{em}	Electromechanical torque	Nm
T_{max}	Maximum temperature	°C
v	Harmonic number	
V	Voltage	V
Vol	Volume	m^3
W	Coil span	m
X	Reactance	Ω
Y	Admittance	S
Z	Impedance	Ω
z_l	Number of bars of length l	
z_Q	Number of conductors in a slot	
α	Span	m
α_u	Slot angle	

δ	Air gap length	m
δ_{skin}	Depth of skin effect	m
$\Delta\alpha$	Span of each short bar creating total bar	m
Δl	Length of each short bar creating total bar	m
ξ	Reduced conductor factor	
κ	Factor for reduction of slot opening	
ψ	Flux linkage	Wb/turns
λ	Permeance factor	
η	Efficiency	
Ω	Mechanical angular velocity	
ρ	Electrical resistivity	Ωm
Φ	Magnetic flux	Wb
σ	Electrical conductivity	S/m
σ_{sq}	Skew leakage factor	
τ_p	Pole pitch	m
τ_u	Slot pitch	m
Θ_{mag}	Equivalent mmf of a permanent magnet	A
μ_0	Permeability of free space	N/A^2
μ_r	Permeability of a material relative to free space	
ω	Angular frequency in radians	rad/s

Subscripts

1	Fundamental harmonic/Stator	

	parameter
2	Rotor parameter
Al	Aluminium
av	Average
c	Coercivity, conductor
Cu	Copper
d	Direct
DC	Direct current
e	Equivalent
ef	Effective
fe	Iron
fnl	Field no load
g	Air gap
in	Line
m	Magnetising
mag	Permanent magnet
max	Maximum
nl	No load
ph	Phase
q	Quadrature
Q	Slots
r	Rotor

R	Resistance
s	Stator
skin	Skin effect relation
tot	Total
X	Reactance

List of Abbreviations

AC	Alternating current	A
Alnico	Aluminium nickel cobalt alloy	
d-axis	Direct axis	
DC	Direct current	A
FEMM	Finite Element Method Magnetics	
IEC	International Electrotechnical Commission	
LSPMSM	Line start permanent magnet synchronous machine	
M&C	Marthinusen & Courts	
mmf	Magneto motive force	
NdFeB	Neodymium Iron Boron	
NEMA	National Electrical Manufacturers Association	
PMSM	Permanent magnet synchronous machine	
q-axis	Quadrature axis	
RMS	Root Mean Square	
SmCo	Samarium Cobalt	

List of Figures

Figure 2-1: Design of the first induction motor [1] 5

Figure 2-2: B-H curve of a typical permanent magnet material 7

Figure 2-3: The effect of temperature on a material's B-H curve 7

Figure 2-4: Axial air gap orientation 10

Figure 2-5: Radial air gap orientation 10

Figure 2-6: Side view of surface-mounted permanent magnets 11

Figure 2-7: Side view of embedded permanent magnets 12

Figure 2-8: Example of a rectangular magnet 13

Figure 2-9: A typical example of the current linkage distribution of a two-pole non-salient pole motor [4] 13

Figure 2-10: An example of a slotted stator (left) and non-slotted stator (right)[8] 15

Figure 3-1: A depiction of the induction machine stator lamination used for the design 19

Figure 3-2: Stator winding layout as obtained from WEG [9] 19

Figure 3-3: Equivalent circuit of the 7.5kW, 4 pole W22 WEG induction motor [9] 19

Figure 3-4: Typical motor's natural speed-torque curve 20

Figure 3-5: Current density effect on slot size 23

Figure 3-6: Rotor slot shape chosen for the retrofit LSPMSM 23

Figure 3-7: Skin effect illustration on a conductor 24

Figure 3-8: Skin effect on a rotor slot 24

Figure 3-9: Designed rotor slot 26

Figure 3-10: Equivalent magnetic circuit of the retrofit LSPMSM conceptual design 29

Figure 3-11: Simplified equivalent magnetic circuit of the retrofit LSPMSM conceptual design 29

Figure 3-12: Load line of NdFeB 48 30

Figure 3-13: Comparison of B-H curve of NdFeB 48 at 20°C and 60°C 33

Figure 3-14: Energy product of NdFeB 48 at 60°C 33

Figure 3-15: Load line of magnetic circuit intersecting with load line of the permanent magnet 34

Figure 3-16: End ring dimensions 35

Figure 3-17: LSPMSM retrofit conceptual design FEMM model 36

Figure 4-1: Close-up of quarter section of flux density plot 39

Figure 4-2: The slot types applicable to the retrofit design 41

Figure 4-3: The dimensioning of an end winding [4] 41

Figure 4-4: Electromechanical torque versus slip of the retrofit LSPMSM design 44

Figure 4-5: Electromechanical torque versus slip of the WEG WQuattro motor [16] 44

Figure 4-6: Simulated efficiency curve determined from ANSYS Mawxell© program 49

Figure 4-7: Equivalent circuit used to determine R_{fe} 51

Figure 4-8: Equivalent circuit for the LSPMSM retrofit conceptual design 52

Figure 5-1: Close-up of quarter section of flux density plot with magnets moved closer to the air gap 54

Figure 5-2: Flow diagram for the modification of flux barriers and reduction of leakage flux 54

Figure 5-3: Close-up of quarter section of flux density plot with first modification of flux barriers ... 55

Figure 5-4: Close-up of quarter section of flux density plot with second modification of flux barriers 55

Figure 5-5: Flux density plot after leakage flux reduction 56

Figure 5-6: Relationship between volume of magnetic material and acceleration torque [20] 56

Figure 5-7: Flux linkage of LSPMSM FEMM model 57

Figure 5-8: Back-emf of LSPMSM FEMM model 58

Figure 5-9: Simulated back-emf voltages at no load 58

Figure 5-10: Braking torque generated by the permanent magnets 59

Figure 5-11: Total torque curve for retrofit LSPMSM design 60

Figure 5-12: Comparison between calculated and simulated torque curves 61

Figure 5-13: Rotor lamination 61

Figure 5-14: Rotor stack with shaft 62

Figure 5-15: Final assembly and test setup 62

Figure 6-1: Equivalent circuit of the DC resistance test 65

Figure 6-2: Equivalent circuit of the blocked rotor test 66

Figure 6-3: Equivalent circuit of the no load test 69

Figure 6-4: Calculated back-emf at no load with reduced magnet axial length 73

Figure 6-5: Simulated back-emf at no load with reduced magnet axial length 73

Figure 6-6: Cogging torque test diagram 74

Figure 6-7: Measured cogging torque of the LSPMSM 74

Figure 6-8: Comparison of measured and simulated efficiency 75

Figure 6-9: Torque comparison between design and performance testing 76

List of Tables

Table 1: Characteristics of main types of permanent magnets [5] 8

Table 2: A comparison between the 7.5 kW WQuattro LSPMSM and a 7.5 kW induction motor [9] . 16

Table 3: Characteristics of the 7.5kW, 4 pole W22 WEG induction motor stator [9] 18

Table 4: Equivalent circuit's parameters as obtained by WEG [9] 20

Table 5: Suggested current densities for the LSPMSM [4] 21

Table 6: Reduced conductor factor versus slip 25

Table 7: Dimension of rotor slot to reduce skin effect 26

Table 8: NdFeB 48H 30

Table 9: Stator and rotor leakage inductances and impedances for the retrofit LSPMSM 43

Table 10: Torque summary of the retrofit LSPMSM design and the WEG WQuattro 45

Table 11: The properties of the conductor used in the rotor 46

Table 12: The properties of the conductor used in the stator 46

Table 13: Segregation of sections to determine iron losses 47

Table 14: Lamination material specifications [19] 47

Table 15: Iron losses calculated for each section 48

Table 16: Calculated mechanical losses 49

Table 17: Calculated equivalent circuit parameters for the LSPMSM 51

Table 18: Results of DC resistance test 66

Table 19: X1 and X2 relationship according to NEMA classes 68

Table 20: Results of the blocked rotor test 68

Table 21: Results of the no load test 71

Table 22: Properties and dimensions of NdFeB 25BH 72

Chapter 1 - Introduction

This chapter introduces the project overview and motivation. The problem statement will be formulated and the design methodology to be used will be explained.

1.1 Background

Our energy resources are under tremendous pressure with society's ever increasing need for electricity. Resources are seen to be dwindling and the effect of our power generation has become evident on the environment. There is an urgent need to look at how we are expending all the energy generated and try to reduce our energy consumption.

Studies have indicated that 65% of electrical energy is converted to heat and mechanical energy by electric motors. Most of these motors are three-phase induction motors used in fan and pump applications [1]. Constructing motors with better efficiency can result in a reduction in energy consumption and cost savings to the consumer. A 3% increase in motor efficiency can yield a 2% saving in energy consumed and reduce carbon emissions [1].

1.2 Project Motivation

One method of increasing a motor's efficiency is to use permanent magnets in the construction of the motor's core. Permanent magnets eliminate the rotor excitation losses experienced by standard induction machines, thereby increasing the motor's efficiency [2].

This project originated from a petro-chemical company's need to improve the efficiency of its load. Induction motors constitute 70% of the company's load profile, indicating a significant potential for savings. However, the cost of the solution must not outweigh the eventual savings.

1.3 Problem Statement

The problem is to produce a prototype retrofit machine utilising permanent magnets. The prototype will lay the foundation for future optimisation strategies. The design should provide improved efficiency with a minimum effect on the motors already operating in industry. This will provide industrial companies with a simple yet effective solution to improve energy efficiency without replacing an entire installation.

A retrofit design of a three-phase induction motor's rotor is considered for this project. The proposal is to substitute the standard rotor of an induction motor with a permanent magnet core. The stator and frame of the induction motor will be kept intact.

A retrofit design is considered because of the ease of manufacturing for motor suppliers. A motor supplier will not need to replace its entire production line, but only replace its rotor design. The retrofit will also allow induction motors currently operating in industrial applications to switch to a permanent magnet solution with minimal impact. A motor with increased efficiency can be achieved without increasing the size of the motor.

1.4 Technical specifications

A 525V, 7.5 kW, 4 pole permanent magnet motor, called WQuattro, was purchased from WEG for this research. This motor was also developed by replacing the induction motor's rotor with a rotor fitted with permanent magnets. Its operation has not met the developer's required specifications and as a result, WEG will not develop the technology further, but is supporting this project for a better solution.

This project will redevelop the rotor of this motor.

1.5 Design Methodology

A structured project plan and the continuous acquisition of knowledge are integral components of a successful project. These two components allow the researcher to address problems effectively and timeously.

1.5.1 Permanent magnet machine theory

Permanent magnet machine theory provides the knowledge on the characteristics of permanent magnets and the behaviour of these magnets in motor applications. The research into the theory will lay the foundation for selecting the best material and design for the rotor.

1.5.2 Analytical sizing equations

An analytical model of the rotor's dimensions will be generated to characterise the machine. Fundamental machine equations will be used to compile the model and the operation of the model will be compared with induction machine behaviour. A model will be constructed in FEMM, a finite element method magnetics program, to determine the flux density.

1.5.3 System verification and validation

The retrofit prototype will be constructed in accordance with the specifications. ANSYS Maxwell®, an electromagnetic field simulation program, will be used for verification purposes. The prototype will be tested in the laboratory along with a 7.5 kW induction machine for validation purposes.

1.6 Design Requirements

The specifications for the retrofit machine are as follow:

1. Deliver 7.5 kW of electric power
2. Existing stator and frame must remain unchanged
3. Specifications of the permanent magnet rotor will be determined

1.7 Dissertation Overview

Chapter 2: This chapter comprises of the literature study. It deals briefly with the history of permanent magnets and then focuses on the operating principles of permanent magnets. The factors for rotor and stator selection are discussed and a rough comparison is investigated between an existing permanent magnet motor design and an induction motor.

Chapter 3: The conceptual design of the retrofit PMSM is discussed in Chapter 3. This includes the sizing approach for the rotor slots which form the induction machine of the prototype and the design of the permanent magnets which forms the PMSM design of the prototype.

Chapter 4: A model of the prototype is developed in FEMM. The theoretical results of the torque capability, efficiency and equivalent electric circuit of the design are determined. A recommendation for improvement on the design is given for the detail design covered in the next chapter.

Chapter 5: Chapter 5 deals with the detail design, paying special attention to optimisation of the flux density plot of conceptual design. The braking torque of the permanent magnets and the effect on the design's torque curve is analysed.

Chapter 6: Chapter 6 handles the testing of the final fabricated design in a laboratory. This allows validation of the results against the theoretical results obtained through calculations and simulations.

Chapter 7: The final results are discussed in further detail and recommendations for further opportunities are provided.

Chapter 2 - Literature Study

This chapter introduces the theory and concepts required to produce an effective design. The basic principles and operation of permanent magnets are discussed, leading to the factors that influence stator and rotor design. A comparison between line start permanent magnet motors and induction motors is also briefly discussed.

2.1 History of the induction machine and permanent magnets

The 1800s announced the arrival of the synchronous and induction motors after the discovery of electromagnetic induction. The initial motor designs had large air gaps and could only develop a small torque. Figure 2-1 illustrates the design of the first induction motor. At the time the torque the motor developed was only able to rotate the motor without a load. Since then, there have been numerous developments and improvements to the basic design. Eventually the later models were able to operate on load with smaller air gaps and improved efficiency.

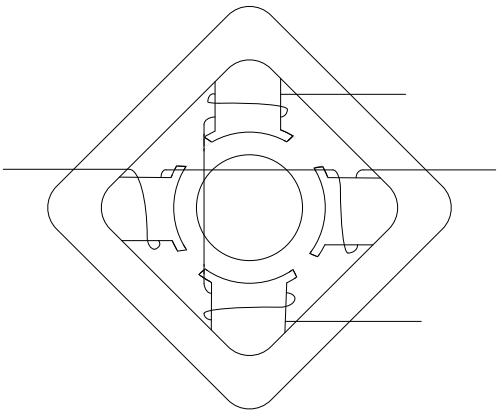

Figure 2-1: Design of the first induction motor [1]

After the many improvements in the field, the most popular electric motor has been the cage induction motor. This motor has a simple construction, less maintenance than a DC machine and is moderately reliable in comparison with a DC machine. Unfortunately, even today the induction motor has lower efficiency and power factor than a synchronous motor [1]. With the increasing need to look at energy efficiency, these drawbacks call for a new development in motor design. The cage induction motor has reached the pinnacle in its design and is restrained with regards to further improvements to reduce losses.

The use of permanent magnets in electrical machines dates as far back as the nineteenth century. It was discovered that the use of permanent magnets in an electrical machines construction can result in

improved performance, greater power density, simplified construction and a reduction in losses [1]. Carbon, cobalt and wolfram steels were the only permanent magnets available for many decades but their magnetic properties were poor. The lack of good quality magnets able to maintain magnetisation at the time dampened the enthusiasm around their use over electromagnetic excitation systems [1].

It was in the 1960s that a vast improvement in the permanent magnet field was made [3]. Ferrite quickly replaced the previous metals in the design because of its abundance and low production cost. Its maximum energy product is poor and cannot be used for high temperature applications, but it is still used today in many small applications because of its low cost. Further developments lead to compounds of rare earth metals with higher energy products using more common materials. The rare earth permanent magnets are not as abundant as Ferrite, but have far better electromagnetic characteristics. The development of better permanent magnet materials has increased the use of permanent magnet motors in industry.

At present, permanent magnets are becoming more readily available. The developments in permanent magnets until now have allowed for cost effective motor designs which yield greater power efficiency.

2.2 Permanent Magnet Motors

2.2.1 Permanent magnets

A permanent magnet can maintain its own persistent magnetic field. Permanent magnets are generally described by their magnetic behaviour in terms of remanence, coercivity and maximum energy product.

Remanence refers to the flux density remaining in a permanent magnet after saturation while coercivity speaks of the negative field strength required to reduce this remanence to zero. The maximum energy product indicates the maximum energy the permanent magnet is able to produce.

Figure 2-2 is an example of a B-H curve for a permanent magnet material. The initial magnetization is achieved by applying an electric field to the permanent magnet material. When the field is taken away, the material recoils or demagnetises along the upper curve in the second quadrant. This curve is called the demagnetization curve and this is where a permanent magnet is generally used. B_r and H_c indicate the remanence and coercivity of a permanent magnet material respectively.

The maximum energy product BH_{max} is achieved at the point where the B-H hyperbola is tangent to the demagnetization curve. The higher the maximum energy product of a permanent magnet material, the less material can be used.

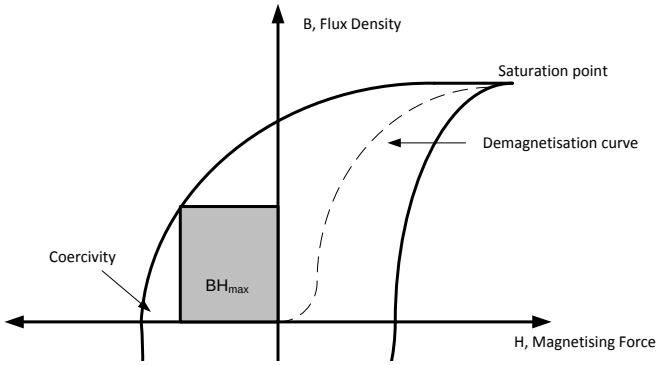

Figure 2-2: B-H curve of a typical permanent magnet material

The B-H curve of a permanent magnet material varies with temperature. The magnetic moment fluctuates when the temperature of the material changes from ambient temperature to a higher temperature. This fluctuation in the magnetic moment influences the demagnetization curve [1] [4].

The temperature at which a magnet loses its magnetisation is called the Curie temperature. Though the material is still a magnetic material, it would have completely demagnetized at this point. The effect of the heating and cooling rates during the temperature cycle can also cause structural damage to the magnetic material [3]. The effects of temperature on a permanent magnet material's B-H curve can be seen in Figure 2-3. Neodymium Iron Boron was used for the illustration and will be discussed in further detail in Section 2.2.2.

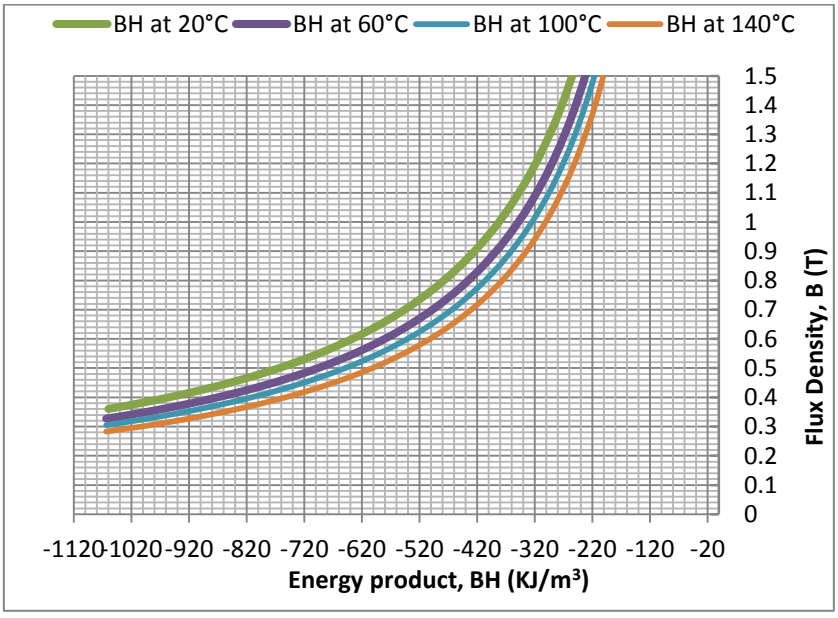

Figure 2-3: The effect of temperature on a material's B-H curve

2.2.2 Permanent magnet materials

There are four types of commercially available permanent magnets based on their material composition [5]:

- Ferrite (also known as Ceramic)
- Alnico (AlNiCo)
- Samarium Cobalt (SmCo)
- Neodymium Iron Boron (NdFeB)

Ferrite and Alnico magnets have been around since the 1930s and are still used extensively because of their low cost as stated previously. NdFeB and SmCo are rare earth permanent magnets and are be created by bonding or sintering. When the magnets are bonded a non-magnetic, non-conductive resin is mixed with the material. The resultant magnet has a low performance rating because of the high percentage of non-magnetic material used. Sintering uses only magnetic material in the process and thus yields a high performance permanent magnet.

While SmCo has a greater inherent stability, NdFeB yields the highest magnetic properties of all the available magnets at room temperature [1]. Table 1 illustrates the characteristics of the main types of permanent magnets available.

Table 1: Characteristics of main types of permanent magnets [5]

Material	Grade	$\mathbf{B_r}$ (G)	$\mathbf{BH_{max}}$ (MGOe)	$\mathbf{H_c}$ (KOe)	T_{max} (°C)
Ferrite	5	3950	3.4	2400	400
Alnico	5	10900	3.9	620	540
Alnico	8	8200	5.3	1650	540
SmCo	20	9000	20	8000	260
SmCo	28	10500	28	9500	350
NdFeB	N45	13500	45	10800	80
NdFeB	33UH	11500	33	10700	180

There are numerous advantages and disadvantages associated with each type of permanent magnet. When selecting a material, it is important to consider the availability of the material, the cost and the

constructability of the design. NdFeB will be used for the retrofit LSPMSM because it has the highest magnetic properties of all the available magnets at room temperature.

2.2.3 Principle of operation

In a permanent magnet motor, a winding acts as an electromagnet when it conducts current. The permanent magnet is attracted to the electromagnetic coil, causing the motor to rotate. When the supply is removed, the magnetic qualities of the winding are lost and the motor stops.

The line start permanent magnet synchronous machine uses the rotor cage to develop a starting torque. The magnets supply the magnetic field in the air gap to induce the voltage in the armature windings. The starting torque pulls the rotor into synchronism while the permanent magnets generate the synchronous torque required for steady state operation. In this manner, an asynchronous start with a synchronous steady state operation is achieved.

Because the motor operates as a synchronous machine, the current induced in the rotor is zero and the copper losses in the rotor cage are negligible.

The disadvantage of a permanent magnet motor is that the magnets generate a braking torque which decreases the starting torque during the starting period. This reduces the motor's ability to synchronize a load during line starting. Using the cage winding of an induction motor for the retrofit design will assist in providing sufficient accelerating torque to overcome the braking torque and the load's inertia [4].

2.2.4 Permanent magnet factors for a rotor

The rotor of a permanent magnet motor is manufactured from magnetic flux-carrying steel to concentrate the magnetic flux generated by the permanent magnets.

The use of permanent magnets in motors allows for a wide variety of topologies. The magnets can be used in various shapes, positions and orientation to obtain the best topology for an application.

The following basic factors are considered when designing the magnets of a rotor for a LSPMSM:

- Magnetization
- Permanent magnet orientation
- Permanent magnet sizing

2.2.4.1 Magnetization

There are two main topologies that provide the best solution for most applications: radial flux and axial flux machines. Radial and axial flux permanent magnet machines are described by the orientation of the air gap with respect to the rotational axis. The air gap separates the rotor and the stator and is kept as small as possible to generate a strong magnetic field.

In an axial flux permanent magnet machine the magnetic flux generated is parallel to the rotational axis as can be seen in Figure 2-4.

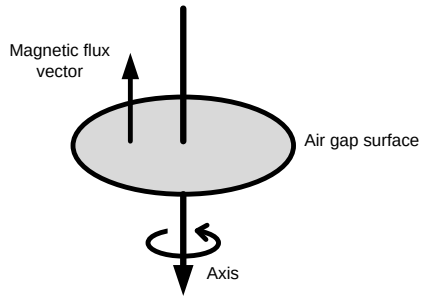

Figure 2-4: Axial air gap orientation

Axial flux permanent magnet machines are generally used for low speed/high torque operations [4]. Their design allows a high power/weight distribution which results in the reduction of core material. The air gap of this type of machine is planar and very easily changeable. This means that the losses in this machine can be greatly reduced.

The heat transfer of an axial flux permanent magnet machine is less effective than the radial flux topology. This implies that its electrical loading cannot be extremely high [4] [6].

The magnet axes of a radial flux permanent magnet machine are produced radially or perpendicular to the rotational axis as illustrated in Figure 2-5.

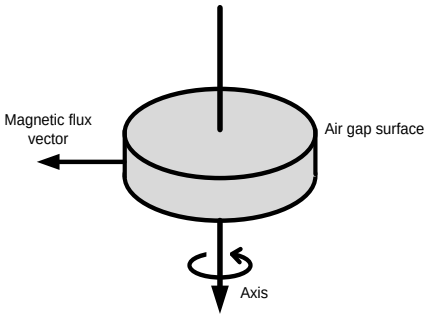

Figure 2-5: Radial air gap orientation

The radial flux permanent magnet machine is typically used for applications requiring high speed operation [4]. It has a higher torque capability than an induction machine but it is also lower than that of an axial flux permanent magnet machine. This machine has long end windings when the diameter per axial length is small, making it susceptible to high copper losses. The air gap of a radial flux permanent magnet machine is very large compared to its axial flux counterpart and therefore has a lower flux density.

2.2.4.2 Permanent magnet orientation

Permanent magnets can be mounted on the rotor in various presentations. The layouts of the magnets can be described in two categories: surface-mounted or embedded.

As the name implies, the magnets of a surface-mounted permanent magnet motor are glued on the surface of the machine's rotor. This design is represented in Figure 2-6. This type of layout is commonly used because its manufacturing and assembly are very simple. The rotation speed of such a machine is limited because of the effect of centrifugal force on the permanent magnets.

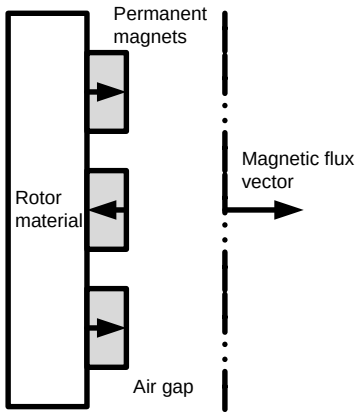

Figure 2-6: Side view of surface-mounted permanent magnets

An embedded permanent magnet motor has its magnets buried inside the rotor structure as illustrated in Figure 2-7. This design allows for a smaller construction and a reduction in total material used. It can be used at high speeds and has a reluctance torque that is not present in the surface-mounted counterpart [2]. However, the manufacturing and assembly of the machine is much more complex because of the fine tolerances required for embedded magnets.

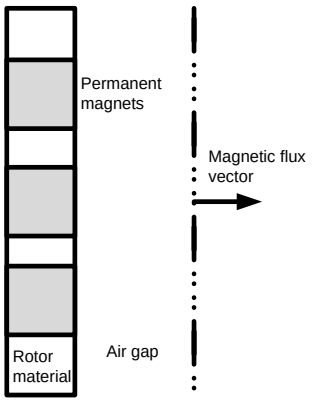

Figure 2-7: Side view of embedded permanent magnets

2.2.4.3 Permanent magnet sizing

Permanent magnets are sized for a specific application. The dimensions of the magnets will influence the amount of magnetic flux a material can generate.

The magnetic flux density B_{mag} is dependent on a material's permeability $\mu_r\mu_o$, and field intensity H_{mag} illustrated by

$$B_{mag} = \mu_r \mu_o H_{mag}. \tag{2.1}$$

The material's relative permeability, also known as recoil permeability, is represented by μ_r and the free-space permeability is μ_o. H is a negative value because the operating point of a permanent magnet material is in the second quadrant.

The reluctance of a material represents its ability to store magnetic energy. It is akin to electric resistance, so the lower a material's reluctance the more magnetic energy it is capable of storing. The reluctance $R_{m,mag}$ is a function of a material's length l and area A. It is represented by

$$R_{m,mag} = \frac{l}{\mu A}. \tag{2.2}$$

Using a rectangular piece of magnetic material as depicted in Figure 2-8 as an example, the magnetic flux density would be given by

$$B = B_r + \mu_r \mu_o H. \tag{2.3}$$

B_r is the inherent flux density of the magnetic material specified in its datasheet. The magnetic flux delivered by the material is then calculated by

$$\Phi = BA. \tag{2.4}$$

It is important to note that these calculations are a first order approximation and ignore factors such as leakage flux and condensing of flux across an air gap.

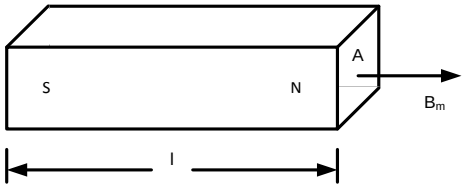

Figure 2-8: Example of a rectangular magnet

2.2.5 Line-start permanent magnet factors for a stator

2.2.5.1 Stator winding

A stator consists of a core manufactured from cast iron or laminations and copper windings. The stator design of a LSPMSM is approximately the same as for an induction machine. Special attention is paid to the design of the cage winding to enable the motor to be line-started. This is due to the fact that the permanent magnets will generate a braking torque that will negatively impact the motor's torque curve.

An induction motor's stator winding is classified as a poly-phase distributed rotating-field slot winding. The distributed slot windings and the constant length of the air gap are used to create a cosinusoidally distributed flux density in the air gap [4]. A cosinusoidal distribution is used because it reaches maximum on the direct axis where the angle is zero. Figure 2-9 displays an example of a cosinusoidal distribution of a rotor.

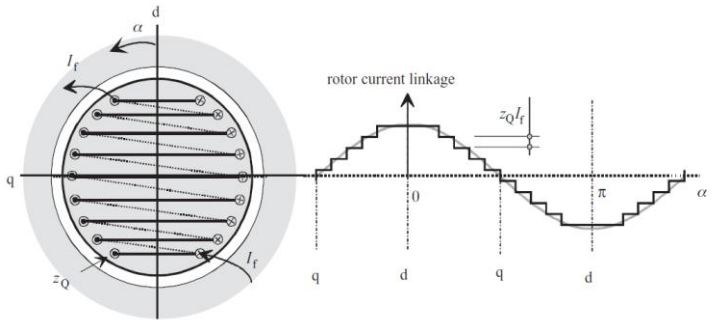

Figure 2-9: A typical example of the mmf distribution of a two-pole non-salient pole motor [4]

The variable z_Q refers to the number of conductors in each slot. An excitation current I_f flows through the conductors and this generates the mmf displayed. Two very important elements of a slot winding are the slot pitch τ_u and the slot angle α_u. These elements are a factor of the air gap diameter D and the number of slots Q as indicated by

$$\tau_u = \frac{\pi D}{Q}, \tag{2.5}$$

$$\alpha_u = \frac{2\pi p}{Q}. \tag{2.6}$$

The slot pitch of a non-salient pole winding is constant and thus the sum of the currents in the conductors has to have a different magnitude in different slots to achieve the cosinusoidal distribution. The current flowing in each conductor is the same so the number of conductors in each slot is the only element which can be varied. Varying the value of z_Q in the different slots can improve the stepped waveform response to better simulate a cosinusoidal shape.

2.2.5.2 Stator slots

The laminations of a stator can be manufactured with or without teeth. A stator design with teeth is referred to as a slotted stator, while a design without teeth is called a non-slotted stator.

The teeth of a slotted stator carry the magnetic flux and hold the windings in place. The teeth are, however, difficult to manufacture because of the high tolerances required. A manufactured example of a slotted stator is depicted on the left of Figure 2-10. The greater flux density achieved also implies that this design has high iron losses [7].

The stator depicted on the right of Figure 2-10 presents a manufactured example of a non-slotted stator. A non-slotted stator is easier to manufacture than a slotted stator. With a non-slotted stator, the copper windings are placed in the air gap. This makes the air gap larger which increases the reluctance of the machine. A larger reluctance lowers the flux and back-emf. To achieve the same back-emf as the slotted stator counterpart, more windings are required which means that more copper is required when compared to the slotted stator. The magnetic flux has to cross a larger non-magnetic medium resulting in greater flux concentration [7]. Unfortunately the increase in copper implies an increase in copper losses. Thicker permanent magnet material must be used in this design, increasing the overall cost. Non-slotted stators require a mechanism to keep the stator in place. This mechanism can be difficult to achieve as well as expensive.

In order to determine the size of the stator slots, the stator current must first be determined. The stator current is a factor of the shaft power P, the stator phase voltage U_{sph}, the efficiency η and the power factor $cos\varphi$. This is covered in more detail in Chapter 3.

Figure 2-10: An example of a slotted stator (left) and non-slotted stator (right)[8]

2.3 Permanent magnet motor versus induction motor

This section will look at the comparison between the 7.5 kW WEG WQuattro LSPMSM and a 7.5 kW, design class B, premium efficiency induction motor. The WQuattro motor is also a hybrid comprising of an induction motor and a permanent magnet motor. Table 2 summarises the differences between the WQuattro and the equivalent induction motor. The results displayed were gathered from the respective datasheets [9].

The data in Table 2 indicates that the WQuattro provides at least a 2.5% increase in efficiency. As stated in Section 1.2, this increase in efficiency can lead to a significant reduction in energy consumption across a large industrial application.

Table 2: A comparison between the 7.5 kW WQuattro LSPMSM and a 7.5 kW induction motor [9]

Parameter	WEG WQuattro motor	Induction motor
Power factor at 50% and 100% load	0.77 and 0.93	0.71 and 0.86
Efficiency at 50% and 100% load	90.5% and 93%	89% and 90.4%
Locked rotor torque and	380 Nm	250 Nm
Breakdown torque	220 Nm (at 80% rated speed)	300 Nm (at 60% rated speed)
Rated current	9.52 A	10.6 A
Speed	1500 rpm	1465 rpm

2.3.1 Start-up behaviour

A permanent magnet synchronous machine lacks the starting capability of the induction motor due to its braking torque. However, with a carefully developed cage winding, the LSPMSM overcomes this phenomenon. This will be discussed further in Chapter 5.

2.3.2 Steady state operation

The LSPMSM and the induction machine reach steady state operation at approximately the same time. The LSPMSM has a 3% higher efficiency than the induction machine during steady state operation.

2.4 Conclusion

The literature indicates that a LSPMSM can provide a more efficient solution over an induction machine counterpart. There is room for improvement in terms of the machine's torque profile and this will be a focus point for analysing the retrofit design. The retrofit design will only focus on designing the rotor and thus the following factors are already known:

- Direction of magnetization
- Dimensions of the stator
- The size and quantity of the stator slots
- Number of poles
- Voltage and frequency

- Rated torque required

A conceptual design will be developed and analysed in Chapter 3.

Chapter 3 - Conceptual Design

This chapter develops a conceptual design using the information gathered from the literature study. The sizing approach focuses on the rotor slot design and the design of the permanent magnets. The flow diagram describing the thought process for the conceptual design is displayed in Figure A - 1 in Appendix A.

3.1 Stator Structure

The stator design of the machine is fixed and only the rotor will be designed. The characteristics of the stator of the 7.5 kW, 4 pole WEG motor with W22 frame size are described in Table 3. The data, and permission to use the data, has been obtained from WEG [9].

Table 3: Characteristics of the 7.5kW, 4 pole W22 WEG induction motor stator [9]

Characteristics	Value
Rated power	7.5 kW
Power factor	0.85
Stator outer diameter	220 mm
Stator inner diameter	150 mm
Axial length	170 mm
Number of stator slots	48
Number of conductors per slot	33
Number of parallel branches	1
Air gap length	0.5 mm
Effective axial length, l'	171
Rotor inner diameter	149 mm

Figure 3-1 depicts the stator lamination to be used in the retrofit LSPMSM design. The winding layout of the stator is depicted in Figure 3-2 as obtained from WEG [9]. The winding consists of a single layer is full-pitched, meaning that the distribution of the zones among the phases is equal.

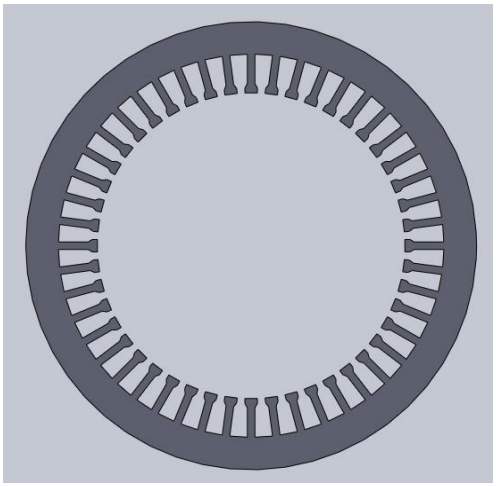

Figure 3-1: A depiction of the induction machine stator lamination used for the design

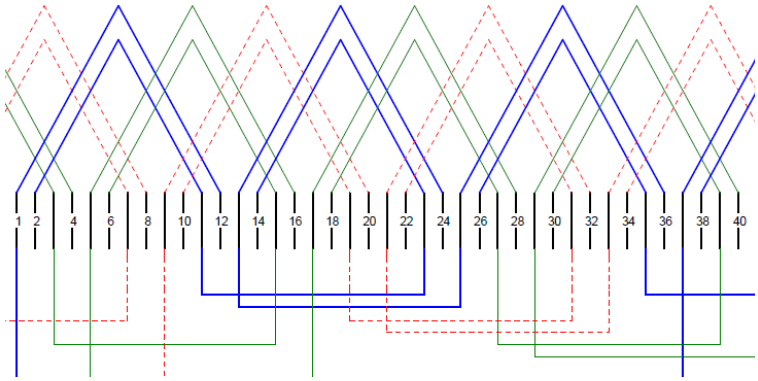

Figure 3-2: Stator winding layout as obtained from WEG [9]

The equivalent circuit for the motor is displayed in Figure 3-3 and the values of the parameters are listed in Table 4 [9]. The equivalent circuit must be modified for the addition of the permanent magnets. This will not affect the stator impedance because no changes are made to the stator or to the air gap. The addition of the permanent magnets affects the impedance of the rotor.

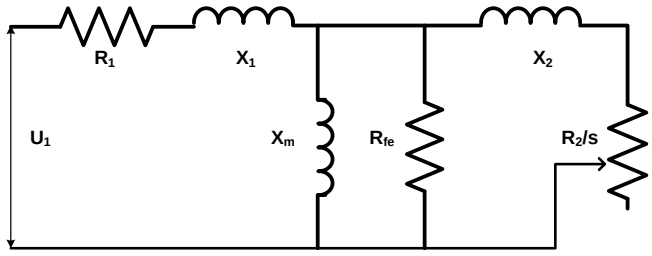

Figure 3-3: Equivalent circuit of the 7.5kW, 4 pole W22 WEG induction motor [9]

Table 4: Equivalent circuit's parameters as obtained by WEG [9]

Parameter	Value
R_1	2.383 Ω
R_2	1.622 Ω
R_{fe}	5349.904 Ω
X_1	5.748 Ω
X_2	7.722 Ω
X_m	195.908 Ω

3.2 Rotor Structure

The LSPMSM motor is intended to be used in a pump application because fans and pumps constitute most of the applications where induction motors are applied. Pump applications require motors that operate in their high speed/low torque area of the speed-torque curve as displayed in Figure 3-4 .

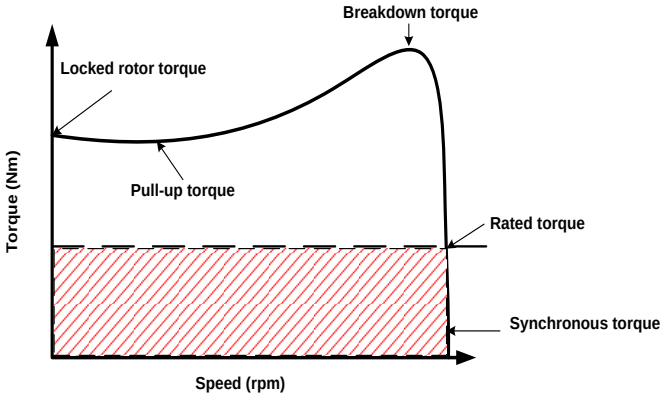

Figure 3-4: Typical motor's natural speed-torque curve

Embedded magnets are chosen for the rotor structure to maintain the axial length of 170 mm. As shown in Section 2.2.4.2, embedded magnets allow for a smaller construction because the magnets are fitted inside the rotor steel. Surface-mounted magnets add to the axial length of the rotor, making it longer. This means that a longer stator is required to facilitate the longer rotor.

A radial flux permanent magnet configuration is the only option available for the retrofit design because the stator has been developed for radial flux.

3.3 Sizing Approach

When designing an electrical machine, the following parameters have to be determined to yield an optimum design [4]:

- Outer diameter and length of the stator stack
- Width and height of the stator slot
- Diameter and length of the air gap
- Width and height of the rotor slot
- Pole pair number and frequency

Only the width and height of the rotor slot will need to be determined for the retrofit design. The other parameters are fixed since they relate to the stator. The LSPMSM design will require that the dimensions of the magnets need to be determined.

A LSPMSM is a hybrid between an induction machine and a synchronous machine. The flux and current densities for the retrofit design will be established by the limits for the induction machine as well as the salient pole synchronous machine.

Table 5 indicates the suggested current densities [4]. Higher values can be used, but this will cause some parts of the material to saturate and thereby reduce efficiency.

Table 5: Suggested current densities for the LSPMSM [4]

Current density (A/mm^2)			
	Asynchronous machine	Salient pole synchronous machine or LSPMSM	LS PMSM
J (A/mm^2)	3 – 8 (Copper rotor winding)	4 – 6.5 (Field winding)	4 – 6.5
J (A/mm^2)	3 – 8 (Aluminium rotor winding)	2 – 3.5 (Multi-layer winding)	3 – 3.5
J (A/mm^2)	3 – 6.5	2 – 4 (Single layer winding)	3 – 4

3.3.1 Rotor slot dimensions

The number of rotor slots is chosen by considering the number of poles and the number of stator slots. The stator and rotor slots should not be equal otherwise the slots will align like a stepper motor and have large cogging torque. The number of rotor slots is chosen as 30 [4]. The lowest slot number recommended was chosen because of the size of the rotor diameter. Too many slots would not allow sufficient spacing between rotor slots and make the manufacturing more complex.

The rotor slot area is calculated by determining the stator and rotor currents. The stator current I_s is calculated using the shaft power P, the number of phases m, the efficiency η, the power factor $cos\varphi$ and the stator phase voltage V_{sph}

$$I_s = \frac{P}{m\eta V_{sph}\cos\varphi}. \tag{3.1}$$

The rotor current I_r is a factor of the stator current and is determined by

$$I_r = \frac{z_Q}{a}\ \frac{Q_s}{Q_r}\ I_s\cos\varphi \tag{3.2}$$

where z_Q is the amount of conductors per slot, a is the number of parallel paths in the windings and Q_s and Q_r represent the number of stator slots and rotor slots respectively.

The area of the conductive material in the slot must be calculated in order to calculate the slot area. The value of J_r is chosen based on the best practices applied in Table 5 as 4 A/mm^2. Choosing a higher current density yields a smaller cross-sectional area of the conductive material and thus a higher resistance. A higher rotor resistance provides an increased starting torque because torque is proportional to the rotor resistance at low values of slip.

The area of the rotor's conductive material A_{cr} is given by [4]

$$A_{cr} = \frac{I_r}{a_r J_r}. \tag{3.3}$$

The area of the rotor slots A_{ur} is then calculated as follows

$$A_{ur} = \frac{z_Q A_{cr}}{k_{cu,r}}. \tag{3.4}$$

The fill factor $k_{cu,r}$ is dependent on the winding material and winding type of the machine. A space factor is a ratio of the area of conductive material in a slot and the area of the slot itself. Aluminium casted bars will be used for the design making $k_{cu,r} = 1$ [4].

The area of the rotor slot is then calculated as 97.56 mm^2. If a current density of $J_r = 3$ A/mm^2 was selected, the area of the conductive material required would increase to 130 mm^2. A smaller area of conductive material results in less material being used. The effect of the current density on the slot size is displayed in Figure 3-5. The dimensions of the rotor slot need to be determined to form the appropriate shape.

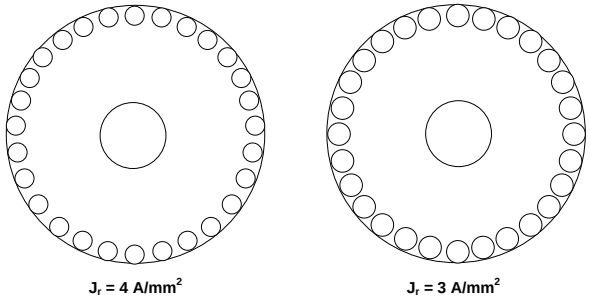

Figure 3-5: Current density effect on slot size

Most slot shapes can be grouped into pear-shaped, trapezoidal or circular. Pear-shaped slots are more effective at weakening torque ripples, but the torque results between the three types vary marginally on the fundamental flux density [9]. Torque ripple is a result of cogging torque, which is discussed in Section 3.3.2.

A circular slot shape, depicted in Figure 3-6, was chosen for the design which would be easier to manufacture and assemble.

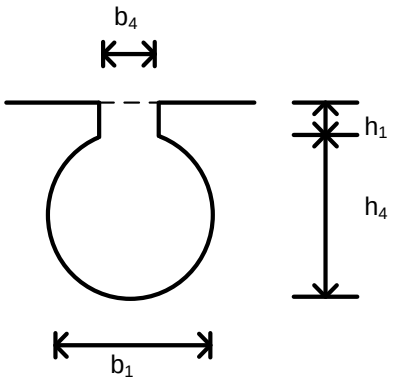

Figure 3-6: Rotor slot shape chosen for the retrofit LSPMSM

A radius of 10 mm was selected to satisfy the calculated area required, while the depth and slot opening can only be finalised once the skin effect on the slot shape is considered. Skin effect arises when an alternating current distributes through a conductor such that the current density is largest near the surface of the conductor and decreases through the depth of the conductor. The current thus flows mainly at the skin of the conductor, termed the skin depth, as indicated in Figure 3-7. Skin effect increases the effective resistance of the conductor, thereby decreasing the current-carrying capacity of the conductor.

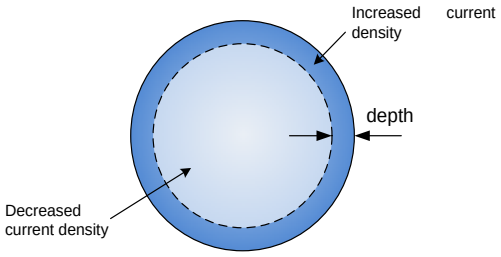

Figure 3-7: Skin effect illustration on a conductor

The rotor slots of a motor are affected in a similar way. Under nominal operating conditions, the current in the rotor slot cross-section is uniformly distributed. During a non-steady-state operation, such as starting, the rotational speed does not correspond to the number of revolutions of the stator rotary field and high slip values occur. At a low rotational speed, the rotor current frequency is increased and the current in the rotor slots is displaced in a radial direction towards the air gap. This effect is caused by the slot leakage field around the slots.

The rotor slot is modelled into several elements as partial coils to mimic the effect of the current distribution, as depicted in Figure 3-8 [11]. The coil located deepest in the slot experiences a stronger leakage field and has the highest leakage inductance in comparison to the coils locates close to the air gap. The leakage reactance is more prominent and the rotor current concentrates in the upper coils. The conductive cross-section of the slot is decreased and the resistance of the slot increases.

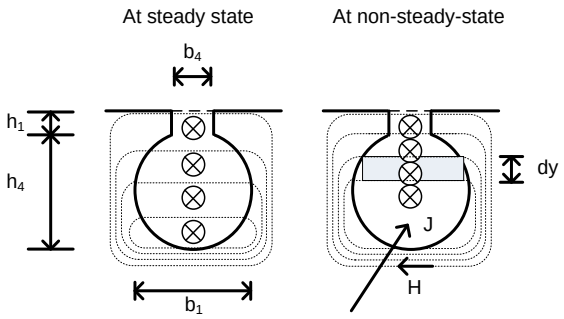

Figure 3-8: Skin effect on a rotor slot

Ampère's law is applied to the shaded area in Figure 3-8 following the derivation in [4], the reduced conductor height, ξ, is calculated as follows

$$\xi = h_4 \quad = h_4 \sqrt{\frac{s\omega\mu_0\sigma_{Al}}{2}\frac{b_c}{b}} \tag{3.5}$$

The width of the slot is defined as b and the width of the conductor in the slot is b_c. Besides the dimensions of the slot, the reduced conductor factor depends on the slip s, the radial frequency ω and the conductivity of the material σ_{Al}, which is aluminium in this case. The variable b is equal to b_1 for the retrofit design. The value of the reduced conductor factor for some values of slip is displayed in Table 6. This indicates that at high values of slip, the slot's conductive area is effectively reduced by 10-17%.

Table 6: Reduced conductor factor versus slip

Slip, *s*	**Reduced conductor factor, ξ**
1	0.1766
0.9	0.1249
0.3	0.1019
0.2	0.0588
0.1	0.0558

The rotor slots need to be corrected accordingly to minimise the skin effect. The correction coefficients for the slot resistance k_R and the slot inductance k_X are determined by [4] as follows

$$k_R = \xi \frac{\sinh 2\xi + \sin 2\xi}{\cosh 2\xi \quad \cos 2\xi} = \frac{R_{ac}}{R_{dc}} \tag{3.6}$$

$$k_X = \frac{3}{2\xi}\frac{\sinh 2\xi \quad \sin 2\xi}{\cosh 2\xi + \cos 2\xi} = \frac{L_{u,ac}}{L_{u,dc}} \tag{3.7}$$

To determine the best dimensions of the slot to minimise the skin effect, the correction coefficients should be 1. The skin effect factor is then calculated and used to determine the slot opening for the various scenarios of slip. The depth of the slot is calculated by [4]

$$\delta_{skin} = \sqrt{\frac{2}{\omega \mu_0 \mu_r \sigma_{Al}}} \tag{3.8}$$

The depth of the slot δ_{skin} is also the dimension h_1.The dimensions calculated for the rotor slot to reduce the skin effect are tabled in Table 7.

Table 7: Dimension of rotor slot to reduce skin effect

Slot variable	Dimension (mm)
b_1	11
b_4	2
h_1	1
h_4	11

The designed rotor slot is depicted in Figure 3-9.

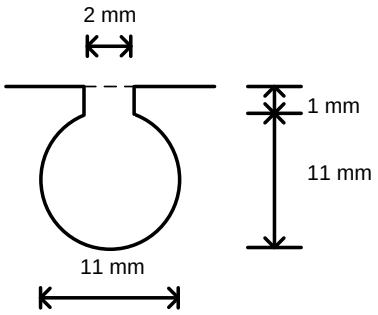

Figure 3-9: Designed rotor slot

3.3.2 Cogging torque reduction principles

In an induction machine, torque is established by the magnetic fields generated by the current in the coils. The torque is a function of the magnetic flux, which depends on the magnetic circuit's reluctance. As discussed in Section 3.3.1, the reluctance of the circuit (the slots) varies as the rotor position varies. The changing reluctance initiates a change in the torque and this causes a ripple in the torque.

A permanent magnet machine experiences the same effect, but this effect also occurs when the machine is de-energised because of the field generated by the permanent magnets.

There are various techniques employed to reduce cogging torque such as [12]:

- Skewing the stator or rotor stacks
- Creating fractional slots per pole
- Optimising the width of the magnet's pole

3.3.2.1 Skewing the stator or rotor stacks

The rotor slots are skewed relative to the stator slots in small motors to reduce permeance harmonics and cogging torque [4]. The skewed bars, length l, are modelled as a series of short straight bars, length Δl, and the number of these bars is defined as z_l

$$z_l = \frac{l}{\Delta l} = \frac{\alpha}{\Delta \alpha}. \tag{3.9}$$

The span of the total skewed bar is represented by α, while the span of each short straight bar, also referred to as slot angle, is represented by $\Delta\alpha$. The skewing factor, k_{sqv}, is determined by [4]

$$k_{sqv} = \frac{\sin\left(\frac{v\alpha}{2}\right)}{\frac{v\alpha}{2}} = \frac{\sin\left(v\frac{skew}{\tau_p}\frac{\pi}{2}\right)}{v\frac{skew}{\tau_p}\frac{\pi}{2}} \tag{3.10}$$

The variable, *skew*, in this equation represents the skewing measured as the length of an arc which is derived by $\alpha = skew(\pi/\tau_p)$. The skewing factor, k_{sqv}, should be zero to eliminate slot harmonics. It is deduced from [4] that skewing the slots by one slot pitch is able to reduce the effect of slot harmonics. However, for permanent magnet motors this slot skewing is difficult to manufacture because it would require skewing the magnets [12][13]. The motor design is a retrofit LSPMSM, therefore skewing the stator stacks is eliminated from the reduction options. Skewing the stator stacks is only possible when designing a new stator.

3.3.2.2 Creating fractional slots per pole

The most feasible mitigation method is to create fractional slots per pole. The number of slots per pole per phase, q, is given by [4]

$$q = \frac{Q_r}{2pm}. \tag{3.11}$$

The number of slot per phase is defined by Q_r/m and the number of magnetic poles facing the air gap is defined by $2p$. When q has a fractional component then the motor is considered to have fractional slots. If q is fractional then it means that each magnet faces a fractional number of slots Q_r/m.

A fractional q reduces cogging torque because the magnets are not in the same places relative to the stator teeth. The cogging torque produced by each magnet to maximise the flux flowing from the rotor to the stator is out of phase because of the difference in stator teeth placement relative to the magnet [13]. This means that fractional slots assist in reducing the cogging torque.

The rotor slot number was chosen as 30 for this design. This yields a value of q =2.5, meaning that the rotor design already has a fractional slot per pole value and will reduce the amount of cogging torque present.

3.3.2.3 Optimising the width of the magnet's pole

The equivalent mmf Θ_{mag} generated by a permanent magnet is dependent on its thickness, h_{mag}, as follows

$$\Theta_{mag} = -H_c h_{mag}. \tag{3.12}$$

A thicker magnet can lead to a greater mmf and in turn lead to a greater flux, Φ_{mag}, as follows

$$\Phi_{mag} = \frac{\Theta_{mag}}{R_{m,tot}}. \tag{3.13}$$

$R_{m,tot}$ is the total reluctance of the magnetic circuit. A greater flux generated by the magnet can cause an increased rate of change in the air gap flux density. This happens because of the leakage flux that appears between magnet poles [14]. Cogging torque is a function of the air gap flux and the air gap reluctance so if the air gap flux changes, the cogging torque will also change. An increased rate of change in the air gap flux density will thus lead to an increased cogging torque. This also implies that making the magnet thinner can decrease this rate of change and the associated cogging torque.

The dimensions of the permanent magnets will be discussed later in Section 3.3.3.

3.3.3 Magnet dimensions

As discussed in Section 2.2.3, the magnets are sized for a specific application. One element of the application is the amount of flux needed in the air gap of the motor design. A good design estimates

the air gap flux density at 0.85 – 0.9T [4]. An air gap flux density of 0.85 T was selected for the initial design of the motor to consider the worst case scenario.

The equivalent magnetic circuit of the retrofit LSPMSM design is displayed in Figure 3-10.

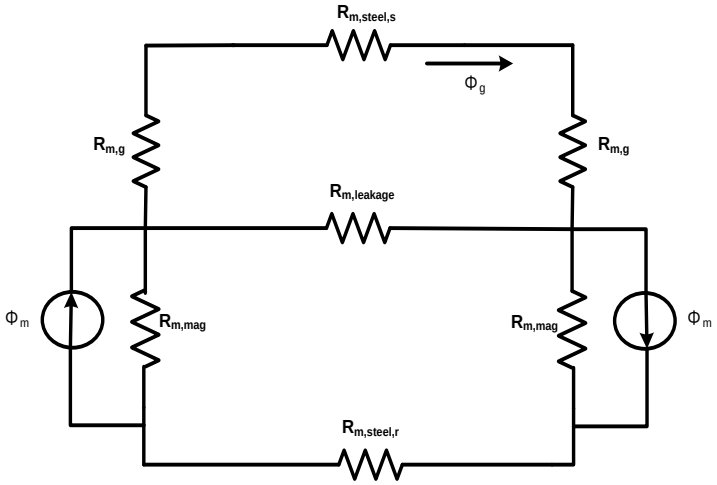

Figure 3-10: Equivalent magnetic circuit of the retrofit LSPMSM conceptual design

The leakage reluctance, $R_{m,leakage}$, will not be modelled in this design but strategies will be developed to reduce it in Section 5.1. The simplified magnetic circuit is given in Figure 3-11.

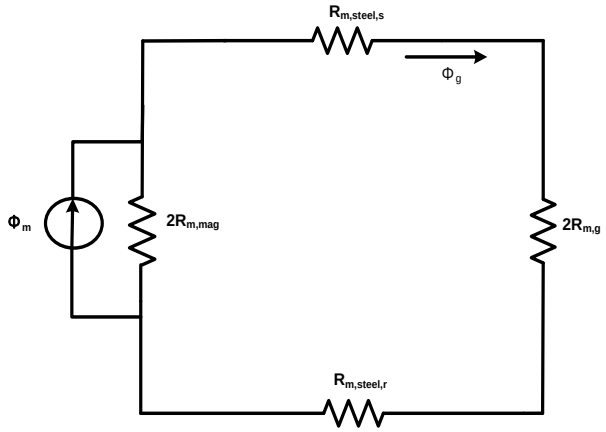

Figure 3-11: Simplified equivalent magnetic circuit of the retrofit LSPMSM conceptual design

The permeability of the core steel is assumed infinite compared to the permeability of the permanent magnet and the air gap. Deriving from this assumption, the permanent magnet's flux Φ_{mag} is equal to the air gap's flux Φ_g. This assumption neglects the effect of leakage flux and fringing and is a first order approximation. Kirchhoff's Current Law and equation 2.4 can then be applied as

$$A_{mag}B_{mag} = A_g B_g \text{ and} \tag{3.14}$$

$$B_g = \frac{A_{mag}}{A_g} B_{mag}. \tag{3.15}$$

A_{mag} represents the area of the magnetic material while A_g represents the area of the air gap. In order to size the magnet appropriately a material and grade must be chosen for the application. An NdFeB permanent magnet from Bakker Magnetics was selected with a manufacturer grade of 48H. As discussed in Section 2.2.1, NdFeB yields the highest magnetic properties of all the available magnets at room temperature. The selection was also based on the typical flux density the magnet is capable of producing at 60°C which is the temperature the motor is designed to reach during operation. The material's data is displayed in Table 8.

Table 8: NdFeB 48H

NdFeB 48H	
B_r	1.41 T
H_c	-1060 kA/m
μ_{mag}	0.001330189
BH_{max}	382 kJ/m^3

The operating point (B_{mag}, H_{mag}) of the permanent magnets must be calculated using the load line created by B_r and H_c. The load line is shown in Figure 3-12.

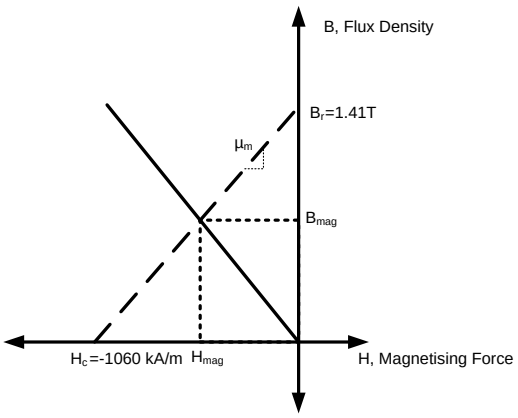

Figure 3-12: Load line of NdFeB 48

The operating point of the material, B_{mag} and H_{mag}, is taken as the midpoint of the B-H curve in the second quadrant as indicated in Figure 2-2. B_{mag} is taken as 0.705 T ($0.5B_r$) which makes H_{mag} = 541.844 kA/m. The product of these values of B_{mag} and H_{mag} yields the maximum energy product of 382 kJ/m^3. Using the maximum energy product yields the smallest volume of material needed to produce the desired air gap flux density [15].

Drawing from the simplified magnetic circuit, the magneto motive force drop across the air gap and the permanent magnet is equal, but opposite in polarity as shown in [15]:

$$\frac{H_{mag}h_{mag}}{H_g\delta} = -1. \tag{3.16}$$

Equation 3.25 can be solved for H_g and then for B_g as follows

$$H_g = -\frac{H_{mag}h_{mag}}{\delta}. \tag{3.17}$$

$$\frac{B_g}{\mu_0} = -\frac{H_{mag}h_{mag}}{\delta}. \tag{3.18}$$

If equation 3.27 is multiplied with equation 3.25, then the following equation is obtained

$$B_g^2 = \mu_0 \frac{h_{mag}}{\delta}\frac{A_{mag}}{A_g} H_{mag}B_{mag} \tag{3.19}$$

$$B_g^2 = \mu_0 \frac{Vol_{mag}}{Vol_g} H_{mag}B_{mag}. \tag{3.20}$$

The required volume of magnetic material per pole Vol_{mag} is calculated from equation 3.30 and using the maximum energy product of the material.

$$Vol_{mag} = \frac{Vol_g B_g^2}{\mu_0\left(H_{mag}B_{mag}\right)}. \tag{3.21}$$

The volume of the air gap, Vol_g, is calculated by subtracting the volume of the inner circle from the volume of the outer circle. In this application Vol_g is 32.876x10^{-6} m^3. The maximum volume of the magnetic material is then deduced as 50.960x10^{-6} m^3. The calculated volume provides a maximum BH equal to 345 kJ/m^3. The maximum BH of the permanent magnet material at 20°C is 382 kJ/m^3 and

is displayed in Table 8. At 60°C, the maximum BH drops to 348 kJ/m^3.The calculated volume is thus within the permanent magnet material's capability as per the supplier's datasheet [16].

A rectangular shape will be used with a depth of 170 mm because the axial length of the rotor is 170 mm. As discussed in Section 3.3.2.3, the magnet thickness must be kept to a minimum to minimise the effect of the cogging torque and still provide enough flux. As stated previously, the permeability of the core steel is assumed infinite. The permanent magnet's flux Φ_m is equal to the air gap's flux Φ_g and drawing from Kirchhoff's Current Law again, the following equation is obtained

$$\circ \oint Hdl = H_{mag} h_{mag} + H_g \delta = 0. \tag{3.22}$$

Equation 3.26 is then rewritten to obtain the thickness of the magnet, h_{mag}

$$h_{mag} = -\frac{(H_g \delta)}{H_{mag}}. \tag{3.23}$$

The field strength of the air gap, H_g, is determined from equation 2.1.

$$H_g = \frac{B_g}{\mu_r \mu_o}. \tag{3.24}$$

The air gap flux density was chosen as $B_g = 0.85$T and $\mu_0\mu_r = 4\pi x10^{-7}$ which is the permeability of air. Substituting equation 3.34 into 3.33 gives

$$h_{mag} = -\frac{\frac{B_g}{\mu_r \mu_0}\ \delta}{H_{mag}}. \tag{3.25}$$

The thickness of the magnet, h_{mag}, is then calculated as 6.242 mm. Now the required area is known as well as the thickness of the permanent magnet. The required length of the permanent magnet is then 58 mm. The calculated magnet thickness is very fine in terms of tolerances and this could make machining the magnets very costly. A thickness of 6.5 mm was chosen which results in a required length of 56 mm.

Figure 3-13 displays the BH curve for the material at 20°C and 60°C respectively. The point where the graphs intersect is the operating point of the material for that specific temperature. It is important

to note the shift in the operating point when the material reaches 60°C: (0.720 T;-530 kA/m) at 20°C versus (0.709 T; -490 kA/m) at 60°C.

Figure 3-14 represents the equivalent BH of the material and the maximum calculated energy product of the material. This assists in determining if the calculated volume produces a sufficient energy product. If the energy product is too far right of the maximum BH, the material will not be able to produce the desired flux during operation. If the energy product is left of the maximum BH required, it results in unused magnetic material because the material has already reached its limit. The graph indicates that the calculated volume of magnetic material is will sufficiently meet the requirements of the machine at the operating temperature of 60°C.

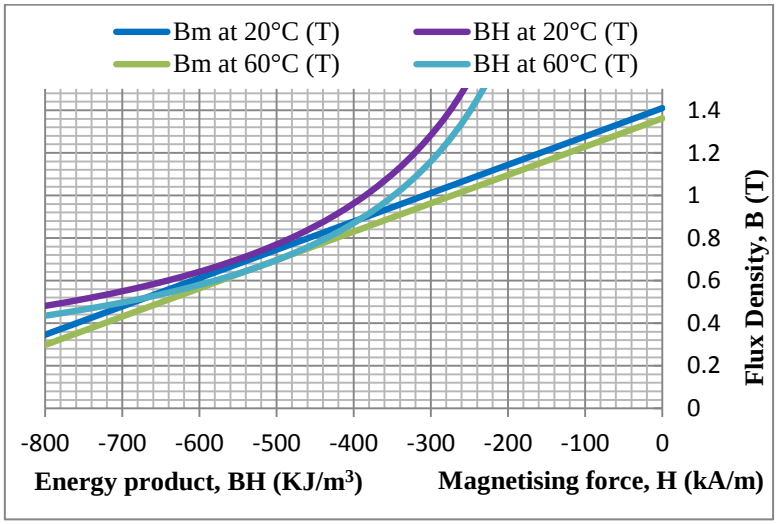

Figure 3-13: Comparison of B-H curve of NdFeB 48 at 20°C and 60°C

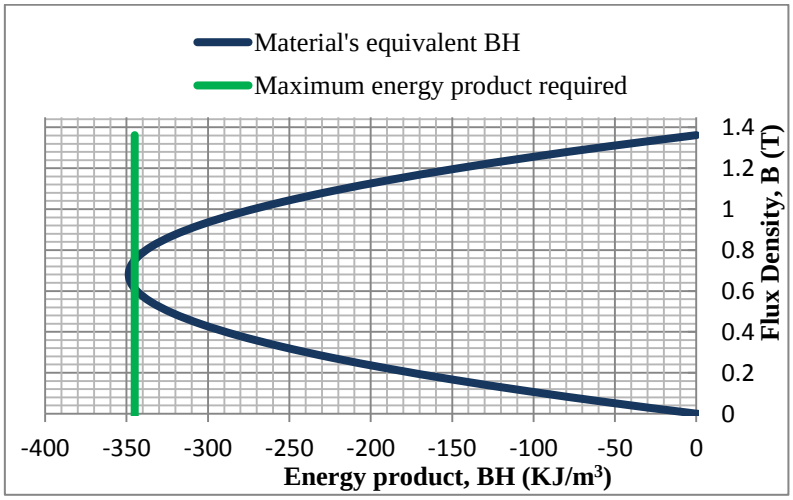

Figure 3-14: Energy product of NdFeB 48 at 60°C

The permanent magnets have been sized according to the application and corresponding magnetic circuit. The load line of the circuit is displayed in Figure 3-15 to indicate that the permanent magnets will operate within the designed operating point. The load line is developed from equation 3.25 by making B_{mag} the subject of the equation. The intersection of the load line of the magnetic circuit and the load line of the permanent magnet occurs at (0.789 T; -450 kA/m).

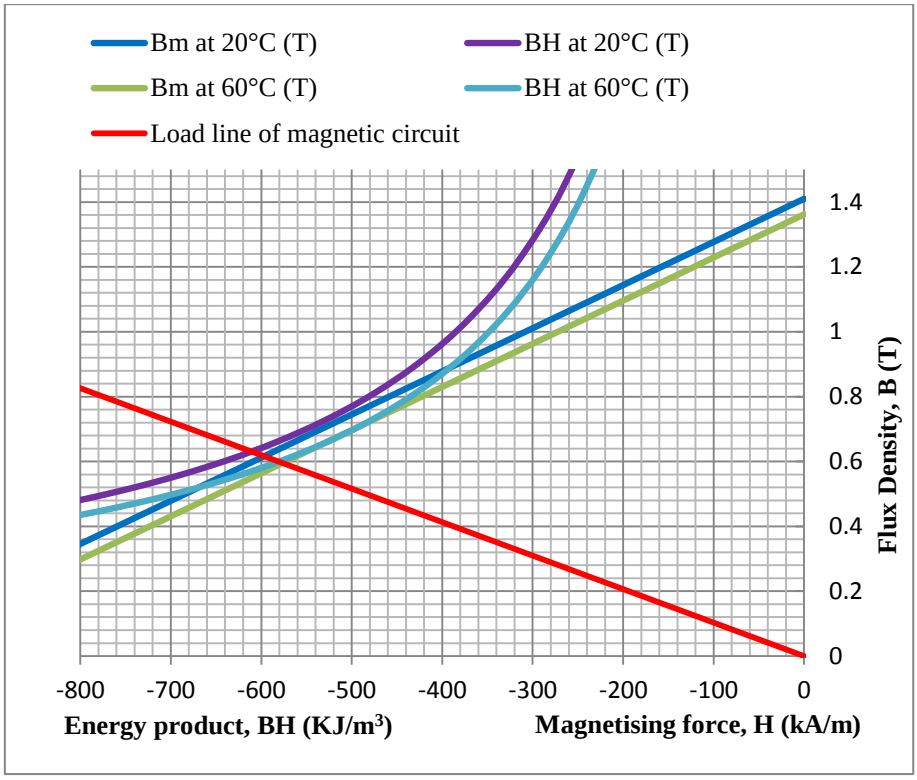

Figure 3-15: Load line of magnetic circuit intersecting with load line of the permanent magnet

3.3.4 End ring dimensions

The bars of the rotor need to be short-circuited to complete the electrical circuit so that current will flow. The size of the end ring must be determined so that it will sufficiently handle the resulting current. The current flowing in the end ring, I_{end_ring}, is determined from the current flowing in the rotor bars as follows [4]

$$I_{end\_ring} = \frac{I_r}{2\sin\frac{\pi p}{Q_r}}. \tag{3.26}$$

The current must be referred to the stator reference frame by applying K_{rs} which is determined as

$$K_{rs} = \frac{2m_s k_{ws1} N_s}{Q_r k_{sqr1}}. \tag{3.27}$$

The fundamental winding factor for the stator k_{ws1} is a product of the pitch factor k_{p1}, distribution factor k_{d1} and skewing factor k_{sq1}.

$$k_{ws1} = k_{p1} k_{d1} k_{sq1}. \tag{3.28}$$

In a full pitch winding, $k_{p1} = 1$ [4]. There is also no skewing present in the retrofit design as discussed in Section 3.3, thus $k_{sq1} = 1$. The distribution factor is defined as

$$k_{d1} = \frac{2\sin\frac{\pi}{2m}}{\frac{Q_s}{mp}\sin\frac{\pi p}{Q_s}} = 0.95766. \tag{3.29}$$

The fundamental winding factor is thus $k_{ws1} = 0.95766$ and $K_{rs} = 6.320$. The end ring current, I'_{end_ring}, becomes 834.298 A in the stator reference frame. The end ring area, A_{end_ring}, is calculated by

$$A_{end\_ring} = \frac{I'_{end\_ring}}{J_{end\_ring}}. \tag{3.30}$$

The current density, J_{end_ring}, is selected as 6.5 A/mm^2 to provide a lower end ring area of 128.353 mm^2. The dimensions of the end ring are selected as 13 mm wide and 10 mm high and are displayed in Figure 3-16.

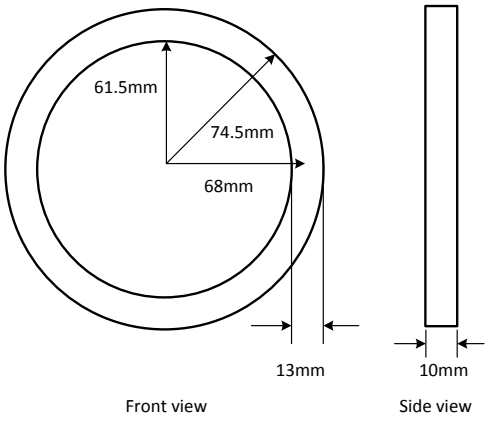

Figure 3-16: End ring dimensions

3.4 LSPMSM Structure

The conceptual design of the retrofit motor modelled in FEMM is depicted in Figure 3-17. The arrows in the rectangular magnets indicated the direction of magnetisation. It is important to ensure that the magnetic field generated by one magnet is not opposed by the other otherwise the required flux will not be generated.

The areas on either side of each magnet are air gaps that act as flux barriers. This is to minimise leakage flux around the end points of the magnets because an embedded magnet design can typically waste 25% of the magnet's flux capability [4]. The flux density plot will be analysed in Section 4.1.

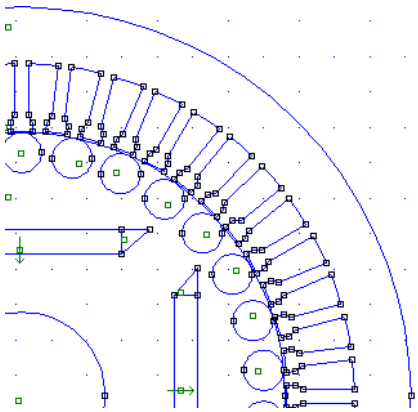

Figure 3-17: LSPMSM retrofit conceptual design FEMM model

3.5 Conclusion

This chapter covered the conceptual design of the retrofit motor. The rotor design is divided into two sections:

1. The rotor slots which form the induction machine cage winding to provide line-starting
2. The permanent magnet sizing which form the PMSM

The rotors slots were designed by using standard induction machine equations and taking skin effect into consideration. The torque curve will be calculated in Section 4.2 to determine if the cage was adequately designed to ensure a starting torque that would overcome the machine's inertia.

The permanent magnets were sized by selecting a material capable of producing the required flux density at the motor's operating temperature and then choosing an operating point to yield the maximum energy product. The equivalent magnetic circuit and the operating point of the permanent

magnet were used to calculate the dimensions of the permanent magnet. The performance prediction of the conceptual design will be discussed in Chapter 4.

Chapter 4 - Modelling

This chapter focuses on the modelling of the conceptual design to determine its theoretical performance. The model is analysed mathematically to determine the torque capability, predicted efficiency and the equivalent electric circuit parameters.

4.1 Flux density plot

As mentioned in Section 3.4, the prototype is modelled in FEMM. The outside boundary of the stator is set to zero to maintain the magnetic flux inside the machine. Non-magnetic steel is selected for the shaft so that no flux is diverted away from the air gap [4]. The following materials are used to define the prototype in FEMM:

- Stator and rotor steel: Steel M400-50A
- Stator slots: Copper
- Rotor slots: Aluminium
- Permanent magnets: NdFeB 48H (this is created by inputting B_r and H_c)
- Shaft: Stainless steel 1020

The flux density plot of the conceptual design is displayed in Figure 4-1. The results indicate that there is still significant leakage flux between the magnets and into the rotor core. The leakage flux amounts to 28% of the total flux created by the permanent magnet.

The leakage flux has prohibited the design from achieving the desired flux in the air gap. In this design, the average air gap flux density is approximately 0.7T. The maximum available power from the motor is proportional to the air gap flux density [4]. A lower flux leads to a smaller magnetic force and thus lowers the output torque. The motor will be able to operate but it will run inefficiently because it will lower the maximum power the motor will be able to deliver.

It is also important to note that the area of the air gap between the two opposing magnets yields little flux (0.7T) because of the span of the magnets. These areas act as end windings in this arrangement.

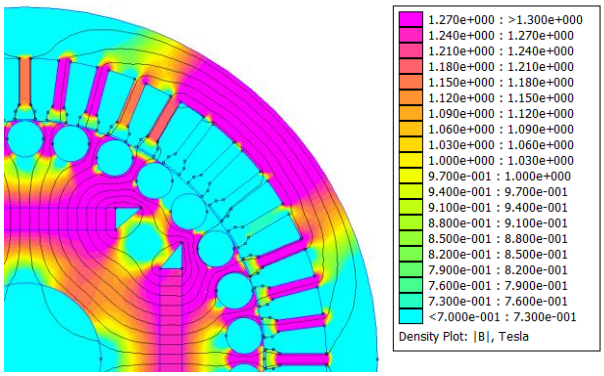

Figure 4-1: Close-up of quarter section of flux density plot

4.2 Preliminary torque capability

The torque generated by the motor T_{em} is calculated by [4]

$$T_{em} = \frac{m_s V_{sph}^2 \left(R_r^{'} / s\right)}{\left(\omega_s / p\right)\left(\left(R_s + \left(R_r^{'} / s\right)\right)^2 + \left(\omega_s L_k\right)^2\right)}. \tag{4.1}$$

$R_r^{'}$ is the total rotor resistance referred to the stator and is discussed in Section 4.4. The only other unknown in the above equation is L_k which is the motor short-circuit inductance. The short-circuit inductance is calculated by adding the stator leakage inductance $L_{s\sigma}$ and rotor leakage inductance $L_{r\sigma}$. The leakage inductance in turn consists of the following components [4]:

- Air gap leakage inductance L_δ
- Slot leakage inductance L_u
- Tooth tip leakage inductance L_d
- End winding leakage inductance L_w
- Skew leakage inductance L_{sq}

4.2.1 Air gap leakage inductance

The air gap leakage inductance L_δ is calculated by multiplying the magnetising inductance L_m with a leakage factor σ_δ. The magnetising inductance is defined as [4]

$$L_m = \frac{2m\tau_p \mu_0 l^{'} \left(k_{ws1} N_s\right)^2}{\pi^2 p \delta_{ef}}. \tag{4.2}$$

The fundamental winding factor, k_{ws1}, was determined in Section 3.3.4 as 0.9576. The pole pitch τ_p and effective air gap δ_{ef} are not known yet and must be derived. The pole pitch τ_p is calculated by

$$\tau_p = \frac{\pi D_s}{2p} = 0.17279. \tag{4.3}$$

The effective air gap δ_{ef} refers to the air gap lengthened by the Carter factor k_C which is a function of the slot pitch τ_u, the slot opening b_1 and the factor for reduction of slot opening κ [4].

$$k_C = \frac{\tau_u}{\tau_u - \kappa b_1} \tag{4.4}$$

$$\kappa = \frac{\frac{b_1}{\delta}}{5 + \frac{b_1}{\delta}}. \tag{4.5}$$

The slot opening b_1 is 3.7mm for the stator of the retrofit design. The Carter factor is thus k_C = 1.247 and the effective air gap δ_{ef} = 0.645 mm. From equation 3.34, the magnetising inductance is L_m = 788.50 mH. The stator leakage factor σ_δ is found from [4] and is 0.098. The air gap leakage inductance for the stator is then L_δ = 7.272 mH.

The air gap leakage inductance for the rotor is determined by a rotor leakage factor $\sigma_{\delta r}$. This factor is determined by [4]

$$\sigma_{\delta r} = \frac{\pi^2}{3}\left(\frac{p}{Q_r}\right)^2. \tag{4.6}$$

The air gap leakage inductance, $L_{\delta r}$, for the rotor is then calculated as 11.5 mH.

4.2.2 Slot leakage inductance

The slot leakage inductance L_u and permeance factor, λ_u, is calculated by [4]

$$L_u = \frac{4m}{Q}\mu_0 l' N^2 \lambda_u, \tag{4.7}$$

$$\lambda_u = \frac{h_4}{3b_4} + \frac{h_3}{b_4} + \frac{h_1}{b_1} + \frac{h_2}{b_4 - b_1} ln\left(\frac{b_4}{b_1}\right). \tag{4.8}$$

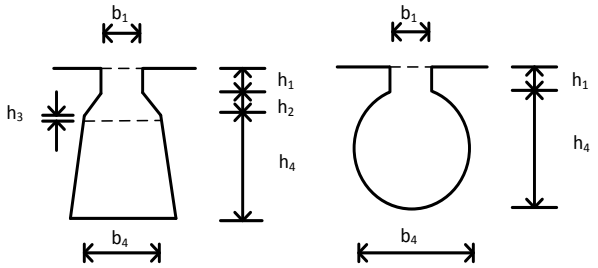

Figure 4-2: The slot types applicable to the retrofit design

The slot leakage needs to be calculated for the stator as well as for the rotor. The values of h_1, h_2, h_3, h_4, b_1 and b_4 refer to the dimensions of the stator or rotor slot as indicated in Figure 4-2. The stator slot leakage inductance is calculated as 123.139 µH while the rotor slot leakage inductance is 31.012 µH.

4.2.3 Tooth tip leakage inductance

The tooth tip leakage inductance is determined by the leakage flux flowing in the air gap outside the motor's slots. The tooth tip leakage inductance is calculated the same way as the slot leakage inductance, with only the permeance factor being determined by

$$\lambda_d = k_2 \frac{5\frac{\delta}{b_1}}{5 + 4\frac{\delta}{b}}. \tag{4.9}$$

The factor k_2 is 1 for this design because the winding is not short-pitched [4]. The tooth tip leakage inductance is thus 46.86 µH for the stator and 33.324 µH for the rotor.

4.2.4 End winding leakage inductance

The current flowing in the end windings generates a leakage flux. This leakage flux is greatly influenced by the axial length l_{ew} of the end winding and the coil span W_{ew} which are depicted in Figure 4-3 [4].

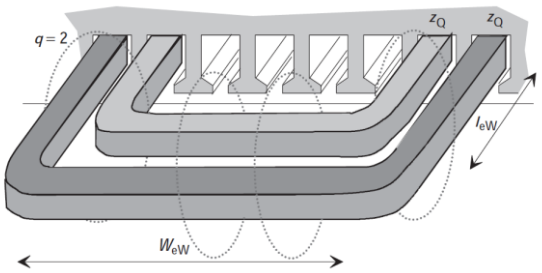

Figure 4-3: The dimensioning of an end winding [4]

The end winding leakage inductance is represented by

$$L_w = \frac{4mq}{Q} N^2 \mu_0 l_w \lambda_w, \tag{4.10}$$

$$l_w \lambda_w = 2 l_{ew} \lambda_{lew} + W_{ew} \lambda_W \tag{4.11}$$

The permeance factors λl_{ew} and λ_W are determined from [4] and thus are 0.34 and 0.24 respectively for a three phase, three plane stator winding with a cage winding. The coil span of the winding is equal to the pole pitch because there is no short-pitching. The axial length of the end winding is determined by halving the difference of the axial length of the full winding and the coil span. The result is that the end winding leakage inductance is calculated as L_w = 49.102 µH.

The retrofit LSPMSM uses a cage winding with a short-circuit ring that also produces a leakage inductance. The inductance is calculated by

$$L_{rw\sigma} = \mu_0 \frac{Q_r}{m_s p^2} \frac{1}{3} \left(l_{bar} \quad l_s^{'} \right) + v \frac{\pi D_r^{'}}{2p} \quad . \tag{4.12}$$

The terms l_{bar} and $D^{'}_r$ refer to the length of the rotor bar and the average diameter of the short-circuit ring respectively. The factor v = 0.18 when the amount of pole pairs is greater than 1 [4]. The average diameter of the short-circuit ring was measured as 74.5 mm, making $L_{rw\sigma}$ = 0.00989 µH.

4.2.5 Skew leakage inductance

Skewing is often employed in squirrel cage induction machines to mitigate the effects of cogging torque and permeance harmonics.

$$k_{sq1} = \frac{\sin \frac{s}{\tau_p} \frac{\pi}{2}}{\frac{s}{\tau_p} \frac{\pi}{2}} . \tag{4.13}$$

Skewing is not used in the retrofit design as discussed in Section 3.3. In this case, $s = \tau_p$ and the skewing factor for the fundamental becomes 1. The skew leakage factor is a function of the skewing factor and is represented by

$$\sigma_{sq} = 1 \quad k_{sq1}^2 . \tag{4.14}$$

The skew inductance is calculated by multiplying the magnetising inductance with the skew leakage factor. No skewing is employed and thus L_{sq} = 0 µH.

4.2.6 Total leakage inductance

The leakage inductances and impedances calculated in this section are displayed in Table 9.

Table 9: Stator and rotor leakage inductances and impedances for the retrofit LSPMSM

Stator leakage inductances		Rotor leakage inductances	
L_δ	7.272 mH		
L_u	123.1 µH	L_u	31.27 µH
L_d	46.86 µH	L_d	33.32 µH
L_w	49.10 µH	$L_{rw\sigma}$	9.890 nH
L_{sq}	0 µH	L_{rq}	0 µH
$L_{s\sigma}$	7.946 mH	$L_{r\sigma}$	64.55 µH

The total leakage inductance is $L_k = L_{s\sigma} + L'_{r\sigma}$ which means that the rotor leakage inductance needs to be referred to the stator. The rotor leakage inductance is usually referred to the stator as follows

$$L'_{r\sigma} = L_{r\sigma} \frac{4m_s}{Q_r}(N_s k_{ws})^2 \quad . \tag{4.15}$$

The winding factor is k_{ws} = 0.958 as per equation 3.42 and 3.43. The referral factor becomes 401.449, $L'_{r\sigma}$ = 27.861 mH and L_k = 33.728 mH.

4.2.7 Electromechanical torque curve

The electromechanical torque generated by the machine relative to the slip calculated by equation 4.1 is displayed in Figure 4-4. A supply voltage of 525 V delta connected was used for the calculations because of the supply and torque meter limitations which will be used for the validation.

The torque curve was simulated in ANSYS Maxwell®. The ANSYS Maxwell® model requires all the physical dimensions of the machine, such as stator and rotor diameter, slots, permanent magnet dimensions and number of stator turns. The limitation of the software is that it cannot process

fractional slots per pole as the design requires. The rotor slot number is rounded down to satisfy the constraint.

The torque curve can be determined from the FEMM model, but it requires rotating the model at various frequencies to simulate slip [17]. The calculated and simulated results are displayed together for comparison. The simulated results are slightly larger than the calculated values and the difference is attributed to the difference in rotor slots per pole. The lowest integer was used, which decreases the amount of rotor slots and hence decreases the rotor resistance.

The torque curve does not include the braking torque which permanent magnets are prone to generate. This is covered in Section 5.2 of this dissertation as part of the detail design.

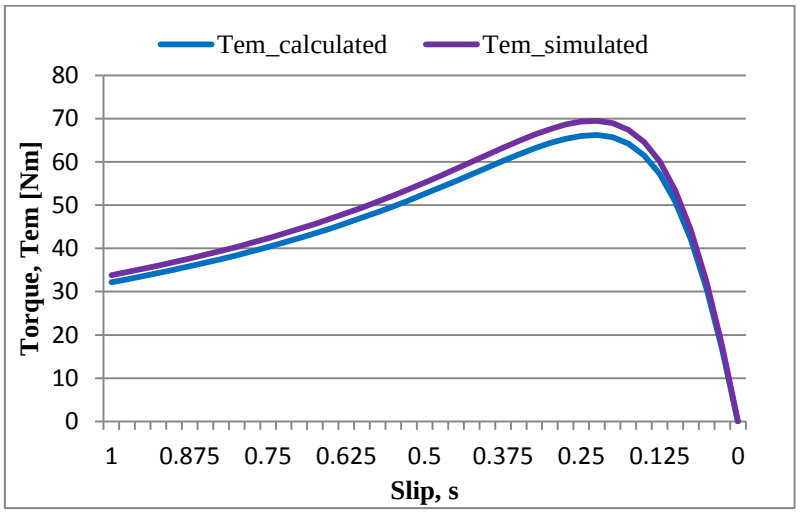

Figure 4-4: Electromechanical torque versus slip of the retrofit LSPMSM design

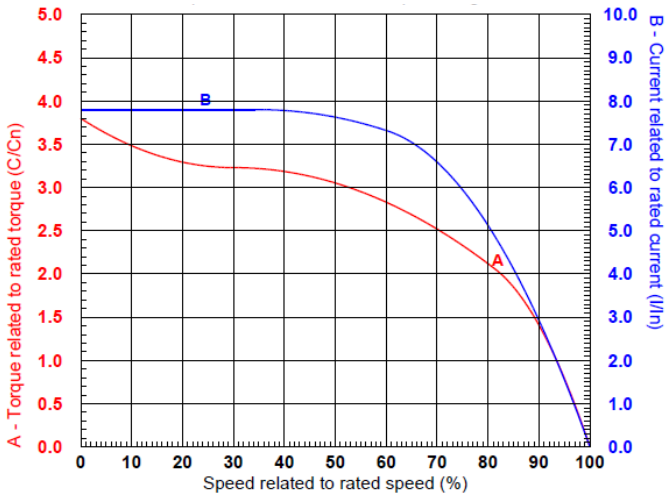

Figure 4-5: Electromechanical torque versus slip of the WEG WQuattro motor [16]

A torque summary of the retrofit LSPMSM design and the WEG WQuattro is given in Table 10. In order to compare the two torque curves, 525 V was used as the supply voltage in the prototype's calculations. The retrofit design has a much lower locked rotor torque. A high locked rotor torque is preferable for applications where the load is hard to start, such as cranes which have a high inertia. However, the lower locked rotor torque is acceptable for centrifugal fans and pumps, which is the intended usage, as these items have a very low starting load. The retrofit LSPMSM has a better breakdown torque, meaning that the machine can provide a higher torque without abruptly losing speed.

Table 10: Torque summary of the retrofit LSPMSM design and the WEG WQuattro

	Retrofit LSPMSM design	**WEG WQuattro**
Rated torque	47.8 Nm	47.8 Nm
Locked rotor torque	101.5 Nm	181.64 Nm
Maximum torque	198.69 Nm	155.35 Nm
Breakdown torque	180 Nm	95 Nm

4.3 Calculated efficiency

To determine the theoretical efficiency of the retrofit LSPMSM design, the total losses must be calculated. The following losses are applicable to the design:

- Resistive losses
- Iron losses
- Electromagnetic losses
- Mechanical losses

4.3.1 Resistive losses

Resistive losses are also sometimes called copper losses and occur in the conductors of a machine. The resistive losses P_{Cu} are calculated by [4]

$$P_{Cu} = mI^2 k_R \frac{Nl_{av}}{\sigma A_c} . \tag{4.16}$$

The skin effect resistance coefficient, k_R, was set in Section 3.3.1 as 1 to determine the slot dimensions. Table 11 indicates the conductor properties of the rotor slot. The $P_{Cu,r}$ is 7.36 W.

Table 11: The properties of the conductor used in the rotor

Properties of conductor	Value
Average length, l_{av}	0.17 m
Conductivity, σ_{Al}	35 x 10^6 S/m
Cross-sectional area, A_c	97.5 x 10^{-6} m^2

Similarly, the value of the resistive losses of the stator is then calculated using the properties in Table 12 as $P_{Cu,s}$ = 443 W.

Table 12: The properties of the conductor used in the stator

Properties of conductor	Value
Average length, l_{av}	0.17 m
Conductivity, σ_{Cu}	57 x 10^6 S/m
Cross-sectional area, A_c	0.445 x 10^{-6} m^2

4.3.2 Iron losses

The iron losses are calculated by dividing the magnetic circuit of the machine into sections where the flux density is constant. For this design, the machine is split into quarters to facilitate the analysis. The flux density plot from Section 4.1 is used for the analysis. The quarter section is divided into four sub-sections where the flux density is similar in the area. The sections are detailed in Table 13.

Table 13: Segregation of sections to determine iron losses

Sub-section	Average flux density in area
Sub-section 1	1.27 T
Sub-section 2	0.9 T
Sub-section 3	0.7 T
Sub-section 4	0.2 T

The iron losses for a sub-section are calculated by [4]

$$P_{Fe} = MP_{Bn} \left(\frac{B_n}{1.5} \right)^2 . \quad (4.17)$$

M refers to the mass of a sub-section and the factor P_{Bn} is the loss per mass unit specified by the manufacturer of the material at the specific flux density B_n. There are two types of lamination material available locally: M400-50A and M530-50A. The material is selected based on the saturation point and the loss per mass unit factor. Table 14 displays the difference between the two materials based on the selection criteria. Manufacturers usually give the losses of their materials per mass unit at a peak value of flux density of 1.5T.

Table 14: Lamination material specifications [19]

Material	Saturation Point (T)	Loss per mass unit at B_n = 1.5T (W/kg)
M400-50A	1.3T	6
M530-50A	1.4T	8

The highest flux density reached in the flux density plot is 1.27T. Although M530-50A would be a better solution with regards to the saturation point, it [19] has higher iron losses than M400-50A. M400-50A was selected to minimise the iron losses in the machine. The total mass of the iron of the machine is estimated as 30 kg.

The iron losses for each of the identified sub-sections are displayed in Table 15. The iron losses for the quarter sections summate to 16.213 W. The total iron losses for the LSPMSM are 64.853 W.

Table 15: Iron losses calculated for each section

Section	Mass of section	Iron losses
Section 1	2.5 kg	9.6 W
Section 2	1.5 kg	3.24 W
Section 3	2.5 kg	3.267 W
Section 4	1 kg	0.107 W

4.3.3 Stray losses

Stray losses are difficult to measure or calculate but have been estimated as 0.05 – 0.15% of the input power for a non-salient pole synchronous machine [20]. This puts the electromagnetic losses in the range of 3.75 – 11.25 W. The maximum result will be used when calculating the total losses.

4.3.4 Mechanical losses

Mechanical losses are a result of bearing friction and windage. These losses are calculated by the equations below [4]

$$P_{pw1} = \frac{1}{32} k C_M \pi \rho \Omega^3 D_r^4 l_r \tag{4.18}$$

$$P_{pw2} = \frac{1}{64} C_M \rho \Omega^3 \left(D_r^5 - D_{ri}^5\right). \tag{4.19}$$

Ω is the mechanical angular velocity, D_r is the diameter of the rotor and l_r is the axial length of the rotor. The roughness coefficient k is 1 for a smooth surface. C_M is a torque coefficient which is determined by measurements and is dependent on the density ρ and viscosity of the coolant used by the machine. The calculations are provided in Appendix B. The results are provided in Table 16.

Table 16: Calculated mechanical losses

Mechanical losses	Value
P_{pw1}	17.092 W
P_{pw2}	1.31 W
Total mechanical losses	18.402 W

4.3.5 Total losses and efficiency

The total losses P_{loss} of the LSPMSM design summate to 554 W. The efficiency η of the design is thus

$$\eta = \frac{P_{in} - P_{loss}}{P_{in}} = 0.926 \tag{4.20}$$

The calculated efficiency of the design is 92.6% in comparison to the 90.4% of the equivalent induction motor. A model of the design was constructed in ANSYS Maxwell® and simulated to verify the calculated efficiency. The simulated efficiency curve is displayed in Figure 4-6. The efficiency at a torque angle of 90° is 93%. The maximum efficiency is 95%. The efficiency must also be measured in a laboratory to validate the results. The validation is discussed in Chapter 6.

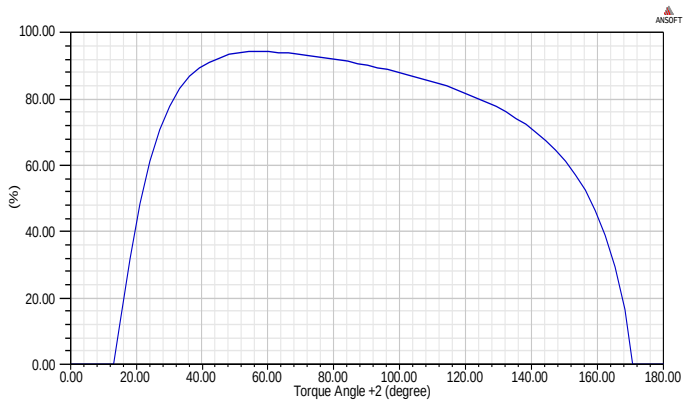

Figure 4-6: Simulated efficiency curve determined from ANSYS Mawxell© program

4.4 Equivalent electrical circuit

The retrofit LSPMSM design's equivalent electrical circuit consists of an induction machine equivalent to Figure 3-3 for start-up and a synchronous machine's equivalent circuit because of the steady-state operation. The values of R_1 and X_1 remain the same as the original circuit of the induction

motor. The rotor resistance, R_2, the rotor leakage reactance, X_2, the magnetising reactance, X_m, and the core resistance, R_{fe}, must be determined for the retrofit LSPMSM.

The rotor resistance consists of the resistance of the rotor bar, R_{rotor_bar}, and the resistance of the end ring, R_{end_ring}.

$$R_{rotor\_bar} = \rho_{Al} \frac{l'}{A_{ur}} \tag{4.21}$$

$$R_{end\_ring} = \rho_{Al} \frac{l_{end\_ring}}{A_{end\_ring}} \tag{4.22}$$

$$R_2 = R_{rotor\_bar} + \frac{R_{end\_ring}}{2\sin^2 \frac{2\pi p}{Q_r}}. \tag{4.23}$$

The second term of equation 3.64 represents the part of the end ring that a rotor bar is connected to [4]. The value of R_2 in the rotor reference frame is 74.318 μΩ and 2.122 Ω in the stator reference frame.

The rotor leakage reactance is determined from the rotor leakage inductance which was calculated in Section 4.2.6. The rotor leakage inductance is $L'_{r\sigma} = 27.861$ mH and thus the rotor leakage reactance in the stator reference frame is $X_2' = 8.01$ Ω.

Similarly, the magnetising reactance is determined from the magnetising inductance, L_m. The magnetising inductance was calculated in Section 4.2.1 as L_m = 788.5 mH. The magnetising impedance, X_m, is then 247.714 Ω.

The core resistance, R_{fe}, can be determined from the iron losses of the machine. The total iron losses were calculated as 64.853 W in Section 4.3.2. The per phase iron losses are thus 21.617 W. The voltage drop over the core resistance, V_m seen in Figure 4-7, is determined by subtracting the voltage drop over R_1 and X_1 from the applied voltage. If rated voltage is applied, rated current will flow through the stator windings. The value of V_m is determined as 261.527 V. The core resistance is thus calculated as 3163.911 Ω.

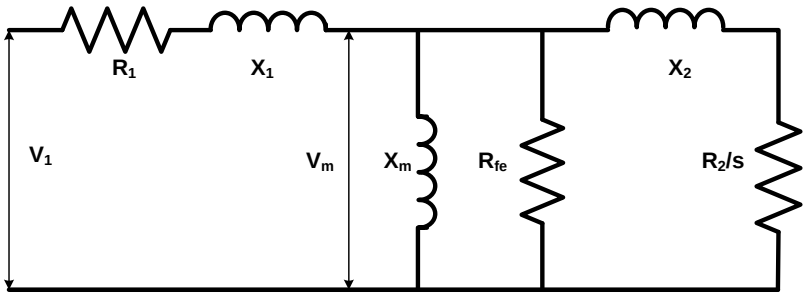

Figure 4-7: Equivalent circuit used to determine R_{fe}

Table 17 indicates the calculated equivalent circuit parameters for the LSPMSM and the results from ANSYS Maxwell®. The calculated results correlate well with the results from ANSYS Maxwell®. The rotor resistance and reactance is lower from the verification model because the software does not allow fractional slots per pole. A lower slot number was used which lowers the rotor resistance as seen in equation 3.64. The machine parameters are validated by means of the tests documented in Chapter 6.

Table 17: Calculated equivalent circuit parameters for the LSPMSM

Parameter	Calculated value	Result from ANSYS Maxwell
R_1	2.383 Ω	2.34 Ω
R_2	2.122 Ω	2.100 Ω
R_{fe}	3163.911 Ω	3089.07 Ω
X_1	5.748 Ω	5.76 Ω
X_2	8.01 Ω	7.851 Ω
X_m	247.714 Ω	257.158 Ω

The equivalent electrical circuit for the LSPMSM retrofit conceptual design is displayed in Figure 4-8. X_q and X_d represent the quadrature axis impedance and direct axis impedance respectively. The values of L_d and L_q will be calculated in Section 5.2.

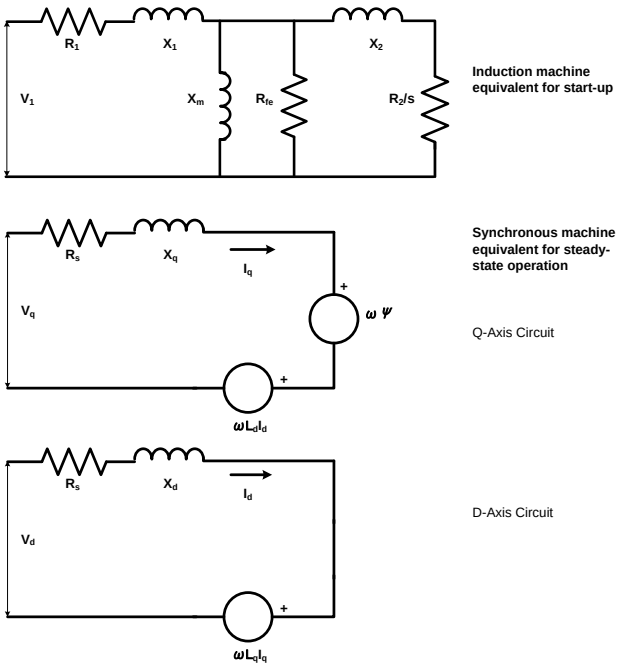

Figure 4-8: Equivalent circuit for the LSPMSM retrofit conceptual design

4.5 Conclusion

This section covered the modelling and the performance prediction of the retrofit motor. The average air gap flux density achieved is lower than the desired flux density: 0.7T in comparison with the desired 0.85T. The design will need to be improved in order to achieve the desired flux density in the air gap. There are two factors that will be considered for the improvement strategy:

1. The magnets can be moved closer to the air gap to prevent leakage flux through the rotor core and to create a shorter path for the magnetic field of the magnets to cross through to the air gap
2. The design of the flux barriers next to the magnets must be improved to reduce the leakage flux between magnets

This improvement strategy will be covered in Section 5.1 as the Leakage Flux Reduction section.

Chapter 5 - Detail Design

This chapter further develops the conceptual design to meet the project specifications. Techniques are applied to reduce the leakage flux to an acceptable level. The braking torque of the permanent magnets is analysed to determine if the retrofit design will meet the torque requirements. The overall flow diagram for this chapter is depicted in Figure A - 2 in Appendix A.

5.1 Leakage Flux Reduction

As discussed in Section 4.5, the average air gap flux density of the proposed design is lower than the desired flux density. This means that there is a fair amount of flux generated by the permanent magnets that is lost in the rotor. This is seen in Figure 4-1 between the ends of the permanent magnets. A lower flux density relates directly to a lower torque output of the motor and thus an inefficient design. To improve the average flux density, the leakage flux present in the design must be reduced.

5.1.1 Movement of magnets

The first step to reducing the leakage flux is to move the magnets closer to the air gap. The magnets were moved as close as possible to the rotor slots while still prohibiting the magnets from touching the slots so that the laminations would not be divided into sections. Manufacturing a rotor lamination that is split into sections is more difficult than a single lamination so structural integrity must be maintained.

Figure 5-1 presents the flux density plotted in FEMM with the magnets moved closer to the air gap. The average flux density achieved in the air gap now becomes 0.74T. Leakage flux is still present around the end points of the magnets and amounts to 26% of the total flux. The amount of leakage flux is determined by measuring the flux generated by the permanent magnet and subtracting the flux measured over one pole length of the air gap.

Moving the magnets even closer to the air gap could further increase the average air gap flux density by reducing the leakage flux, but it is not practical due to the proximity of the rotor slots and hence the structural integrity. The real issue could be the design of the flux barriers at the end points of the magnets.

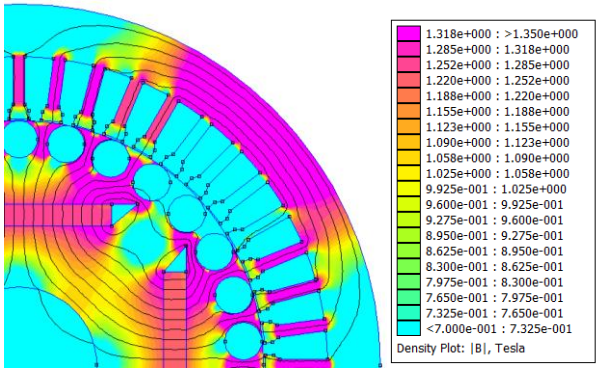

Figure 5-1: Close-up of quarter section of flux density plot with magnets moved closer to the air gap

5.1.2 Improvement of flux barriers

The second step is to improve the design of the flux barriers. The aim of the flux barriers is to channel the flux created by the magnets. If the flux can be channelled away from the perpendicular magnet and towards the air gap it will reduce the amount of leakage flux present. The flow diagram for the improvement of the flux barriers and reduction of the leakage flux is depicted in Figure 5-2. This is also an extract from the overall detail design flow diagram in Appendix A. According to [4] approximately 25% of the flux of a permanent magnet is lost if the magnet is embedded in the rotor structure. This is a significant amount of leakage flux, but can be reduced if the flux barriers are optimised. Surface-mounted permanent magnets lose 5-10% of their flux. The literature on embedded permanent magnets does not give guidance on the lowest leakage flux obtainable, but it was decided to aim to reduce the loss to 15%.

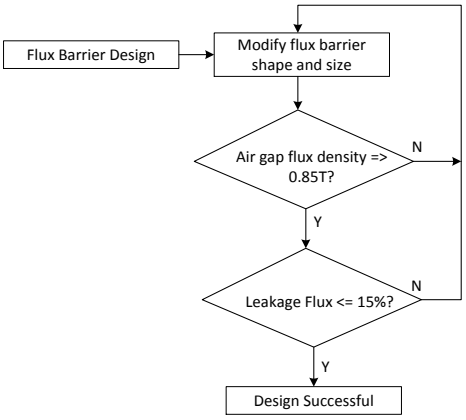

Figure 5-2: Flow diagram for the modification of flux barriers and reduction of leakage flux

The first attempt at changing the flux barriers is displayed in Figure 5-3. The aim is to force more of the flux away from the perpendicular magnet and towards the air gap. A round shape was selected to

lengthen the path the flux would need to take to get to the opposing magnet or to circulate around the end point. The average flux density in the air gap is approximately 0.78T in this case. Some leakage flux has been channelled away from the ends of the magnets, but it is not yet sufficient in achieving the desired air gap flux density. The leakage flux amounts to 24% of the total flux produced by the magnets.

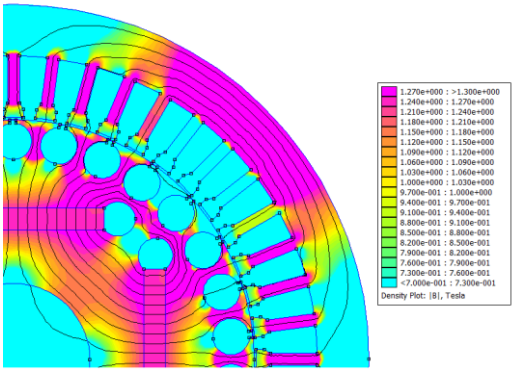

Figure 5-3: Close-up of quarter section of flux density plot with first modification of flux barriers

This second modification is a hybrid between the original and the first modification. The pointed edges towards the air gap and a rounded edge towards the perpendicular magnet channel the flux towards the air gap. The flux density plot of the second modification is depicted in Figure 5-4. The leakage flux amounts to 19% of the total flux. The average flux density in the air gap is 0.8T which just falls out of the value selected for the LSPMSM design. However, the success criterion for this area of the design is to achieve an air gap flux density of 0.85T.

The second attempt yields a good design in reducing leakage flux and improving the air gap flux density. However, it seems as though the leakage flux can be reduced further when analysing the flux lines between the perpendicular magnets in Figure 5-4.

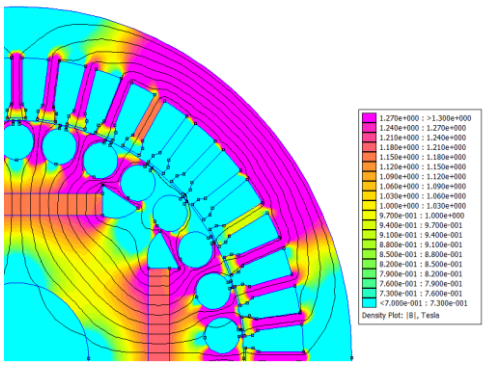

Figure 5-4: Close-up of quarter section of flux density plot with second modification of flux barriers

5.1.3 Leakage flux reduction final design

The design was improved by adding separate flux barriers between the end points of the magnets' flux barriers as displayed in the flux density plot shown in Figure 5-5. The average air gap flux density of the design is 0.88T and the leakage flux has been reduced to 15%.

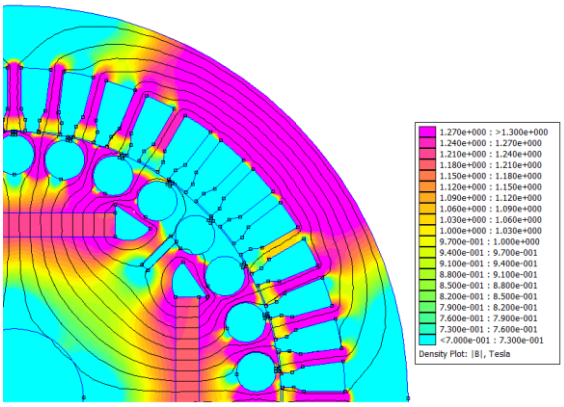

Figure 5-5: Flux density plot after leakage flux reduction

5.2 Permanent Magnet Braking Torque Analysis

Permanent magnets are sized such that the magnetic flux generated is high enough to ensure a good synchronous torque, but low enough to ensure good starting [20]. This is because permanent magnets generate a braking torque which affects the line start of a LSPMSM. The relationship between different volumes of magnetic material and the corresponding acceleration torque curve is displayed in Figure 5-6. It is evident that a comparatively larger magnetic volume results in a poor acceleration torque curve.

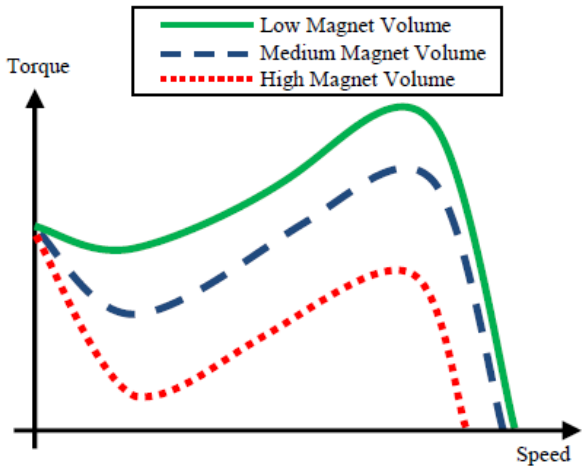

Figure 5-6: Relationship between volume of magnetic material and acceleration torque [20]

To determine the effect of the specific volume of magnetic material used in the retrofit design, the braking torque of the material must be calculated. The braking torque, T_b, is calculated by [20]

$$T_b = \frac{3p}{2w_s} E_m^2 R_1 (1 \quad s) \frac{R_1^2 + (1 \quad s)^2 X_{qs}^2}{\left(R_1^2 + (1 \quad s)^2 X_{ds} X_{qs}\right)^2}. \tag{5.1}$$

X_{qs} and X_{ds} represent the quadrature axis impedance and direct axis impedance respectively. The voltage, E_m, is the back-emf generated by the permanent magnets. The magnetic flux of the permanent magnets crosses the air gap and induces a voltage in the stator. Hence, the back-emf is dependent on the flux linkage created by the permanent magnets. Flux linkage, ψ, is determined by the winding factor, k_w, the number of turns in series of the stator, N_s, and the flux, Φ, and is written as

$$\psi = k_w N_s \Phi. \tag{5.2}$$

The flux linkage was determined by creating a model of the design in FEMM. The rotor currents are set to zero to simulate the motor at synchronous speed. The rotor was rotated to plot the flux linkage in all three phases over the rotation. The flux linkage obtained from the rotation is displayed in Figure 5-7.

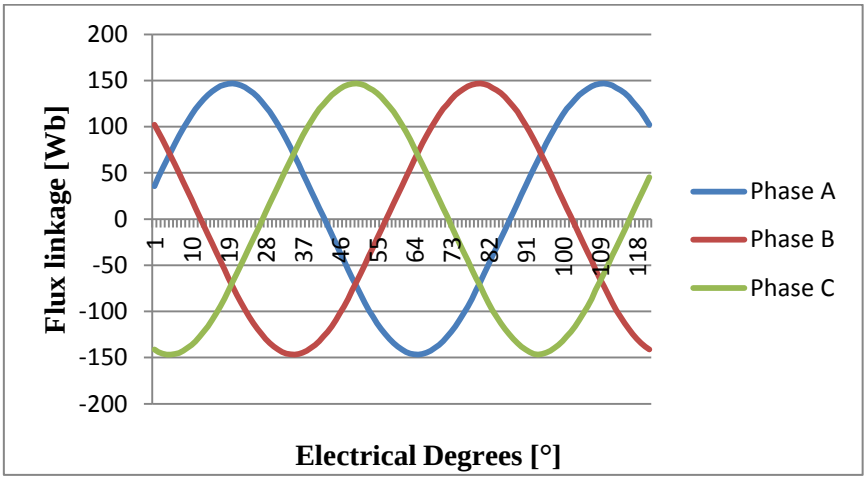

Figure 5-7: Flux linkage of LSPMSM FEMM model

The maximum back-emf, E_m, is determined by

$$E_m = N_m \psi_{max}. \tag{5.3}$$

Figure 5-8 indicates the calculated back-emf per phase of the LSPMSM. The maximum RMS value of the line-to-line voltage of the back-emf is $E_m = 415.35$ V. ANSYS Maxwell® displays the

back emf of the model as the induced winding voltages at no load, which is displayed in Figure 5-9. The simulated RMS value of the no load line-to-line voltage is 420.21 V. There is some ripple present in the simulated back-emf curve which can be attributed to the software's limitations regarding fractional slots per pole. In comparison, the back-emf curve calculated from the FEMM model, which contained fractional slots per pole, is smooth.

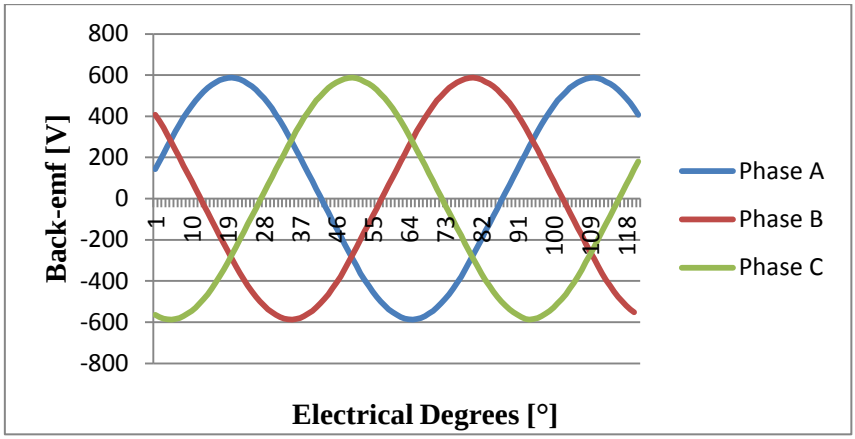

Figure 5-8: Back-emf of LSPMSM FEMM model

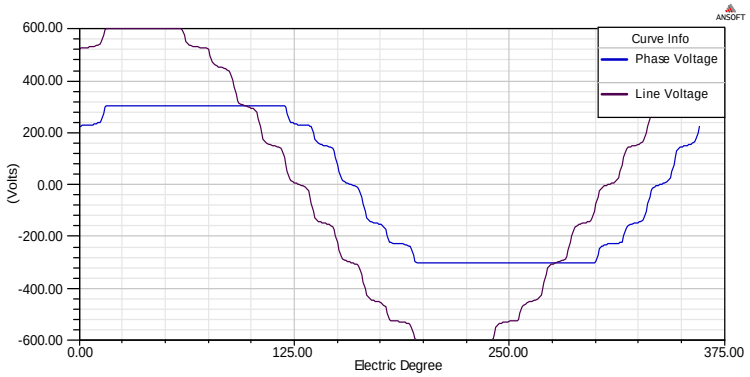

Figure 5-9: Simulated back-emf voltages at no load

The quadrature axis impedance and direct axis impedance are solely consisting of the inductances, L_q and L_d, and they play an important role in the steady-state and the dynamic performance of a LSPMSM [4] [21]. The inductances are calculated as follows

$$L_q = L_{mq} + L_{s\sigma}, \tag{5.4}$$

$$L_d = L_{md} + L_{s\sigma}. \tag{5.5}$$

$L_{s\sigma}$ is the leakage inductance of the stator which has been calculated in Section 4.2. L_{md} and L_{mq} are the magnetising inductances in the respective axes and are determined as follows

$$L_{md} = \mu_0 \frac{2m\tau_p}{p\pi^2 \delta_{def}} l' \left(k_{ws1} N_s\right)^2, \tag{5.6}$$

$$L_{mq} = \mu_0 \frac{2m\tau_p}{p\pi^2 \delta_{qef}} l' \left(k_{ws1} N_s\right)^2. \tag{5.7}$$

The only difference between the two equations is the effective equivalent air gap in the direct axis δ_{def} and the effective equivalent air gap in the quadrature axis δ_{qef}. In a non-salient pole machine, $\delta_{def} = \delta_{qef}$ which is calculated by [4]

$$\delta_{def} = \frac{4}{\pi} k_C \delta_{ef}. \tag{5.8}$$

The effective air gap δ_{ef} and Carter factor k_C have already been determined in Section 4.2. The value of δ_{def} and δ_{qef} is thus 1.060. The magnetising inductances become $L_{md} = L_{mq} = 0.5043$ H. The calculated and simulated results of the braking torque are displayed in Figure 5-10 which show good correlation.

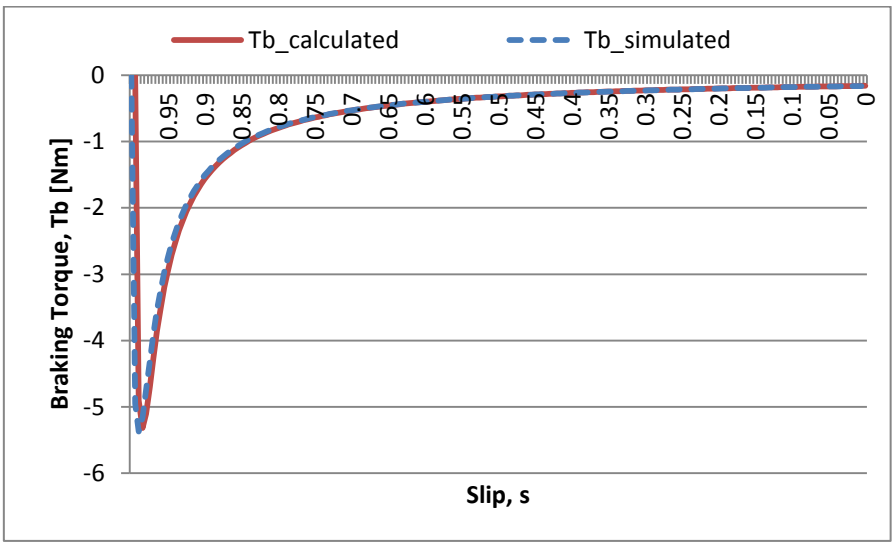

Figure 5-10: Braking torque generated by the permanent magnets

During starting, the braking torque reaches its maximum effect. Based on the calculations, the effect on the total torque for this design will be minimal. It will still be added to the electromagnetic torque curve, which was produced in Section 4.2.7, to determine the resultant starting torque.

5.3 Total torque capability

The resultant torque curve including the braking torque is displayed in Figure 5-11. The braking torque causes a slight dip after starting but is negligible in comparison to the electromechanical torque and this is why the total torque curve and electromechanical torque curve mostly overlap. The starting torque is 28 Nm and the breakdown point is reached at a slip of 0.15 when the torque is 61 Nm. This is the point at which the motor will desynchronise with its load and slow down to a standstill. If the load is speed-dependent, the machine may slow down enough to operate as an induction machine and remain at a non-synchronous speed.

Figure 5-12 displays the comparison between the calculated torque curve and the simulated torque curve. The simulated torque curve is slightly larger, approximately 5%, because of the difference in rotor resistance discussed in Section 4.4. This resultant torque curve will be validated against the test results in Section 6.7.

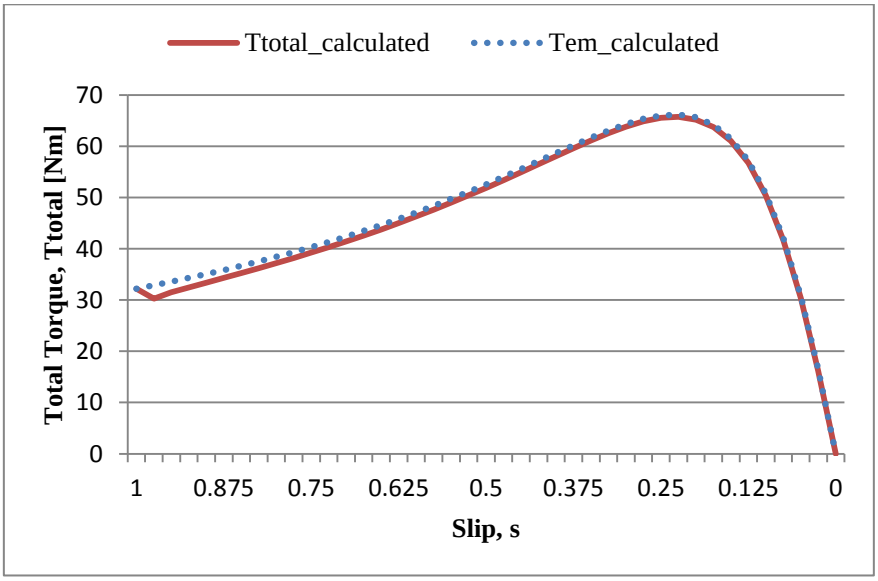

Figure 5-11: Total torque curve for retrofit LSPMSM design

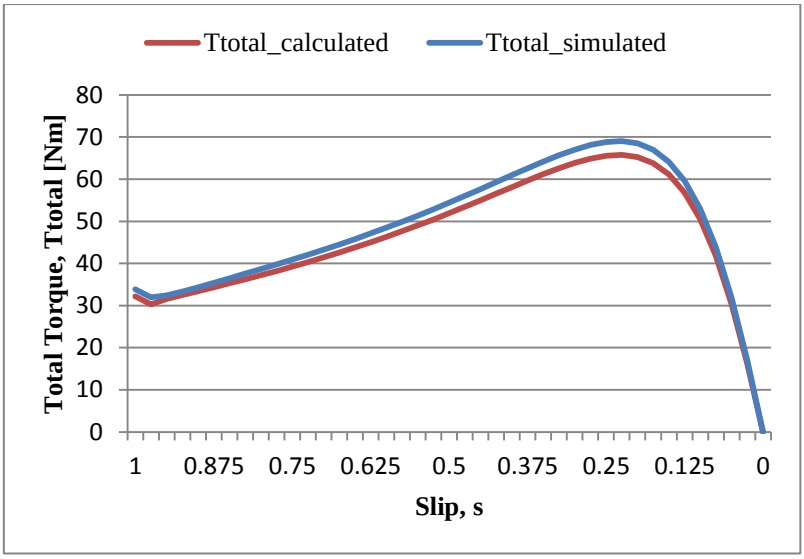

Figure 5-12: Comparison between calculated and simulated torque curves

5.4 Manufacturing and Assembly

5.4.1 Rotor laminations

The rotor is constructed from laminations stacked together to form the full axial length. Each lamination is 0.5 mm thick and thus 340 laminations are required to produce the axial length of 170 mm. The lamination is depicted in Figure 5-13. Two keys have been allowed for in the shaft to ensure a secure fit between the shaft and the laminations. The stack of laminations is compressed tightly and the end rings are pressed on both ends of the stack. The laminations are manufactured 10 mm larger in diameter than required. Once the rotors bars have been manufactured, the stack will be machined to the required diameter to ensure that it forms a smooth cylinder and a consistent air gap when the final machine is assembled. Figure 5-14 illustrates the rotor before the stack is machined.

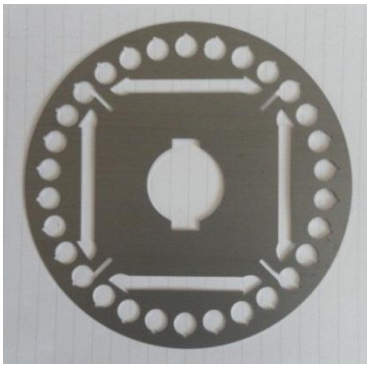

Figure 5-13: Rotor lamination

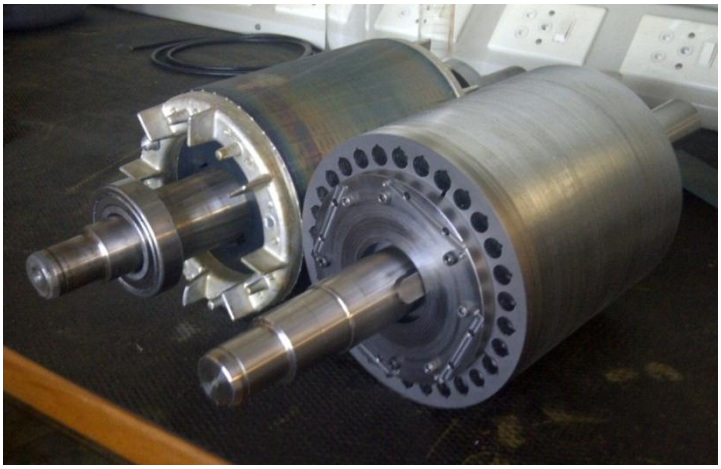

Figure 5-14: Rotor stack with shaft

5.4.2 Rotor bars

The rotor bars are manufactured by machining solid rectangular bars down to the required shape to form the circular bar with a key formed by the slot opening and slot depth requirements. These bars are then inserted into the rotor stack to form the rotor cage.

5.4.3 Final assembly

The manufactured rotor is placed inside the stator to form the retrofit LSPMSM. The permanent magnets are only placed in the rotor after the initial tests are done. Figure 5-15 displays the final assembly and the test setup.

Figure 5-15: Final assembly and test setup

5.5 Conclusion

This section covered the detail design of the retrofit motor. Modifications were applied to the conceptual design to reduce the leakage flux to an acceptable level. The total torque capability of the design was analysed to determine the effects of the braking torque of the permanent magnets. It is important to note that the effect of the braking torque is greatest during the starting of the machine. Although the LSPMSM design is affected by the permanent magnet braking torque, the reduction is not enough to prevent the machine from starting.

The next step is to test the operation of the machine in a laboratory to determine if it meets the intended design criteria. The testing and validation is covered in Chapter 6.

Chapter 6 - Testing and Validation

This chapter describes the tests required to determine the functionality of the retrofit LSPMSM design. The testing is conducted in a laboratory to validate the performance of the prototype.

6.1 Testing Methodology

The retrofit LSPMSM is tested in order to conclude if the proposed machine can be used as a replacement for an equivalent induction machine. The 7.5 kW induction machine is tested first to establish a set of practical base parameters that can be used for the comparison. Once testing of the induction machine is complete, the rotor of the induction machine is replaced with the design rotor. This helps establish the effectiveness of the design process that was followed to develop the prototype.

The designed rotor is tested with and without the permanent magnets. The two instances are tested because the losses due to friction and windage are measured when the machine has no excitation. It is not possible to obtain zero excitation in a permanent magnet machine and hence the machine is tested without the permanent magnets [25].

The same tests are conducted on the induction machine and the LSPMSM. The tests are:

1. DC resistance test of the stator windings
2. Blocked rotor test
3. No load test
4. Back-emf (only for the LSPMSM)
5. Cogging torque test (only for the LSPMSM)
6. Efficiency analysis
7. Torque analysis

These tests facilitate the determination of the equivalent circuit parameters, the power factor, total leakage reactance and starting torque and serve as the validation strategy for the prototype. The stator parameters are tested to check the validity of the theory that they will remain the same because the stator is unchanged. The other equivalent circuit parameters are tested to determine if they correlate with the calculations done in Section 4.4. This also assists in determining if the calculated torque is an accurate representation of the prototype's torque capability. The tests are described further in this chapter.

6.2 DC resistance test

The DC resistance test is performed to measure the resistance of the stator windings. This is done by circulating a direct current and then measuring the voltage drop between terminals. Because the current is DC, no voltage is induced in the rotor and thus no current flows in the rotor. The setup of the test is displayed in Figure 6-1.

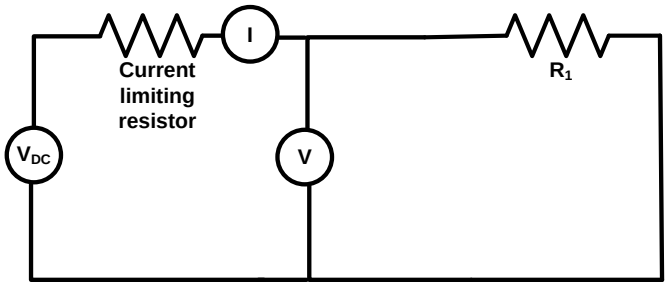

Figure 6-1: Equivalent circuit of the DC resistance test

The following equipment is required to conduct the test:

- DC voltage source (40 V)
- Optional current limiting resistor (6 Ω)
- Ammeter (50 A)
- Voltmeter (550 V)

A voltage drop only occurs over the stator resistance because direct current is being applied. The stator resistance is then determined by the applied direct current, I_{DC}, and the resultant DC voltage, V_{DC}, as follows

$$R_1 = \frac{V_{DC}}{I_{DC}}. \tag{6.1}$$

As stated previously in Section 4.4, the stator remains the same for the induction machine and the retrofit LSPMSM. The data is available on the WEG datasheet [9]. The results are displayed in Table 18. The results indicate that the measured stator resistance is within an acceptable range of the value indicated in the datasheet.

Table 18: Results of DC resistance test

Condition		R_1 (Ω)
7.5 kW induction motor	Datasheet	2.383
	Simulated	2.391
	Measured	2.411
Retrofit LSPMSM	Calculated	2.383
	Simulated	2.378
	Measured	2.403

6.3 Blocked rotor test

This test is also known as the short circuit test. The rotor is locked to prevent the shaft from turning, causing a slip of $s = 1$ and a low voltage is then applied to the stator terminals. The equivalent starting torque is also measured during this test. The equivalent circuit of the test is depicted in Figure 6-2. The wattmeter can be excluded if the test equipment is able to measure the amplitude and angle of the current and voltage.

The test is performed to determine the stator reactance, the rotor reactance and the rotor resistance.

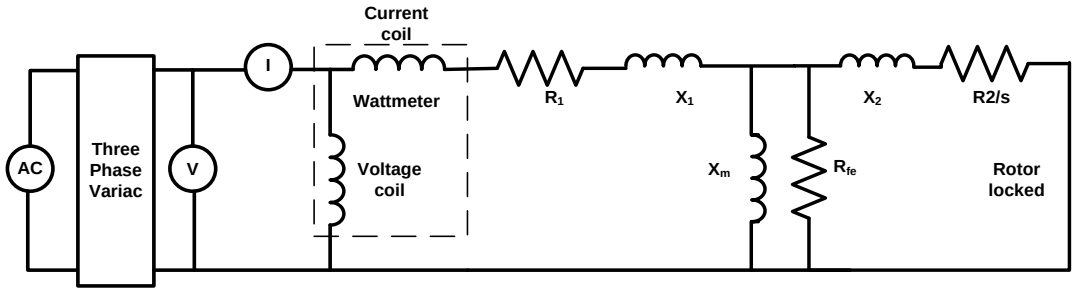

Figure 6-2: Equivalent circuit of the blocked rotor test

The equipment required for the blocked rotor test is as follows:

- Variable three phase AC voltage source or AC voltage source with a variac (up to 525 V)
- Ammeter (50 A)
- Voltmeter (550 V)

- Wattmeter (excluded if the test equipment is able to measure the amplitude and angle of the current and voltage)
- Clamp
- Torque meter (100 Nm)

The current, voltage and power are measured and used to determine the short circuit current, power factor and leakage reactance. During this test, the slip is unity and results in the rotor impedance, R_2 and X_2, being much smaller than the magnetising impedance, R_{fe} and X_m,. This causes the current flowing through the magnetising impedance to be negligible and thus the equivalent circuit only involves the stator and rotor impedances. The equivalent resistance, R_e, is the sum of the stator resistance, R_1, and rotor resistance, R_2, and is calculated by

$$R_e = \frac{P_{ph}}{I_{in}^2}. \tag{6.2}$$

P_{ph} is the total phase power and I_{in} is the line current. The stator resistance is determined from the DC resistance test and thus the rotor resistance can be calculated.

The equivalent impedance, Z_e, is calculated using the phase voltage, V_{ph}, and the phase current, I_{ph}, as follows

$$Z_e = \frac{V_{ph}}{I_{ph}}. \tag{6.3}$$

The equivalent leakage reactance, X_e, is the sum of the stator reactance, X_1, and rotor leakage reactance, X_2, and is determined as

$$X_e = Z_e^2 \quad R_e^2. \tag{6.4}$$

To calculate the individual stator and rotor leakage reactances, the relationship between X_1 and X_2 must be determined. The relationship is classified by the National Electrical Manufacturers Association (NEMA) [23] and the International Electrotechnical Commission (IEC) [24] based on induction motor performance such as starting current and stall torque. Table 19 displays the relationship according to the different classes. The original induction motor is classified as Design Class B (NEMA)/Design Class N (IEC) according to the manufacturer's data sheet.

Table 19: X1 and X2 relationship according to NEMA classes

NEMA Design Class	IEC Design Class	X_1 and X_2 Relationship
A	A	$X_1 = X_2$
B	N	$X_1 = (2/3)X_2$
C	H	$X_1 = (3/7)\ X_2$
D	No equivalent	$X_1 = X_2$

The stator and rotor leakage reactances for the induction machine are determined from the WEG datasheet [9]. The stator leakage reactance will again remain the same for the induction motor and the retrofit LSPMSM. The rotor leakage reactance of the LSPMSM was calculated in Section 4.4.

The calculated, simulated and measured results are displayed in Table 20.

Table 20: Results of the blocked rotor test

Condition		X_1 (Ω)	X_2 (Ω)	R_2 (Ω)	Starting Torque (Nm)
7.5 kW induction motor	Datasheet	5.748	7.722	1.622	25.8
	Simulated	5.756	7.42	1.619	26.3
	Measured	5.76	7.719	1.621	26
Retrofit LSPMSM	Calculated	5.748	8.01	2.122	32.2
	Simulated	5.623	7.54	2.24	33.8
	Measured	5.551	7.743	2.281	29.1

The stator reactance from the test result correlates with the theory that the parameter will remain the same because the stator is unchanged. There is a difference between the calculated results and the test results of the rotor parameters. The rotor resistance is calculated by adding the resistance of the rotor bar, R_{rotor_bar}, and the resistance of the section of the end ring, R_{end_ring}, connected to the bar. When the rotor slots were designed, it was with the intention of casting the rotor bars and this decision was used to determine the rotor bar area in Section 3.3.1 and hence the rotor resistance in Section 4.4. Casting

was not possible during the manufacturing process and the bars were manufactured instead. This has reduced the area of the rotor bars to allow for slotting of the bars into the lamination stack. From equation 3.62 it is clear that if the area is reduced, the resistance of the rotor bar increases.

$$R_{rotor\_bar} = \rho_{Al} \frac{l'}{A_{ur}} \tag{4.21}$$

The profile of the rotor bar was decreased by 0.5 mm which changed the area from 97.56 mm^2 to 92.31 mm^2 and thus the total rotor resistance from 2.122 Ω to 2.28 Ω. Similarly, this affects the rotor reactance. This is why there is a difference between the original calculated result and the result from the tests. The effect of the difference on the torque capability will be discussed in Section 6.8.

6.4 No load test

The no load test is also known as the open circuit test. This test is performed by operating the motor without an external load connected to it. Rated voltage is applied to the stator and the resultant current and output power are measured. When a motor runs without a load, the mechanical speed is between 97 – 99% of the synchronous speed. This means that there is very little slip and the rotor impedance becomes negligible. This test determines the values of the core resistance, R_{fe}, and the magnetising reactance, X_m, and thereby the losses of the motor. The equivalent circuit of the test is displayed in Figure 6-3.

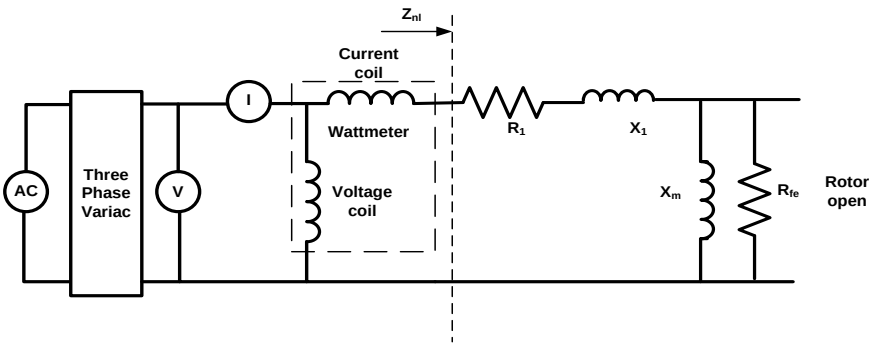

Figure 6-3: Equivalent circuit of the no load test

The equipment required for the no load test is as follows:

- Variable three phase AC voltage source or AC voltage source with a variac (up to 525 V)
- Ammeter (50 A)
- Voltmeter (550 V)

- Wattmeter (excluded if the test equipment is able to measure the amplitude and angle of the current and voltage)

The no load impedance, Z_{nl}, is calculated from the no load voltage, V_{nl}, and the no load current, I_{nl}

$$Z_{nl} = \frac{V_{nl}}{I_{nl}}. \tag{6.5}$$

The no load field impedance, Z_{fnl}, represents the parallel sum of X_m and R_{fe} and can be calculated by subtracting X_1 and R_1 from the no load impedance as follows

$$Z_{fnl} = Z_{nl} \quad (R_1 + jX_1). \tag{6.6}$$

The no load field admittance, Y_{fnl}, is given as

$$Y_{fnl} = \frac{1}{Z_{fnl}}. \tag{6.7}$$

The magnetising impedances, R_{fe} and X_m, are then calculated from

$$R_{fe} = \frac{1}{Re(Y_{fnl})}, \tag{6.8}$$

$$X_m = \frac{1}{Im(Y_{fnl})}. \tag{6.9}$$

The magnetising impedances for the induction machine were determined in Section 4.4. The results are displayed in Table 21. The results obtained from the no load test do not correspond with the calculated results. There is also a difference in the no load test results between the retrofit design without the permanent magnets and with the permanent magnets. This leads to the conclusion that the permanent magnets have an impact on the determination of the core resistance. Further investigation is required to determine how the effect can be accounted for during the design phase.

Table 21: Results of the no load test

Condition		R_{fe} (Ω)	X_m (Ω)
7.5 kW induction motor	Datasheet	5349.904	195.908
	Simulated	5340.847	197.02
	Measured	5350	195.91
Retrofit LSPMSM without permanent magnets	Calculated	3163.911	247.714
	Simulated	3089.07	214.939
	Measured	1154.83	204.241
Retrofit LSPMSM with permanent magnets	Calculated	3163.911	247.714
	Simulated	3089.07	227.842
	Measured	3809.28	204.241

6.5 Back-emf test

Back-emf is measured by measuring the voltage over the stator terminals while the machine is running at full speed and at no load. The back-emf is measured while the permanent magnets are slotted into position.

It was established during the testing that the calculated back-emf of the prototype is too high in comparison with the supply voltage which means that the machine will not operate correctly as a motor since the high back emf will keep it from synchronizing. The back-emf produced by the permanent magnet is related to the flux linkage as seen in equation 4.3. The flux linkage is a function of the flux generated by the permanent magnets, which in turn is dependent on the flux density, B_r. This means that the magnet's flux density is too high for the application, though the operating point for the magnetic circuit is correct. However, if a permanent magnet with a lower B_r was selected the required magnetic material volume would increase to maintain the same flux. This would result in a magnet with larger width and height and the problem of space for placement of the magnets arises. To illustrate the analysis, NdFeB 25BH permanent magnet with B_r = 1 T was used for the calculations in Table 22.

Table 22: Properties and dimensions of NdFeB 25BH

Permanent Magnet Property	Value
B_r	1 T
H_c	-830 kA/m
μ_{mag}	0.0012048
BH_{max}	225 kJ/m^3
B_{mag}	0.5 T
H_{mag}	-450 kA/m
Vol_{mag}	102.08 x10^{-6} m^3
h_{mag}	623 mm
Width	0.963 mm

The calculated volume of the NdFeB 25BH magnetic material is almost double the volume required of the NdFeB 48H magnetic material. The calculated height of the magnet to reduce cogging torque is nonsensical for the application. If a height of 10 mm is selected the required width is 60 mm. This provides a better placement of the magnets, but increases the leakage flux because the magnet end points will be situated closer together than the current prototype.

The conclusion is that when a permanent magnet is designed for an application, the load line still applies, but the back-emf must be calculated at the same time to facilitate the selection of the correct grade of material. If the stator windings could be reduced, the back-emf would also be reduced because the induced emf is directly proportional to the number of turns in the stator coils. This would mean the original volume of permanent magnet material could be used.

To reduce the back-emf of the prototype, only 105 mm of the 170 mm axial length of the permanent magnet material was placed into the rotor. This changed the RMS line-to-line voltage of the back-emf to E_m = 303.23 V. The calculated back-emf, using equation 5.3, and measured back-emf curves are displayed in Figure 6-4 while the simulated back-emf is displayed in Figure 6-5. The measured back-emf corresponds well with the new calculated curve.

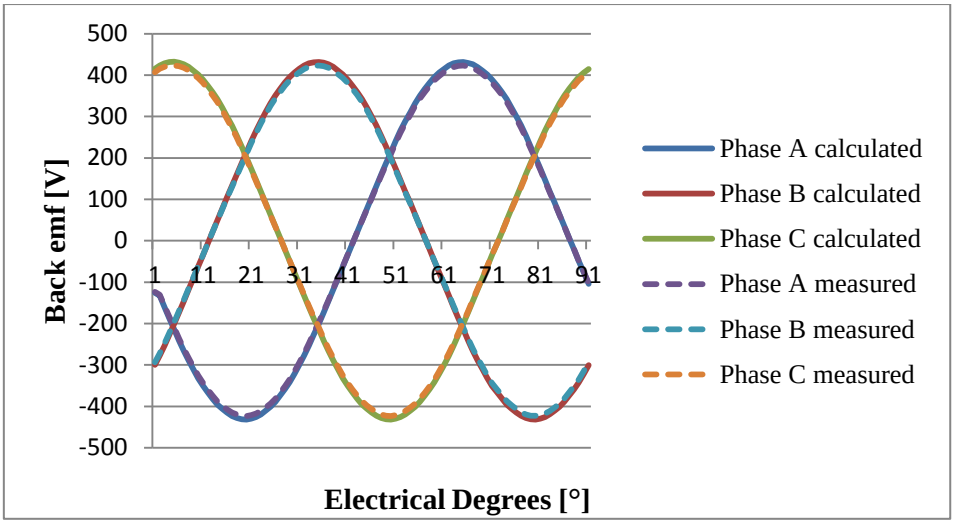

Figure 6-4: Calculated back-emf at no load with reduced magnet axial length

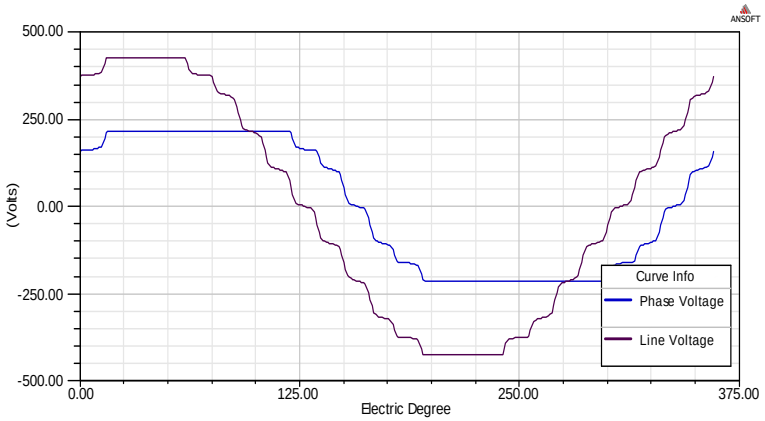

Figure 6-5: Simulated back-emf at no load with reduced magnet axial length

6.6 Cogging torque test

Permanent magnet machines experience cogging torque even when the motor is de-energised because of the presence of the field generated by the permanent magnets [25] [26]. This test can therefore be performed at zero speed or at a very low constant speed.

To perform the test at zero speed, a mechanical indexing fixture is used to rotate the motor through a known number of degrees. A torque meter is connected to the shaft of the motor and the resultant cogging torque is then displayed on an oscilloscope. A diagram of the cogging torque test setup is displayed in Figure 6-6.

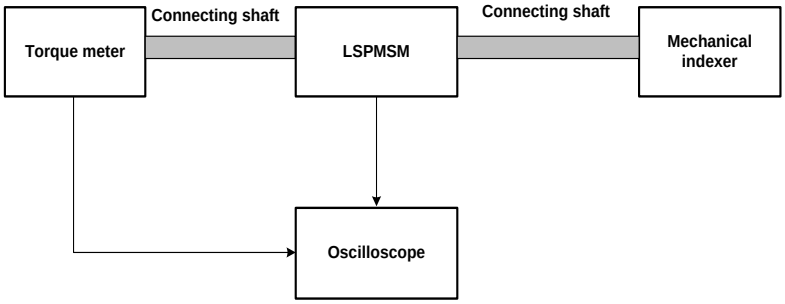

Figure 6-6: Cogging torque test diagram

From Figure 6-6, the equipment required for the cogging torque test is as follows:

- Torque meter (50 Nm, accuracy 0.01 Nm)
- Mechanical indexing fixture
- Oscilloscope

Cogging torque requires the simulation of the machine at various positions of the rotor and is typically expressed as a Fourier series [26]. Calculating the theoretical cogging torque was not an objective of this design, but the measurement of the cogging torque is still required to determine if it is within an acceptable range. The measured cogging torque is displayed in Figure 6-7. A very small section is displayed for viewing purposes. According to [25] and [26], the measured cogging torque is within an acceptable range. The DC offset is a result of the friction the machine experiences. The oscillation frequency is a function of the stator turns and the number of poles [26].

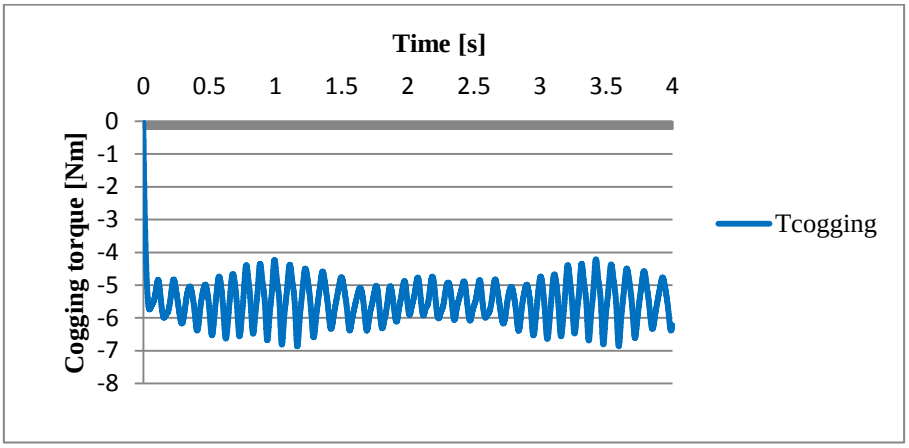

Figure 6-7: Measured cogging torque of the LSPMSM

6.7 Efficiency analysis

The efficiency of the motor was calculated in Section 4.3 as 92.6%, while the simulation indicated an efficiency of 93%. During the performance testing the input and output power was measured to determine the actual efficiency of the prototype. The measured efficiency at full load was 91.8% which correlates with the calculated and simulated results. A comparison between the measured and simulated efficiency plotted against the torque angle is displayed in Figure 6-8. The measured efficiency profile was determined by calculating the output power from the rotational speed and corresponding torque and dividing it by the input power. The simulated efficiency was determined from ANSYS Maxwell® as indicated in Section 4.3.5.

The efficiency of the equivalent induction machine is 90%. This means that the design process followed for the retrofit LSPMSM design was able to deliver a more efficient machine.

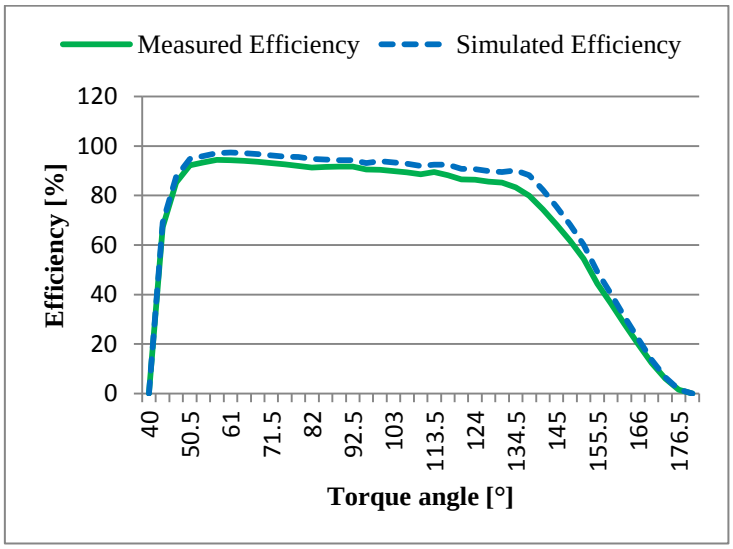

Figure 6-8: Comparison of measured and simulated efficiency

6.8 Torque analysis

Figure 6-9 depicts the torque curves determined from the design and the torque curve determined during testing. The induction machine torque curve is also displayed on the graph for comparison. The torque curve of the LSPMSM correlates well with the induction machine and has a higher starting torque. The measured torque curve indicates the presence of the torque ripple as caused by the cogging torque.

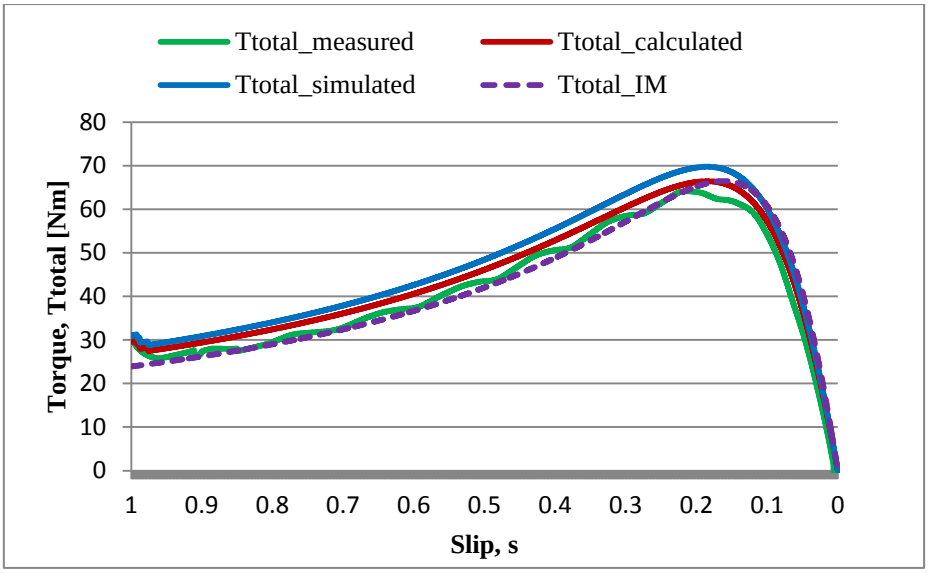

Figure 6-9: Torque comparison between design and performance testing

The starting torque from the test is 29.01Nm while the calculated starting torque is 32.2 Nm. The maximum torque achieved between the calculated results and the measured results differs by 7 Nm. From equation 4.1, the electromechanical torque is derived by

$$T_{em} = \frac{m_s U_s^2 \left(R_r^{'} / s\right)}{\left(\omega_s / p\right) \quad R_s + \frac{R_r^{'}}{s} \quad ^2 + \left(\omega_s L_k\right)^2} \tag{4.1}$$

As discussed in Section 6.3, there was a small difference between the calculated values and test results for the rotor resistance and rotor reactance. Even though the difference is small, based on equation 4.1 this would affect the torque because both values are squared below the line.

Although only 105 mm axial length of the permanent magnet material was installed, this did not have a significant impact on the final torque curve. This is because equation 4.1 is a function of the equivalent electric circuit parameters of the machine. The stator and rotor resistances are not affected by the permanent magnets and the leakage inductances are dependent on the air gap, slot sizes, tooth tips, end windings and skewing as noted in Section 4.2. The permanent magnets are sized to deliver the desired air gap flux density by the area of the permanent magnet and the magnet flux density. Although the volume of magnetic material was changed, the thickness of the magnet in the radial direction did not change and still satisfied equation 3.22.

The permanent magnets affected the braking torque because of the change in back-emf. It is evident from the measured results that the braking torque of the permanent magnets was not significant though and correlated with the theoretical results. This indicates that the rotor cage was able to overcome the effect of the permanent magnet's braking torque and in turn means that it is not a major limitation in the use of permanent magnets.

6.9 Conclusion

The test results indicate that there are some discrepancies between the calculated results and the performance results. The results obtained from the DC resistance test and blocked rotor test correspond with the calculated and simulated values. However, the results obtained from the no load test do not correspond with the calculated results. As stated in Section 6.4, the conclusion is that the permanent magnets have an impact on the determination of the core resistance.

The back-emf of the permanent magnets was a particular area of concern and it was noted that future permanent magnet sizing must use the load line method and the back-emf calculations at the same time.

The torque curve determined during testing corresponds with the theoretical torque curve. This indicates that the permanent magnets were able to generate the required torque and the rotor slots were sized appropriately to provide an adequate starting torque.

The effect of the braking torque generated by the permanent magnets for this design was deemed as minimal from the calculations, with the original back-emf as well as the recalculated back-emf. This was also verified during testing when the final torque curve was plotted.

Chapter 7 - Conclusion and Recommendations

This chapter draws conclusions regarding the design of the machine and the performance witnessed during testing. Recommendations for further development to improve the retrofit design are discussed.

7.1 Conclusions

The goal of this project was to design and fabricate a retrofit LSPMSM to provide a basis for an alternative to an induction machine. The design will be used for future optimisation strategies. This section concludes the design and the performance of the retrofit LSPMSM.

7.1.1 Design process

The intent of the retrofit LSPMSM design was to leave the stator of the induction machine intact and only design the appropriate rotor. This meant that some of the main machine parameters, such as the axial length, were already fixed because they relate to the stator. The rotor design was then divided in to the design of the rotor slots, the design of the permanent magnets and the design of the end ring.

The design of the rotors slots consists of the shape, size and number of slots. Special cognisance was paid to the skin effect on the rotor slots and how to account for this effect in the slot depth and slot opening. Cogging torque reduction techniques were also investigated which specifically looked at skewing, the amount of slots per pole and width of the permanent magnet. Skewing was not deemed a viable option because of the fixed stator and the difficulty that would be experienced trying to skew the permanent magnets. Rather, fractional slots per pole were used and the width of the permanent magnet optimised to aid in reducing cogging torque. As noted in Section 6.6, although cogging torque is present, the cogging torque is within an acceptable range.

The permanent magnets are designed by considering the magnetization, the permanent magnet orientation and the actual size of the permanent magnet. As discussed in Section 3.2, a radial flux permanent magnet configuration is the only option available for the retrofit design because the stator has been developed for radial flux. The required air gap flux density was set and the equivalent magnetic circuit of the rotor structure was determined. The magnet was sized by selecting a material capable of producing the required flux density at the motor's operating temperature and then choosing an operating point to yield the maximum energy product. The equivalent magnetic circuit and the operating point of the permanent magnet were used to calculate the dimensions of the permanent

magnet. It was identified that the back-emf of the selected material was too high for the prototype and hence less magnetic material was used in the final testing.

Despite the problems experienced with the permanent magnet sizing, the design process still delivered a machine more efficient than the equivalent induction machine.

7.1.2 Fabrication process

With the stator available, only the rotor components were fabricated. The rotor steel was made up of laminations pressed together to form a stack. A stainless steel shaft with keys was used to keep the stack in place. The round rotor bars were simple to slide into the rotor slot positions in the stack. The location of the permanent magnets within the lamination stack was such that the end rings only covered the rotor slots and did not overlap the permanent magnets. The end rings could put into place before the permanent magnets were slotted into the lamination stack. This ensured that the permanent magnets were not exposed to the high temperature experienced while the end rings were welded into position. As discussed in Section 2.2.1, a permanent magnet can lose its magnetisation if exposed to comparatively high temperatures.

7.1.3 Operation

The permanent magnets were slotted into the rotor after all the other components were put in place. This allowed for testing of the machine before the permanent magnets were slotted into position to determine a baseline. The permanent magnets were then slotted into position to determine the effect of the magnets.

The torque curve from the test results corresponded with the theoretical torque curve and it was noted that the braking torque had a negligible effect on the performance. However, the efficiency of the machine was lower than expected and this will require further development with regards to optimisation strategies.

Although most of the calculated machine parameters corresponded with the test results, the core resistance could not be validated against the calculations. As mentioned in Section 6.7, the permanent magnets affected the value of the core resistance significantly. This indicates that the testing methods used on the LSPMSM are not sufficient in determining all the equivalent electric circuit parameters.

7.2 Recommendations

This section looks at recommendations to improve the design and fabrication of the retrofit LSPMSM. Opportunities for further development are also explored.

7.2.1 Design

The purpose of the retrofit design was to implement a rotor using permanent magnets in a stator of an induction machine. Attention was paid to the machine's ability to start on load and to reach its steady state and this was proved successful during the performance testing. However, this design did not look at the transient behaviour of the LSPMSM which would affect the machine's efficiency and its ability to be connected to a large distribution network. Network stability is very important in electrical networks and thus more research on the effect of LSPMSMs on distribution networks is advised. If a LSPMSM cannot be connected to a distribution effectively, then it would not serve as an appropriate replacement for an induction machine in industrial use.

As stated in Section 6.5, careful consideration must be taken when selecting the grade of permanent magnet material. When applying the load line design principle, the back-emf must also be determined at the same time. Simply selecting a material with a lower flux density without performing the calculations again is not viable because the volume of magnetic material required will change. The new required volume can lead to other problems, such as the end points of the magnets being to close in proximity. The example used in Section 6.5 would create more leakage flux which would lower the air gap flux density.

7.2.2 Fabrication

The rotor bars for the retrofit design were fabricated separately and then inserted into the rotor slots. An investigation into the effect of casting the rotor bars directly into the rotor slots is recommended. Casting the bars ensures a unity space factor. As discussed in Section 6.3, inserting a rotor bar separately does not guarantee that the entire slot will be filled because space is necessary for insertion. This affects the space factor and hence affects the required slot area as seen in Section 3.3.1. This would in turn affect the current density and ultimately increase the bar resistance, lowering the starting torque. The starting torque of the design was deemed sufficient during testing, which indicates that the current density in the slot was higher than selected.

7.2.3 Further development

7.2.3.1 Design considerations

Skewing is a common technique applied to small motors to reduce permeance harmonics and cogging torque [12]. However, skewing was not implemented in the rotor structure because of the difficulty in skewing the permanent magnets. A method to skew the permanent magnets should be investigated.

An optimisation strategy must be developed for the design process of the retrofit LSPMSM to improve the efficiency of the machine.

7.2.3.2 LSPMSM testing

The retrofit LSPMSM was tested using the common tests applied for induction machines to determine the equivalent electric circuit parameters. Although, most of the test yielded results similar to the theoretical values, there were still discrepancies between the results, particularly the core resistance and magnetising reactance. Other testing methods to determine the motor parameters and the effect of permanent magnets on these parameters must be investigated.

7.2.3.3 LSPMSM distribution network modelling

No LSPMSM model currently exists to allow for simulation of the machine in a distribution network. Software packages such as DigSilent and ETAPP only have models for induction machines and synchronous machines. These packages allow for simulation of the model under steady state, transient, fault conditions and many others. When a machine is analysed, specific attention is paid to dynamic starting, power dip ride-through and the event of loss of power to the machine. If a LSPMSM is to be an effective future replacement for an induction machine, this model must be developed to determine the machine's integration to the distribution network.

References

[1] J. F. Gieras and M. Wing, Permanent Magnet Motor Technology, second edition, volume 1. M Wing, New York: Marcel Dekker Inc., 2002.

[2] P. W. Hung, S. H. Mao, and M. C. Tsai, "Investigation of line start permanent magnet synchronous motors with interior-magnet rotors and surface-magnet rotors," Electrical Machines and Systems, pp.2888 - 2893, October 2008.

[3] A. S. Langsdorf, Theory of Alternating Current Machinery, second edition, volume 1. New York: McGraw-Hill, 1955, pp. 245.

[4] J. Pyrhönen, T. Jokinen and V. Hrabovcová, Design of Rotating Electrical Machines, first edition, volume 1. West Sussex: John Wiley & Sons, 2008.

[5] Magcraft, "Permanent Magnet Selection and Design Handbook" Internet: http://www.rare-earth-magnets.com/Permanent-Magnet-Selection-and-Design-Handbook.pdf, Apr. 2007 [30 Jan. 2012]

[6] J. Santiago and H. Bernhoff. "Comparison between Axial and Radial Flux PM Coreless Machines for Flywheel Energy Storage", Journal of Electrical Systems, Issue 2, volume 6, June 2010.

[7] M. R. Dubois, Optimized Permanent Magnet Generator Topologies for Direct-Drive Wind Turbines, first edition, volume 1. Technical University Delft, Canada: Les Imprimeries ABC Inc., 2004, pp. 17.

[8] S. Speak, "Advanced Low Voltage Brushless Motor Technology". Internet: http://www.ecycle.com/Brushless_Motor_Technology.html, 21 Jun. 2011 [21 Feb. 2012].

[9] WEG, http://www.weg.net/za. [2011 – 2014].

[10] K. Zhang, X. Jiang, Y. Wu, L. Zhang and X. Wu, "Effect of slot shape in rotor of electrical motor with high-speed spindle on slot ripples" in *Proceedings of the 2010 International Conference on Modelling, Identification and Control*, Japan, July 2010.

[11] M. Benecke, R. Doebbelin, G. Griepentrog and A. Lindemann, "Skin Effect in Squirrel Cage Rotor Bars and Its Consideration in Simulation of Non-steady-state Operation of Induction Machines" in *Proceedings of Progress In Electromagnetics Research Symposium*, Marrakesh, Morocco, March 2011.

[12] Z. Q. Zhu, "Reduction of Cogging Torque in Interior-Magnet Brushless Machines" in *IEEE Transactions on Magnetics*, volume 39, pp. 3238 – 3240, Sept. 2003.

[13] X. Wang, T. Ding, Y. Yang, C. Zhu and D. Wang, "Study of Cogging Torque in Line-Start Permanent Magnet Synchronous Motors" in *Proceeding of the CSEE*, vol. 25, 2005, pp. 167 – 170.

[14] D. C. Hanselman, Brushless Permanent Magnet Motor Design, first edition, volume 1. United States of America: McGraw-Hill, 1994, pp. 120 – 121.

[15] A. E. Fitzgerald, C. Kingsley and S. Umans, Electric Machinery, sixth edition, volume 1. New York: McGraw-Hill, 2003, pp. 32 – 34.

[16] Rare-Earth Permanent Magnets. (2011) www.bakkermagnetics.com.

[17] D. Dolinar., "Calculation of two-axis induction motor model parameters using finite elements" in *IEEE Transactions on Energy Conversion,* volume 12, pp. 133 – 142, June 1997.

[18] S. L. Nau, WQuattro Motors WEG Line-Start Permanent Magnet Motors, 2009.

[19] S. Tumanski, Handbook of Magnetic Measurements, first edition, volume 1. CRC Press, 2011, pp. 129 – 130.

[20] F. J. H. Kalluf, C. Pompermaier, M. V. Ferreira da Luz and N. Sadowski, "Braking Torque Analysis of the Single Phase Line-Start Permanent Magnet Synchronous Motor" in *XIX International Conference on Electrical Machines*, Rome, 2010.

[21] V. B. Honsinger, "Permanent Magnet Machines: Asynchronous Operation" in *IEEE Transactions on Power Apparatus and Systems*, volume PAS-99, pp. 1503 – 1509, 1980.

[22] Y. S. Chen and Z. Q. Zhu, "Calculation of d- and q-Axis Inductances of PM Brushless AC Machines Accounting for Skew" in *IEEE Transactions on Magnetics*, volume 41, pp. 3940 – 3942, Oct. 2005.

[23] NEMA standard MG-1 Motors and Generators.

[24] International Electrotechnical Commission Standard 60085 Electrical Insulation - Thermal Evaluation and Designation, 3rd edition, 2004.

[25] H. Karmaker, "Report on IEEE Standard Working Group P1812 on Guide for Testing Permanent Magnet Machines" in *IEEE Transactions on Magnetics*, volume 46, pp. 2327 – 2333, 2012.

[26] L. Dosiek, "Cogging Torque Reduction in Permanent Magnet Machines" in *IEEE Transactions on Industry Applications*, volume 43, pp. 1565 – 1571, 2007

.

Appendix A: Flow Diagrams

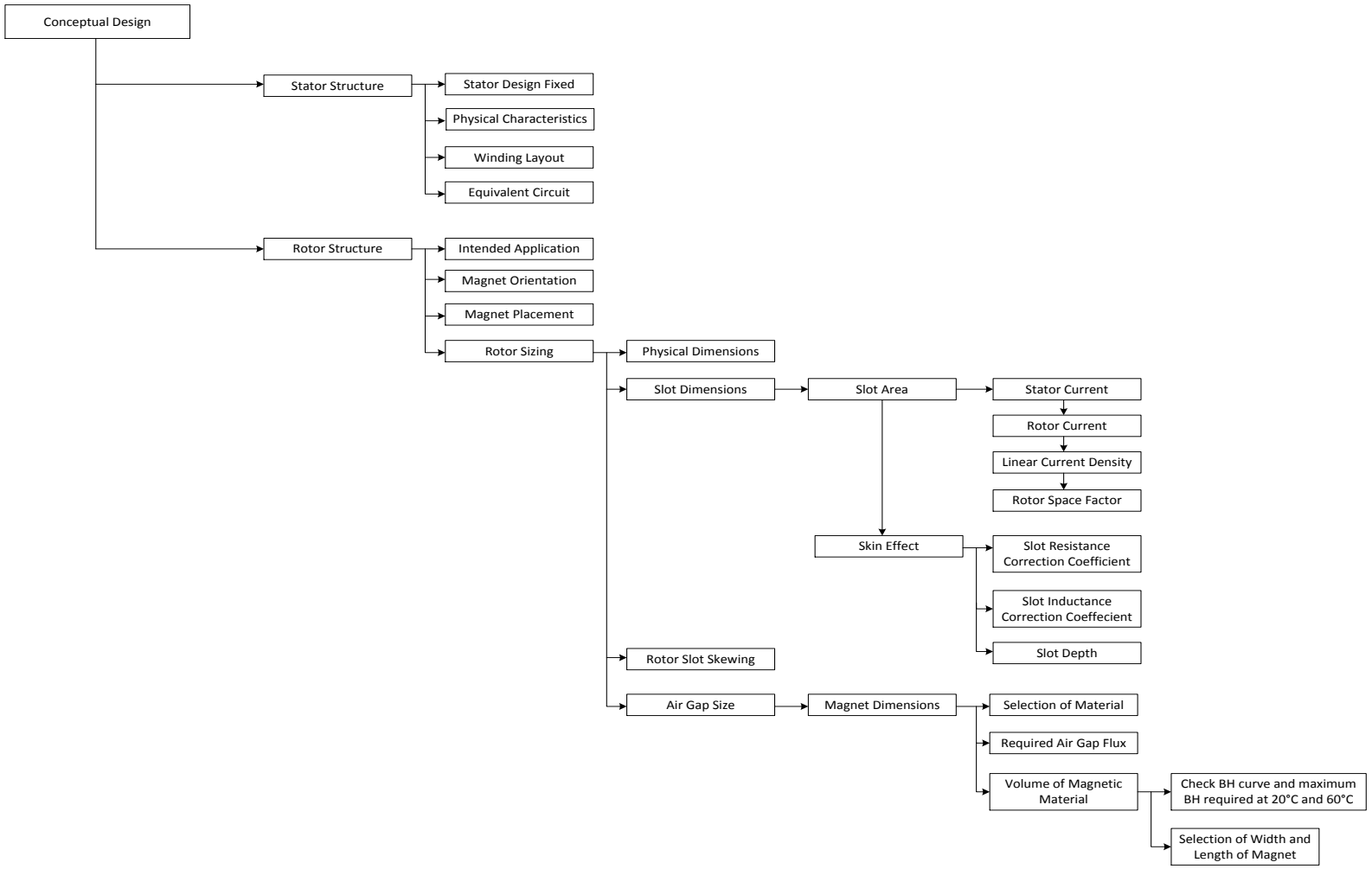

Figure A - 1: Conceptual design flow diagram

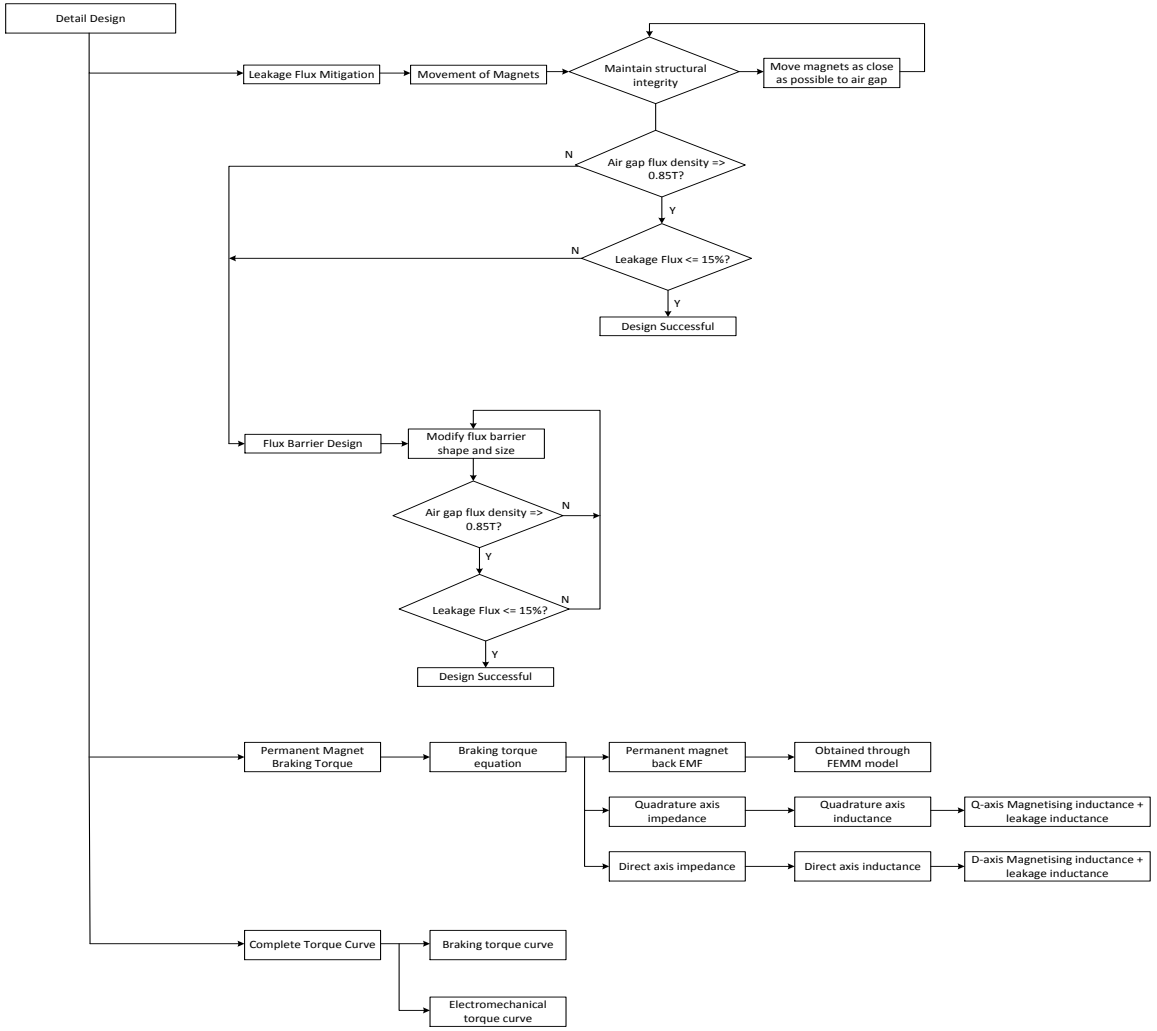

Figure A - 2: Detail design flow diagram

Appendix B: Mechanical losses

Mechanical losses are calculated by [4]

$$P_{pw1} = \frac{1}{32} k C_M \pi \rho \Omega^3 D_r^4 l_r$$

$$P_{pw2} = \frac{1}{64} C_M \rho \Omega^3 \left(D_r^5 \quad D_{ri}^5 \right).$$

The torque coefficient for each equation is different. For determing P_{pw1}, C_M is a function of the Couette Reynolds number $R_{e\delta}$. The Couette Reynolds number is calculated as

$$R_{e\delta} = \frac{\rho \delta \Omega D_r}{2\mu} = \frac{1.1132 * 0.005 * 53.4 * 0.149}{2 * 1} = 0.022 .$$

$R_{e\delta}$.is less than 64 and thus the following equation for calculating C_M applies [4]

$$C_M = 10 \frac{\left(2\delta / D_r\right)^{0.3}}{R_{e\delta}} = 12.253$$

$$P_{pw1} = \frac{1}{32} * 1.1132 * 12.253 * 3.14 * (53.4)^3 (0.149)^4 * 0.17 = 17.092 \text{ W}$$

The torque coefficient for determing P_{pw2} is dependent on the Tip Reynolds number R_{er}

$$R_{er} = \frac{\rho \Omega {D_r}^2}{4\mu} = \frac{1.1132 * 53.4 * 0.149^2}{4 * 1} = 0.33$$

R_{er}.is less than $3 \text{x} 10^5$ and thus the following equation for calculating C_M applies [4]

$$C_M = \frac{3.87}{{R_{er}}^{0.5}} = 6.737$$

$$P_{pw2} = \frac{1}{64} * 1.347 * 1.1132 * (53.4)^3 \left(0.149^5 \quad 0.038^5\right) = 1.31 \text{ W}$$

Appendix D: Presented article

Presented at the 23rd Southern African Universities Power Engineering Conference, (SAUPEC), Johannesburg, January 2015.

ROTOR DESIGN OF A RETROFIT LINE START PERMANENT MAGNET SYNCHRONOUS MOTOR

K. Garner*and A.J. Grobler**

** School of Electrical, Electronic and Computer Engineering, North West University, Potchefstroom, South Africa, E-mail: karen.garner@sasol.com*
*** School of Electrical, Electronic and Computer Engineering, North West University, Potchefstroom, South Africa, E-mail: andre.grobler@nwu.ac.za*

Abstract: The increasing need for energy and the lack of energy resources available has prompted designers to focus on improving the efficiency of equipment. Motors utilise a considerable portion of the electrical energy generated and thus improving the efficiency of these machines would reduce the overall power consumption. Research has indicated that permanent magnet synchronous machines (PMSM) offer improved efficiency when compared to induction machines. A retrofit design where the stator of an induction machine is kept intact and the rotor substituted with a permanent magnet core is proposed as a solution. A retrofit design is considered because of the ease of manufacturing for motor suppliers and the ability to apply the solution to existing operating induction machines. This paper focuses on the principles followed to design the permanent magnet rotor for a retrofit line start permanent magnet synchronous machine (LSPMSM).

Keywords: Rotor design, LSPMSM, PMSM, retrofit, permanent magnet, dimensions

1. INTRODUCTION

Our energy resources are under tremendous pressure with society's ever increasing need for electricity. There is an urgent need to look at how we are expending all the energy generated and to reduce our energy consumption. Studies have indicated that 65% of electrical energy is converted to heat and mechanical energy by electric motors [1]. Majority of these motors are three-phase induction motors and are mostly used in fan and pump applications [1]. Motors with a higher efficiency reduce energy losses, resulting in reduced operating costs. If designed correctly, a permanent magnet machine can be more efficient than an induction machine because permanent magnets eliminate the rotor excitation losses found in induction machines. A retrofit design of a three-phase induction motor is considered. The standard rotor of an induction motor is substituted with a rotor fitted with permanent magnets and the stator and frame of the induction motor is kept intact. The retrofit design is considered because a motor supplier will not need to replace its entire production line, but only replace its rotor design. The retrofit will also allow induction motors currently operating to be changed to a permanent magnet solution with minimal impact. A motor with increased efficiency can then be achieved without increasing the size of the motor.

An alternative solution is to construct a line start permanent magnet synchronous machine (LSPMSM) with a new rotor and stator. This allows the designer to manufacture a smaller machine able to deliver the same power output as an induction machine. The smaller construction is attributed to the fact that permanent magnet synchronous machines (PMSM) have lower operating temperatures because there are no rotor bar currents [2]. The lack of rotor bar currents means that the rotor losses are eliminated and hence the efficiency of the machine is increased. The increased efficiency of the PMSM yields a higher power output than an induction machine of the same power rating [2]. Although a LSPMSM designed with a new rotor and stator will yield a smaller machine, it will not be feasible for replacing existing induction machines because of the impact on the installation.

2. ROTOR DESIGN

The following parameters have to be determined for the rotor of the retrofit LSPMSM:

- Direction of magnetisation
- Rotor slot dimensions
- Permanent magnet orientation
- Permanent magnet dimensions
- Flux barrier dimensions

A LSPMSM is a hybrid between an induction machine and a synchronous machine. The current densities for the retrofit design are chosen based on the suggested limits for the induction machine and the salient pole synchronous machine. The stator of the existing induction machine used for the retrofit design is developed for radial flux. Thus, a radial flux permanent magnet configuration is used. Embedded magnets are used for the prototype because the axial length of the machine is fixed. Using surface-mounted permanent magnets would lengthen the axial length of the rotor.

3. ROTOR SLOT DIMENSIONS

3.1. Slot area

The number of rotor slots is chosen by considering the number of poles and the number of stator slots. There are many requirements for choosing the rotor slot number, such as the rotor slot number must be as small as possible

to minimise asynchronous torques. Considering the requirements in [3] and that there are 48 slots in the stator, the number of rotor slots is chosen as 30. It is also important to keep the number of slots as low as possible to aid manufacturing. The rotor slot area is calculated by determining the stator and rotor currents. The stator current I_s can be calculated as follows

$$I_s = \frac{P}{m\eta V_{sph}\cos\varphi} \tag{1}$$

where P is the shaft power, m is the number of phases, η is the efficiency, $\cos\varphi$ is the power factor and V_{sph} is the stator phase voltage. The rotor current I_r is a factor of the stator current and is determined by [3]

$$I_r = \left(\frac{z_Q}{a}\right)\left(\frac{Q_s}{Q_r}\right) I_s \cos\varphi \tag{2}$$

where z_Q is the amount of conductors per slot, a is the number of parallel paths in the windings which is equal to 1 for a squirrel cage machine, and Q_s and Q_r represent the number of stator slots and rotor slots respectively. The area of the conductive material in the slot must be calculated in order to calculate the slot area. This is calculated using the current density J. Choosing a higher current density yields a smaller cross-sectional area of the conductive material and thus a higher resistance. A higher rotor resistance provides an increased starting torque because torque is proportional to the rotor resistance at low values of slip. The area of the rotor's conductive material A_{cr} is given by [3]

$$A_{cr} = \frac{I_r}{a_r J_r}. \tag{3}$$

The area of the rotor slots A_{ur} is then calculated as

$$A_{ur} = \frac{z_Q A_{cr}}{k_{cu,r}} \tag{4}$$

where $k_{cu,r}$ is the space factor and is dependent on the conductive material of the machine. A space factor is a ratio of the area of conductive material in a slot and the area of the slot itself. Aluminium casted bars are intended for the design, making $k_{cu,r} = 1$.

3.2. Slot shape

The dimensions of the rotor slot need to be determined to form the appropriate shape. A circular slot shape was selected for this design. Most slot shapes are grouped into pear-shaped, trapezoidal or circular. Pear-shaped slots are more effective at weakening torque ripples, but the torque results between the three types vary marginally on the fundamental flux density [4]. The diameter of the slot is determined from the area, but the depth of the slot and the width of the opening required must also be determined to minimise the skin effect on the slots. The skin effect decreases a conductor's current-carrying capacity. It occurs in a rotor because at a low rotational speed, the rotor current frequency is increased and the current in the rotor slots is displaced in a radial direction towards the air gap as depicted in Figure 1 [5]. The coil located deepest in the slot experiences a stronger leakage field and has the highest leakage inductance in comparison to the coils locates close to the air gap. The rotor current concentrates in the upper coils. The conductive cross-section of the slot is decreased and the resistance of the rotor bar increases.

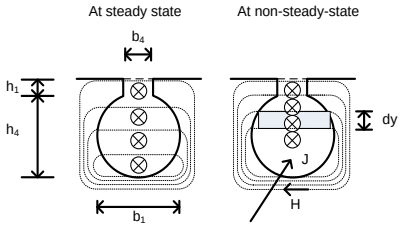

Figure 1: Skin effect on a rotor slot [5]

The correction coefficients for the slot resistance k_R and the slot inductance k_X are determined by [6]

$$k_R = \xi\frac{\sinh 2\xi + \sin 2\xi}{\cosh 2\xi - \cos 2\xi} \tag{5}$$

$$k_X = \frac{3}{2\xi}\frac{\sinh 2\xi - \sin 2\xi}{\cosh 2\xi + \cos 2\xi} \tag{6}$$

where ξ is the reduced conductor factor. To determine the best dimensions of the slot to minimise the skin effect, the correction coefficients should be 1. The reduced conductor factor, ξ, is then calculated and used to determine the slot opening for the various scenarios of slip. The depth of the slot δ_{skin}, or h_1, is calculated by [7]

$$\delta_{skin} = \sqrt{\frac{2}{\omega\mu_0\mu_r\sigma_{Al}}} \tag{7}$$

where ω is the frequency in radians, μ_0 is the permeability of free space, μ_R is relative permeability of the material and σ_{Al} is the electrical conductivity of aluminium.

4. PERMANENT MAGNET DIMENSIONS

Flux is the product of the flux density and the area of the material. The permeability of the core steel is assumed infinite compared to the permeability of the permanent magnet and the air gap. Deriving from this assumption, the permanent magnet's flux Φ_{mag} is equal to the air gap's flux Φ_g. This assumption neglects the effect of leakage flux and fringing and is a first order approximation [9]. The following can then be applied

$$A_{mag}B_{mag} = A_g B_g \text{ and} \tag{8}$$

$$B_g = \frac{A_{mag}}{A_g} B_{mag} \tag{9}$$

where A_{mag} is the area of the permanent magnetic material, B_{mag} is the flux density of the permanent magnet, A_g is the area of the air gap and B_g is the flux density of the air gap. In order to size the magnet

appropriately a material and grade must be chosen for the application. The selection is based on the typical flux density the magnet is capable of producing at 60°C which is the temperature the motor is designed to reach during operation. NdFeB 745TP is selected for the application. The operating point (B_{mag}, H_{mag}) of the permanent magnet must be calculated using the load line created by the magnet's remanence B_r and coercivity H_c. The load line is shown in Figure 2.

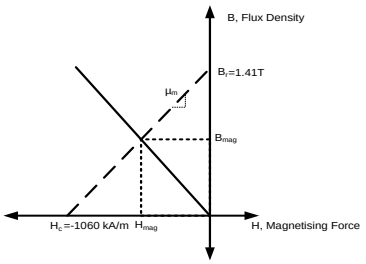

Figure 2: Load line of NdFeB Vacodym 745TP

The operating point of the material, B_{mag} and H_{mag}, is taken as the midpoint of the B-H curve in the second quadrant as indicated in Figure 2. B_{mag} is taken as half of B_r and the equivalent H_{mag} is then determined. The product of B_{mag} and H_{mag} yields the maximum energy product of the magnet. Using the maximum energy product yields the smallest volume of material able to produce the desired air gap flux density [9]. Drawing from the simplified magnetic circuit, the magneto motive force drop across the air gap and the permanent magnet is equal, but opposite in polarity as shown in [9]

$$\frac{H_{mag}h_{mag}}{H_g\delta} = -1. \tag{10}$$

where H_{mag} is the field intensity of the permanent magnet at maximum energy product, h_{mag} is the height of the permanent magnet, H_g is the field intensity of the air gap and δ is the thickness of the air gap. (10) can be solved for H_g and then for B_g as follows

$$H_g = -\frac{H_{mag}h_{mag}}{\delta} \tag{11}$$

$$\frac{B_g}{\mu_0} = \frac{H_{mag}h_{mag}}{\delta} \tag{12}$$

If (11) is multiplied with (12), then the following equation is obtained

$$B_g^2 = -\mu_0 \frac{h_{mag}}{\delta}\frac{A_{mag}}{A_g} H_{mag}B_{mag} \tag{13}$$

$$B_g^2 = -\mu_0 \frac{Vol_{mag}}{Vol_g} H_{mag}B_{mag} \tag{14}$$

where Vol_{mag} is the volume of the permanent magnetic material and Vol_g is the volume of the air gap. The required volume of magnetic material per pole Vol_{mag} is calculated from (14) and using the maximum energy product of the material as

$$Vol_{mag} = \frac{Vol_g B_g^2}{\mu_0\left(-H_{mag}B_{mag}\right)} \tag{15}$$

where Vol_g is volume of the air gap. The maximum volume of the magnetic material is then deduced as $50.960\text{x}10^{-6}$ m^3. The equivalent BH product must be within the limit of the maximum BH of the material at the operating temperature. A rectangular shape is used for the permanent magnet and the depth is governed by the axial length of the rotor. The magnet thickness must be kept to a minimum to minimise the effect of the cogging torque and still provide enough flux [10]. As stated previously, the permeability of the core steel is assumed infinite. The following equation is obtained

$$\oint Hdl = H_{mag}h_{mag} + H_g\delta = 0 \tag{16}$$

(11) is then rewritten to obtain the thickness of the magnet, h_{mag} [9]

$$h_{mag} = -\frac{\left(H_g\delta\right)}{H_{mag}}. \tag{17}$$

The field strength of the air gap, H_g, is determined as follows

$$H_g = \frac{B_g}{\mu_r\mu_o} \tag{18}$$

The air gap flux density was chosen as B_g = 0.85T and $\mu_0\mu_r = 4\pi\text{x}10\text{-}7$ H/m which is the permeability of air. Substituting (18) into (17) gives

$$h_{mag} = -\frac{\frac{B_g}{\mu_r\mu_0}\,\delta}{H_{mag}}. \tag{19}$$

The required area is known as well as the thickness of the permanent magnet, h_{mag} = 6.5 mm. The required width of the permanent magnet is then calculated as 56 mm. The permanent magnets have been sized according to the application and corresponding magnetic circuit. The load line of the circuit is displayed in Figure 3 to indicate that the permanent magnets will operate within the designed operating point. The intersection of the load line of the magnetic circuit and the load line of the permanent magnet occurs at (0.789 T; -450 kA/m) at 60°C.

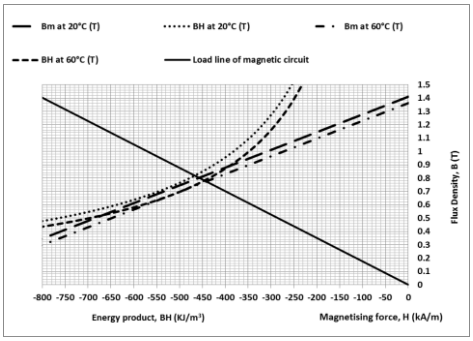

Figure 3: Load line of magnetic circuit intersecting with load line of the permanent magnet

5. FLUX BARRIER DIMENSIONS

Approximately 25% of the flux generated by an embedded permanent magnet is lost at the end points of a magnet [11]. Surface-mounted permanent magnets lose 5-10% of their flux. The literature on embedded permanent magnets does not give guidance on the lowest leakage flux obtainable, but it was decided to reduce the loss to 15%. In order to reduce the leakage flux, flux barriers are created at the ends of a magnet as depicted on the left of Figure 4. Air gaps are used as flux barriers in this design to channel more of the flux away from the magnet and towards the machine's air gap. The best solution for this application would be to join the flux barriers to the machine's air gap. This reduces the leakage flux to less than 10%, but splits the rotor laminations into four sections which are difficult to assemble. The design depicted on the right of Figure 4 was selected as the final design of the flux barriers to reduce the loss to 15%.

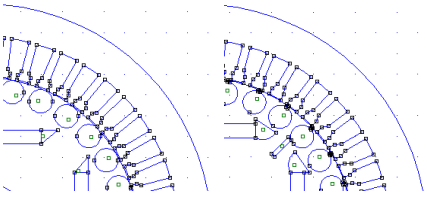

Figure 4: Model with original flux barriers on the left and final flux barriers on the right

6. TESTING

The prototype is tested in order to conclude if the machine can be used as a replacement for an equivalent induction machine. The 7.5 kW induction machine is tested first to establish a set of base parameters to be used for the comparison. The designed rotor is tested with and without the permanent magnets because the losses due to friction and windage are measured when the machine has no excitation. It is not possible to obtain zero excitation in a permanent magnet machine and hence the machine is tested without the permanent magnets [12].

The same tests are conducted on the induction machine and the LSPMSM. The tests are:

1. DC resistance test of the stator windings
2. Blocked rotor test
3. No load test
4. Back-emf (only for the LSPMSM)
5. Cogging torque test (only for the LSPMSM)
6. Final torque curve

6.1. Equivalent circuit parameter results

The equivalent circuit parameter results are displayed in Table 1.

Table 1: Equivalent circuit parameter test results in Ohms

Parameter	7.5kW Induction Machine	Retrofit LSPMSM Calculated	Retrofit LSPMSM Measured
R_1	2.383	2.383	2.423
X_1	5.748	5.748	5.551
R_2	1.622	2.122	2.281
X_2	7.722	8.01	7.743
R_{fe}	5349.904	3163.911	3809.28
X_m	195.908	247.714	204.241

There is a difference between some calculated and measured results. The rotor resistance is calculated by adding the resistance of the rotor bar, R_{rotor_bar}, and the resistance of the section of the end ring, R_{end_ring}, connected to the bar. When the rotor slots were designed, it was with the intention of casting the rotor bars and this decision was used to determine the rotor bar area and the rotor resistance. Casting was not possible during the manufacturing process and the bars were manufactured instead. This reduced the area of the rotor bars to allow for slotting of the bars into the lamination stack. The rotor bar resistance, R_{rotor_bar}, is determined as follows

$$R_{rotor\_bar} = \rho_{Al} \frac{l'}{A_{ur}} \tag{20}$$

where l' is the equivalent length of the machine and ρ_{Al} is the resistivity of aluminium. It is clear that if the area is reduced, the resistance of the rotor bar increases. The profile of the rotor bar was decreased by 0.5 mm which reduced the area by 5% and increased the resistance by 7.5%. Similarly, this affects the rotor reactance.

The results obtained from the no load test do not correspond with the calculated results. There is also a difference in the no load test results between the retrofit design with and without the permanent magnets. This leads to the conclusion that the permanent magnets have an impact on the determination of the core resistance and magnetising reactance. Further investigation is required to determine how the effect can be accounted for during the design phase.

6.2. Back-emf results

The calculated back-emf is displayed in Figure 5. It was established during the testing that the calculated back-emf of the prototype is too high in comparison with the supply voltage which means that the machine will not operate correctly as a motor since the high back emf will keep it from synchronizing. The back-emf, E_m, produced by the permanent magnet is related to the permanent magnet flux Φ_{mag}, the winding factor k_w, the number of stator turns N_s and the number of magnets N_m, as follows

$$E_m = k_w N_s N_m \Phi_{mag} \tag{20}$$

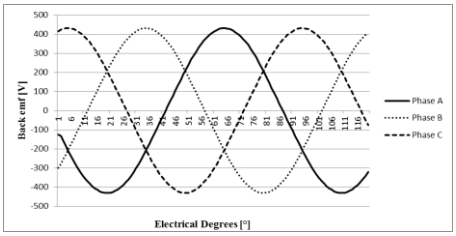

Figure 5: Calculated back-emf of the prototype

The flux generated by the permanent magnets is dependent on the flux density, B_r. This means that the magnet's flux density is too high for the application, though the operating point for the magnetic circuit is correct. However, if a permanent magnet with a lower B_r was selected the required magnetic material volume would increase to maintain the same flux. This would result in placement constraints. If a permanent magnet with B_r = 1 T was used, such as NdFeB Vacodym 688 AP, the required volume would be 102.08 x10^{-6} m^3. The required height to minimise cogging torque would then be h_{mag} = 623 mm which is impractical for the application. If a height of 10 mm is selected, the required width is 60 mm. This provides a better placement of the magnets, but increases the leakage flux because the magnet end points will be situated closer together than the current prototype.

The conclusion is that when a permanent magnet is designed for an application, the load line still applies, but the back-emf must be calculated at the same time in order to select the correct material grade. If the stator windings could be reduced, the back-emf would also be reduced because the induced emf is directly proportional to the number of turns in the stator coils. The original volume of permanent magnet material could be used. To reduce the back-emf of the prototype, only 105 mm of the 170 mm axial length of the permanent magnet material was placed into the rotor. This changed the RMS back-emf to E_m = 303.23 V. The recalculated and the measured back-emf curves are displayed in Figure 6. For display purposes, only Phase A is shown. The calculated and measured values correlate well.

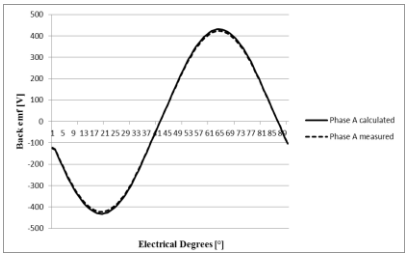

Figure 6: Re-calculated and measured back-emf of the prototype

6.3. Cogging torque results

Cogging torque requires the simulation of the machine at various positions of the rotor and is typically expressed as a Fourier series [13]. Calculating the theoretical cogging torque was not an objective of this design, but the measurement of the cogging torque is still required to determine if it is within an acceptable range. The measured cogging torque is displayed in Figure 7. A small section is displayed for viewing purposes. According to [12] and [13], the measured cogging torque is within an acceptable range. The DC offset is a result of the friction the machine experiences. The oscillation frequency is a function of the stator turns and the number of poles as seen in (21) as follows [13]

$$T_{cogging} = N_p \sum_{k=1}^{\infty} T_{pN_sN_pk} \sin\left(N_s N_p \theta\right) \qquad (21)$$

where N_p is the number of poles, T_{pNsNpk} is the Fourier coefficient of the torque and θ is the angle of rotation.

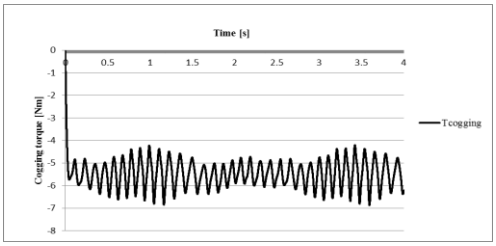

Figure 7: Cogging torque of the prototype

6.4. Final torque results

From [14], the electromechanical torque is derived by

$$T_{em} = \frac{m_s V_{sph}^2 \left(R_r^{'} / s\right)}{\left(\omega_s / p\right)\left(\left(R_s + \left(R_r^{'} / s\right)\right)^2 + \left(\omega\ L_k\right)^2\right)} \qquad (22)$$

where T_{em} is the electromechanical torque, m_s is the amount of phases in the stator, s is the slip, p is the amount of pole pairs, R_s is the stator resistance, $R_r^{'}$ is the rotor resistance referred to the stator and L_k is the machine's short-circuit inductance. The calculated, simulated and measured torque curves are displayed in Figure 8. The torque curve of the induction machine is also displayed. The torque curve of the LSPMSM correlates well with the induction machine and has a higher starting torque. The measured torque curve indicates the presence of the torque ripple as caused by the cogging torque. There is a maximum difference of 7 Nm between the calculated and measured torque curves. The difference between the curves is attributed to the discrepancy between the calculated and measured results of the rotor resistance. If the measured rotor resistance value is used in (22), the calculated torque curve then overlaps the measured torque curve.

Although only 105 mm axial length of the permanent magnet material was installed, this did not have a significant impact on the final torque curve because (22) is a function of the machine's equivalent electric circuit parameters. The stator and rotor resistances are not affected by the permanent magnets and the leakage inductances are dependent on the air gap, slot sizes, end windings and skewing [6]. The permanent magnets are sized to deliver the desired air gap flux density by the

area of the material and flux density. The volume of magnetic material was changed, but the thickness of the magnet in the radial direction did not change and still satisfied (8) and (16).

The efficiency of the prototype was calculated as 92.6% and measured as 91.8%. The equivalent induction machine used for the comparison has an efficiency of 90%. It is evident that the prototype is more efficient than the induction machine.

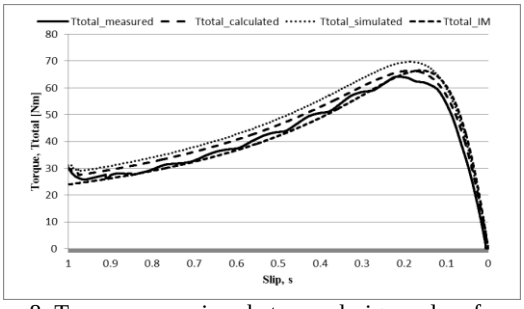

Figure 8: Torque comparison between design and performance test

7. CONCLUSION

Designing a rotor for a LSPMSM requires dividing the design into two sections: the induction machine where the cage or rotor slots are designed and the PMSM where the permanent magnets are designed. The rotors slots were designed by using standard induction machine equations and taking skin effect into consideration. The calculated and measured torque curves indicated that the cage was adequately designed to ensure a starting torque that would overcome the machine's inertia. The permanent magnets were capable of producing the required flux density but that back-emf of the selected material was too high for the prototype and hence less magnetic material was used in the final testing. It is important to perform the back-emf calculations together with the sizing calculations to ensure that the correct material is selected.

The LSPMSM compared well with the induction machine in terms of torque capability. The LSPMSM also proved more efficient that the induction machine, confirming that permanent magnets can improve a machine's efficiency.

8. REFERENCES

[1] J. F. Gieras and M. Wing. "Introduction" in Permanent Magnet Motor Technology, second edition, volume 1. M. Wing, New York: Marcel Dekker Inc., 2002, pp. 12 – 13.

[2] A. H. Isfahani, "Line start permanent magnet synchronous motors: challenges and opportunities", Elsevier: Energy, vol. 34, pp. 1755-1763, April 2009.

[3] J. Pyrhönen, T. Jokinen and V. Hrabovcová. "Design Process and Properties of Rotating Electrical Machines" in Design of Rotating Electrical Machines, first edition, volume 1. West Sussex: John Wiley & Sons, 2008, pp. 307-342.

[4] K. Zhang, X. Jiang, Y. Wu, L. Zhang and X. Wu. "Effect of slot shape in rotor of electrical motor with high-speed spindle on slot ripples" in Proceedings of the 2010 International Conference on Modelling, Identification and Control, Japan, July 2010.

[5] M. Benecke, R. Doebbelin, G. Griepentrog and A. Lindemann. "Skin Effect in Squirrel Cage Rotor Bars and Its Consideration in Simulation of Non-steady-state Operation of Induction Machines" in Proceedings of Progress In Electromagnetics Research Symposium, Marrakesh, Morocco, March 2011.

[6] J. Pyrhönen, T. Jokinen and V. Hrabovcová. "Flux Leakage" in Design of Rotating Electrical Machines, first edition, volume 1. West Sussex: John Wiley & Sons, 2008, pp. 243 – 253.

[7] J. Pyrhönen, T. Jokinen and V. Hrabovcová. "Resistances" in Design of Rotating Electrical Machines, first edition, volume 1. West Sussex: John Wiley & Sons, 2008, pp. 256 – 259.

[8] J. Santiago and H. Bernhoff. "Comparison between Axial and Radial Flux PM Coreless Machines for Flywheel Energy Storage", Journal of Electrical Systems, Issue 2, volume 6, June 2010.

[9] A. E. Fitzgerald, C. Kingsley and S. Umans. "Magnetic circuits and Magnetic Materials" in Electric Machinery, sixth edition, volume 1. New York: McGraw-Hill, 2003, pp. 32 – 34.

[10] D. C. Hanselman. "Design Variations" in Brushless Permanent Magnet Motor Design, first edition, volume 1. United States of America: McGraw-Hill, 1994, pp. 120 – 121.

[11] J. Pyrhönen, T. Jokinen and V. Hrabovcová. "Design Process and Properties of Rotating Electrical Machines" in Design of Rotating Electrical Machines, first edition, volume 1. West Sussex: John Wiley & Sons, 2008, pp. 397-399.

[12] H. Karmaker, "Report on IEEE Standard Working Group P1812 on Guide for Testing Permanent Magnet Machines" in IEEE Transactions on Magnetics, volume 46, pp. 2327 – 2333, 2012.

[13] L. Dosiek, "Cogging Torque Reduction in Permanent Magnet Machines" in IEEE Transactions on Industry Applications, volume 43, pp. 1565 – 1571, 2007.

[14] J. F. Gieras and M. Wing. "Design Process and Properties of Rotating Electrical Machines" in Permanent Magnet Motor Technology, second edition, volume 1. M. Wing, New York: Marcel Dekker Inc., 2002, pp. 330.

Appendix E: Design technical drawings

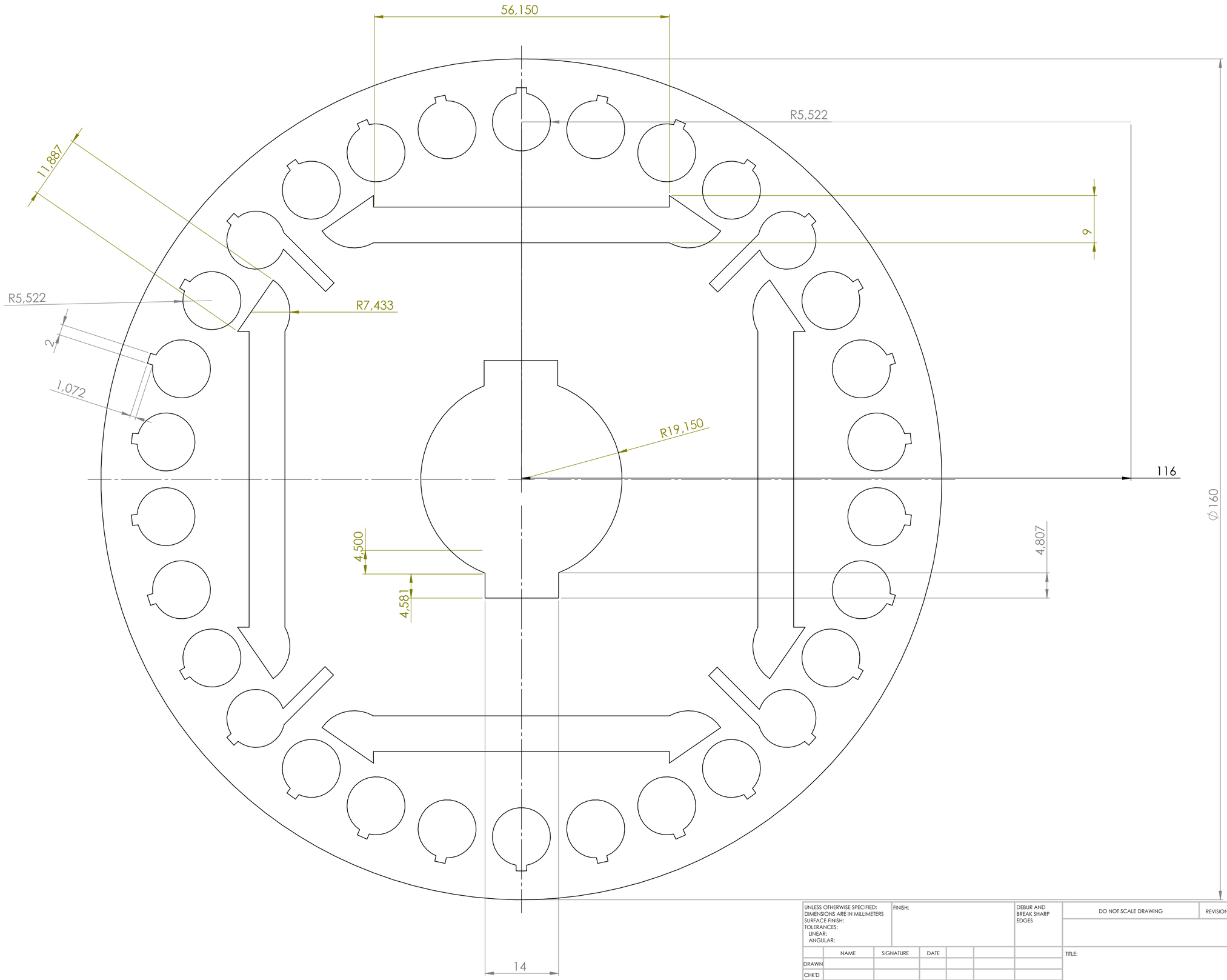

UNLESS OTHERWISE SPECIFIED: DIMENSIONS ARE IN MILLIMETERS SURFACE FINISH: TOLERANCES: LINEAR: ANGULAR:		FINISH:			DEBUR AND BREAK SHARP EDGES	DO NOT SCALE DRAWING	REVISION
	NAME	SIGNATURE	DATE			TITLE:	
DRAWN							
CHK'D							
APPV'D							
MFG							
Q.A				MATERIAL:		DWG NO.	A4
						LSPMSM Rotor to build	
				WEIGHT:		SCALE:1:5	SHEET 1 OF 1

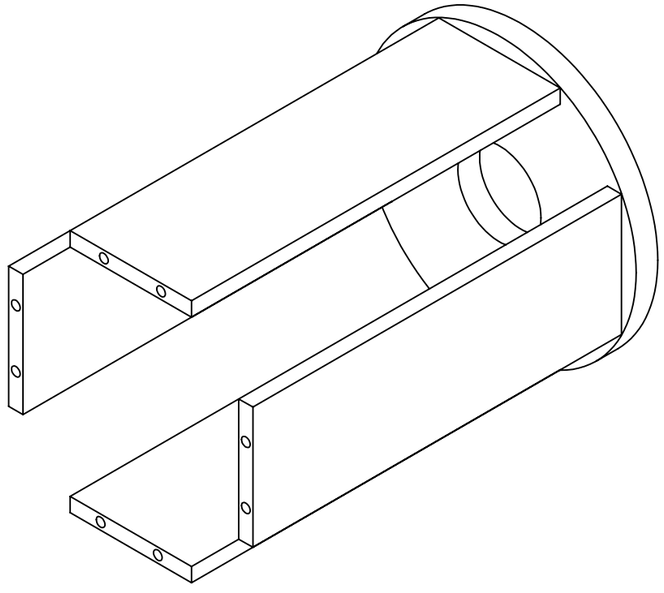

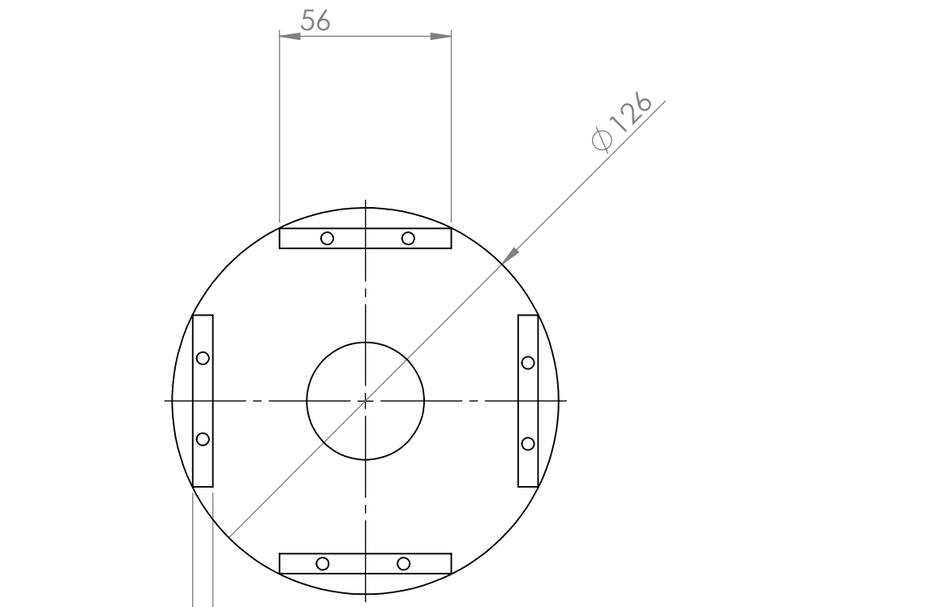

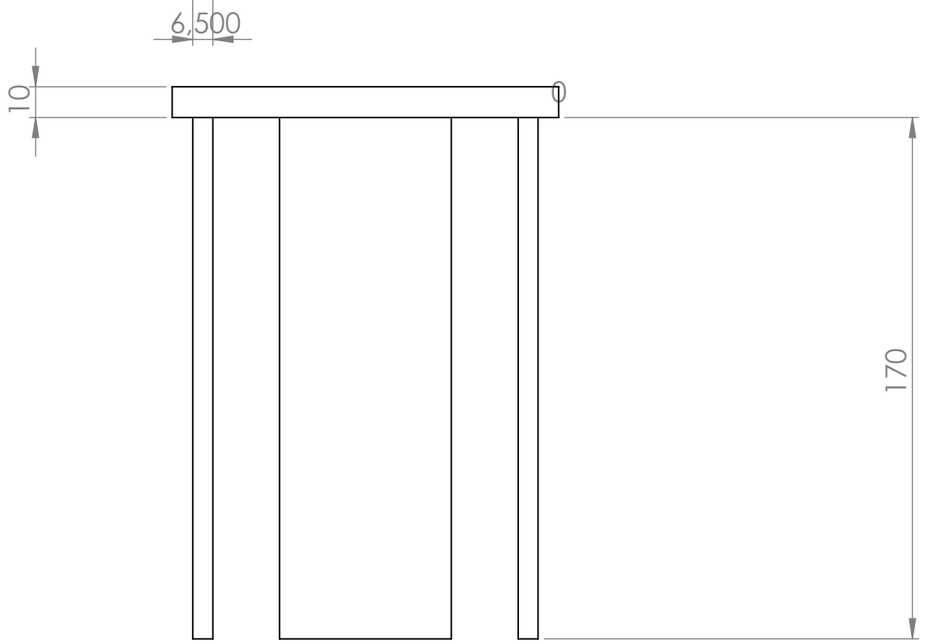

UNLESS OTHERWISE SPECIFIED: DIMENSIONS ARE IN MILLIMETERS SURFACE FINISH: TOLERANCES: LINEAR: ANGULAR:	FINISH:			DEBUR AND BREAK SHARP EDGES	DO NOT SCALE DRAWING	REVISION
	NAME	SIGNATURE	DATE		TITLE:	
DRAWN						
CHK'D						
APPV'D						
MFG						
Q.A				MATERIAL:	DWG NO. Assembly jig	A3
WEIGHT:					SCALE:1:2	SHEET 1 OF 1